In compliance with the
Canadian Privacy Legislation
some supporting forms
may have been removed from
this dissertation.

While these forms may be included
in the document page count,
their removal does not represent
any loss of content from the dissertation.

University of Alberta

Analysis of the Year 2000 Hadronic Endcap Calorimeter Testbeam for the ATLAS Experiment

by

W. Blaine Dowler

A thesis submitted to the Faculty of Graduate Studies and Research in partial fulfillment of the requirements for the degree of **Master of Science**.

in

Subatomic Physics

Department of Physics

Edmonton, Alberta
Fall 2003

National Library of Canada
Acquisitions and Bibliographic Services
395 Wellington Street
Ottawa ON K1A 0N4
Canada

Bibliothèque nationale du Canada
Acquisisitons et services bibliographiques
395, rue Wellington
Ottawa ON K1A 0N4
Canada

Your file Votre référence
ISBN: 0-612-87752-3
Our file Notre référence
ISBN: 0-612-87752-3

The author has granted a non-exclusive licence allowing the National Library of Canada to reproduce, loan, distribute or sell copies of this thesis in microform, paper or electronic formats.

The author retains ownership of the copyright in this thesis. Neither the thesis nor substantial extracts from it may be printed or otherwise reproduced without the author's permission.

L'auteur a accordé une licence non exclusive permettant à la Bibliothèque nationale du Canada de reproduire, prêter, distribuer ou vendre des copies de cette thèse sous la forme de microfiche/film, de reproduction sur papier ou sur format électronique.

L'auteur conserve la propriété du droit d'auteur qui protège cette thèse. Ni la thèse ni des extraits substantiels de celle-ci ne doivent être imprimés ou aturement reproduits sans son autorisation.

Canada

University of Alberta

Library Release Form

Name of Author: W. Blaine Dowler

Title of Thesis: Analysis of the Year 2000 Hadronic Endcap Calorimeter Testbeam for the ATLAS Experiment

Degree: Master of Science

Year this Degree Granted: 2003

Permission is hereby granted to the University of Alberta Library to reproduce single copies of this thesis and to lend or sell such copies for private, scholarly or scientific research purposes only.

The author reserves all other publication and other rights in association with the copyright in the thesis, and except as herein before provided, neither the thesis nor any substantial portion thereof may be printed or otherwise reproduced in any material form whatever without the author's prior written permission.

_____

Iain

Date: May 30, 2003

University of Alberta

Faculty of Graduate Studies and Research

The undersigned certify that they have read, and recommend to the Faculty of Graduate Studies and Research for acceptance, a thesis entitled **Analysis of the Year 2000 Hadronic Endcap Calorimeter Testbeam for the ATLAS Experiment** submitted by W. Blaine Dowler in partial fulfillment of the requirements for the degree of **Master of Science** in *Subatomic Physics*.

Date: Apr 15/03

Abstract

This document details the results of the August 2000 testbeam data for the HEC (Hadronic Endcap Calorimeter) portion of the ATLAS (A Toroidal LHC ApparatuS) experiment based at CERN (European Organization for Nuclear Research). After describing CERN and the ATLAS experiment in general, the HEC is discussed from a design standpoint. Finally, pertinent quantities in this analysis (namely the energy resolution, the electromagnetic and hadronic conversion factors, linearity, and the fraction $\frac{e}{h}$) are defined and measured for this data set. Comparisons are made to results from the June 2000 testbeam period. Some of the results are not always in good agreement (ie. more than two standard deviations). Reasons for the discrepancies are proposed.

Shall I refuse my dinner because I do not fully understand the process of digesting?

Oliver Heaviside (1850-1925)

To my family
for keeping me mostly sane

and to Del Taylor
for being my only high school teacher
who made his subject seem interesting

Acknowledgements

First and foremost, I must thank Dr. Manuella Vincter for her guidance and patience during the course of this thesis program.

I would also like to thank my colleagues at CERN, including Matt Dobbs, Dominique Fortin, Michel Lefebvre, and Carla Sbarra in particular. These four (especially Matt) endured countless irritating questions from someone who had been aiming for research in theory mere months before.

The kind people who visit the comp.text.tex and comp.graphics.apps.gnuplot also deserve thanks for repeatedly assisting with my software troubles.

Finally, I would like to thank the academic and support staff of the University of Alberta, who always found ways to deal with an assortment of bizarre logistical and registration issues that came up during my time here.

Table of Contents

1 Introduction 1
- 1.1 The ATLAS Experiment . . . 1
  - 1.1.1 The HEC . . . 2
- 1.2 What Lies Ahead . . . 2

2 Interactions with Matter 4
- 2.1 Introduction . . . 4
- 2.2 Electromagnetic Interactions and Showers . . . 5
  - 2.2.1 Bremsstrahlung Radiation . . . 5
  - 2.2.2 Pair Production . . . 8
  - 2.2.3 Low Energy Effects . . . 10
  - 2.2.4 Physical Extent of Electromagnetic Showers . . . 12
- 2.3 Hadronic Interactions . . . 14
- 2.4 Sampling Calorimetry . . . 16
- 2.5 Testbeam Predictions . . . 17

3 ATLAS: Physics Potential and Design 19
- 3.1 The Role of ATLAS at the LHC . . . 19
- 3.2 ATLAS Physics Potential . . . 19
- 3.3 The Components of ATLAS . . . 23
  - 3.3.1 Inner Tracker . . . 24
  - 3.3.2 Calorimeter . . . 24
  - 3.3.3 Muon Spectrometer . . . 28
  - 3.3.4 Trigger And Data Acquisition System . . . 28
  - 3.3.5 Computing System . . . 29

4 The HEC and its Design 30
- 4.1 The Location and Purpose of the HEC . . . 30
- 4.2 Design of the HEC . . . 30
  - 4.2.1 The Copper Absorbers . . . 31
  - 4.2.2 Readout: The EST and PAD Boards . . . 31
  - 4.2.3 The DAQ System . . . 34

5 The August 2000 Testbeam Conditions 36
- 5.1 Testbeam Environment and Design Philosophy . . . 36
  - 5.1.1 H6 Beamline . . . 36
  - 5.1.2 The Cryostat . . . 36
  - 5.1.3 Orientation of Modules . . . 37

5.2 The Testbeam Setup 37
5.2.1 Trigger and DAQ Systems 37
5.2.2 Impact Points 40
5.3 The Software 40
5.3.1 The hec_adc Software Package 40
5.3.2 The New Software Package 42

6 The Interesting Quantities: Energy Resolution and Other Measured Quantities 47
6.1 Energy Resolution 47
6.1.1 Clusters and Energy Resolution 48
6.1.2 Intrinsic Energy Resolution 49
6.2 Conversion Factor α 50
6.2.1 Linearity 51
6.3 The Fraction $\frac{e}{h}$ 52

7 The Electron Testbeam Results 53
7.1 The Selection of the Data Subset 53
7.2 Defining Potential Clusters 54
7.3 Optimizing Cluster Sizes Using Point K Data 56
7.4 Measuring the Intrinsic Energy Resolution 59
7.5 Electromagnetic Conversion Factor α 62
7.6 Linearity of Electron Results 63

8 The Pion Testbeam Results 74
8.1 The Expectations 74
8.2 Selection of the Data Subset 75
8.3 Comparison of Pion and Electron Analysis Methods 78
8.3.1 Similarities 79
8.3.2 Differences 79
8.4 Intrinsic Energy Resolution and Determination of Cluster Size . . . 81
8.5 Hadronic Conversion Factor α and the Fraction $\frac{e}{h}$ 90

9 Conclusion 107

A Miscellaneous Derivations 110
A.1 Deriving Equation 2.4 on the following page 110

B My Contributions 111
B.1 The Summer of '99 111
B.2 The Course Work 111
B.3 The Summer of 2000 112
B.4 The Remaining Time 112

Bibliography 113

List of Tables

2.1 The penetration depths x of electrons of various initial energies E_0 in pure copper. 14
2.2 The pentration depth and shower width for pion-instigated hadronic showers at various energies within copper. 16

3.1 The specifications of the LHC, copied directly from the official website. 21

4.1 The granularity of the HEC. 35

7.1 The run numbers corresponding to the data used in the electron analysis at each impact point and beam energy. 60
7.2 The values of the constants in the sampling and linear terms of the intrinsic resolution for electrons. 61
7.3 The values of the electromagnetic conversion factor for each of the six impact points. 62

8.1 The run numbers corresponding to the data used in the pion analysis at each impact point and beam energy. 78
8.2 The fitted parameters of the intrinsic energy resolution for 55 cell clusters with a pion beam. 83
8.3 The fitted parameters of the energy resolution for 55 cell clusters with a pion beam. 90
8.4 A table summarizing the features of the plots in figures 8.14 on page 97 through 8.21 on page 104. 96

List of Figures

2.1 The cross section for various photon interactions in copper. 6
2.2 The relative importance of various electron interactions in lead. . . . 7
2.3 The differential cross section for Bremsstrahlung production for electrons in copper. 9
2.4 The differential cross section for electron pair production by photons in copper. 11

3.1 An artist's conception of the LHC layout. 20
3.2 A schematic view of ATLAS. 25

4.1 A side view of a single wedge of the HEC wheel. 32
4.2 A close-up view of the gap structure between two layers of absorber in the HEC. 33
4.3 A side view of a single wedge of the HEC wheel. 34

5.1 A side view of the HEC, with depiction of the cells in the path of the beam. 38
5.2 A schematic diagram of the triggering system used for the HEC testbeam. 39
5.3 The view of the HEC module from upstream. 41
5.4 A flowchart of the `hec_adc` software package. 43
5.5 A flowchart depicting the structure of the new programs. 45

7.1 A diagram of the face of the 3 front HEC modules used in the testbeam. 55
7.2 The first iteration fit of run 10413. 57
7.3 A sample of a quality Gaussian fit. 58
7.4 An example of a run with a non-Gaussian structure as a result of a trip in the high voltage system. 59
7.5 An example of a run with a non-Gaussian structure, possibly as a result of a calibration error. 64
7.6 The intrinsic energy resolution of electrons at point K with a four cell cluster. 65
7.7 The intrinsic energy resolution of electrons at point K with a five cell cluster. 66
7.8 The intrinsic energy resolution of electrons at point K with a six cell cluster. 67
7.9 A plot of the fitted intrinsic resolution parameter A as a function of cluster size. 68

7.10 A plot of the fitted intrinsic resolution parameter B as a function of cluster size. 69
7.11 The portion of an electromagnetic shower's total energy that would be collected by a given number of cells. 70
7.12 A plot depicting the individual values of the intrinsic resolution parameter A for each impact point using a five cell cluster. 71
7.13 A plot depicting the individual values of the intrinsic resolution parameter B for each impact point using a five cell cluster. 72
7.14 The linearity of the electromagnetic conversion factor α_{em} for electron data at all impact points using five cell clusters. 73

8.1 A pion run with electron contamination. 76
8.2 The intrinsic energy resolution for pions at impact point K. 77
8.3 A sample Gaussian of a quality fit. 80
8.4 A plot of the fitted intrinsic resolution parameter A as a function of the number of cells per cluster. 84
8.5 A plot of the fitted intrinsic resolution parameter B as a function of the number of cells per cluster. 85
8.6 The fraction of the shower energy predicted to be contained in a cluster as a function of the number of cells in the cluster. 86
8.7 The sampling terms for 55 cell clusters at the different impact points. 87
8.8 The linear terms for 55 cell clusters at the different impact points. . 88
8.9 The intrinsic energy resolution for pions at impact point I. 89
8.10 The Monte Carlo simulations of energy leakage for pion showers in the HEC for $y = 0$. 92
8.11 The pion conversion factor for all impact points as a function of energy, uncorrected for energy leakage through the back of the HEC. . 93
8.12 The pion conversion factor for all impact points as a function of energy, corrected for energy leakage through the back of the HEC. . . . 94
8.13 The pion conversion factor for the June 2000 data. 95
8.14 The parameterization of the function in equation 8.2 on page 91 with $f(E) = 0.11 \ln\left(\frac{E}{E_0'}\right)$. 97
8.15 The parameterization of the function in equation 8.2 on page 91 with $f(E) = 0.11 \ln\left(\frac{E}{E_0'}\right)$. 98
8.16 The parameterization of the function in equation 8.2 on page 91 with $f(E) = 0.11 \ln\left(\frac{E}{E_0'}\right)$. 99
8.17 The parameterization of the function in equation 8.2 on page 91 with $f(E) = 0.11 \ln\left(\frac{E}{E_0'}\right)$. 100
8.18 The parameterization of the function in equation 8.2 on page 91 with $f(E) = 1 - \left(\frac{E}{E_0'}\right)^{-0.15}$ 101
8.19 The parameterization of the function in equation 8.2 on page 91 with $f(E) = 1 - \left(\frac{E}{E_0'}\right)^{-0.15}$ 102
8.20 The parameterization of the function in equation 8.2 on page 91 with $f(E) = 1 - \left(\frac{E}{E_0'}\right)^{-0.15}$ 103

8.21 The parameterization of the function in equation 8.2 on page 91 with $f(E) = 1 - \left(\frac{E}{E_0}\right)^{-0.15}$ 104
8.22 The $\frac{e}{\pi}$ parameterization of the function in equation 8.2 on page 91. . 105

List of Symbols

A **(atomic weight, sampling term)** In theoretical calculations, the atomic weight of a nucleus. In experimental analysis, the coefficient of the sampling term in the (intrinsic) energy resolution of a detector, representing the statistical fluctuations that occur during a shower.

α **(fine structure constant)** A dimensionless quantity related to the strength of the electromagnetic interaction. Also, a conversion factor between current measured during a shower and energy of the particle initiating the shower.

α_{em} **(electromagnetic conversion factor)** The factor that relates the initial energy of a lepton which initiates an electromagnetic shower to the current measured in the detector.

α_{had} **(hadronic conversion factor)** The factor that relates the initial energy of a hadron initiating a shower composed entirely of hadronic events to the current measured in the detector.

α_{π} **(pionic conversion factor)** The conversion factor that relates the initial energy of a pion initiating a shower to the current measured during that shower.

B **(constant term)** The term in the energy resolution of a detector, representing leakage effects and calibration errors.

C **(linear term)** The coefficient of the linear term in the energy resolution of a detector, representing the effects of electronics noise. This term is not present in the intrinsic energy resolution of a detector.

χ^2 **(reduced chi squared)** A statistical measure of the confidence the parameter defining a function that has been fitted to data.

e **(electromagnetic response)** The inverse of α_{em}, a measure of a detector's response to electrons.

E **(energy)** In theoretical calculations, the energy of a particle, measured in GeV. In experimental analysis, the mean current resulting from an electromagnetic or hadronic shower, measured in nA.

E' **(energy)** The mean current measured in a detector during a shower, with the linear term subtracted off.

E_0 **(energy, beam energy)** The initial energy of a particle that initiates an electromagnetic shower. Also, the nominal beam energy of a test beam, measured in GeV.

E_0' **(energy parameter)** A parameter used in the relationship between e, h, and π.

E_c **(critical energy)** The critical energy of a particle involved in a shower. If a particle's energy is no larger than this quantity, it will likely be absorbed by the material in its next interaction, and will no longer participate in the shower.

E_i **(initial energy)** The initial energy of an electron before bremsstrahlung radiation emission.

E_f **(final energy)** The final energy of an electron after bremsstrahlung radiation emission.

E_π **(energy)** The mean current measured in a detector during a shower initiated by a pion, measured in nA.

E_+ **(energy)** The energy of a positron produced through the pair production process.

η **(pseudorapidity)** Rather than use the traditional spherical angles of θ and ϕ, experimental physicists often reparametrize θ as the pseudorapidity $\eta = -\ln\left(\tan\left(\frac{\theta}{2}\right)\right)$.

$f(E)$ **(parametrization)** A function used to relate the detector's response to electrons, pions, and hadrons.

k **(energy)** The energy of a photon emitted by an electron during bremsstrahlung radiation. Also, the energy of a photon before experiencing pair production.

h **(hadronic response)** The inverse of α_{had}, the response of the detector to hadronic events.

$L(E)$ **(shower length)** The depth of a hadronic shower. Analogous to $R(E)$.

λ **(absorption length)** The mean absorption length (also called nuclear interaction length) of a material.

N_A **(Avogadro's number)** Avogadro's number, the number of particles in one mole of a substance, which is roughly 6×10^{23}.

π **(pionic response)** In theoretical calculations, the ratio of a circle's circumference to its diameter. In experimental analysis, the inverse of α_π, which is a measure of a detector's response to pions.

q_e **(elementary charge)** The elementary charge, 1.602×10^{-19} C.

$R(E)$ **(range)** The range of an electron in a material. Analogous to $L(E)$.

r_e **(electron radius)** The classical electron radius, defined as

$$r_e = \frac{q_e^2}{4\pi\epsilon_0 m_e c^2} \approx 2.82 \times 10^{-15}\,\text{m}$$

where q_e is the elementary charge, ϵ_0 is the permittivity of free space, m_e is the mass of an electron, and c is the speed of light in vacuum.

ρ **(density)** The mass density of a material, measured in g/cm^3.

ρ_M **(Molière radius)** The Molière radius of an electromagnetic shower. Analogous to $W(E)$.

σ **(cross section, Gaussian width)** In theoretical calculations, the cross section, which is a measure of the likelihood of a given interaction (or set of interactions). In experimental analysis, the width of a Gaussian that has been fitted to data for a run.

σ_{abs} **(absorption cross section)** The absorption cross section for hadrons showering in a material.

$W(E)$ **(shower width)** The width of a hadronic shower. Analogous to ρ_M.

x **(penetration depth)** The penetration depth of an electromagnetic shower.

X_{rad} **(radiation length)** The radiation length of electromagnetic showers. It depends only upon the physical properties of the material the shower is occurring in.

Z **(atomic number)** The atomic number of an atom, which is the number of protons in the nucleus.

Chapter 1

Introduction

This thesis documents the analysis of the data collected at the Hadronic Endcap Calorimeter (HEC) testbeam in August of the year 2000. In order to document this properly, some concepts and terms must first be discussed in detail; this will be the purpose of chapters two through six of this thesis. This chapter will outline the purpose of the ATLAS (*A Toroidal LHC ApparatuS*) experiment, as well as provide an outline of the rest of this thesis.

1.1 The ATLAS Experiment

The ATLAS experiment is one of several high energy physics experiments that will be able to probe into the interactions of particles in the TeV energy regime. Physics interactions at these energies can allow us to examine the properties of quantum chromodynamics (QCD), electroweak gauge bosons, heavy quarks (the b and t quarks in particular) and leptons, the elusive Higgs boson, supersymmetry, and other physics beyond the standard model.

When completed in 2007, ATLAS will be a very large and complex piece of equipment, comprised of several dedicated components. Each component will be responsible for recording data from different aspects of interactions, so that the combined unit will be able to record a variety of physics processes in a way that no single component detector could be able to do.

It would be costly and inefficient to repair various components of ATLAS during its operation[1], so testbeams are performed periodically on some of the components

[1]Due to the logistical needs of the LHC (*Large Hadronic Collider*), access to a detector will only be possible for one month each year, which means components which do not function properly may need to wait for several months before they are repaired. Some components will not be accessible for the entire lifetime of the experiment, so they must be guaranteed to function properly from the outset.

as they are completed. This allows us to confirm that the components of the ATLAS detector are performing as expected before the detector is completely assembled and brought online. The testbeams themselves are designed to recreate actual ATLAS conditions, so that we can also ensure that the components perform according to the design specifications. An understanding of the unit's performance in a testbeam situation will be a valuable indicator of its performance when the physics processes mentioned above are being explored.

1.1.1 The HEC

The HEC is the component of ATLAS responsible for determining the energy of hadronic particles produced from the proton-proton collisions at the LHC (*L*arge *H*adronic *C*ollider). The mass of the HEC is predominantly copper. Sandwiched between the copper layers are readout boards in liquid argon, which collect the signal deposited by hadronic showers produced in the copper. This thesis examines the performance of some of the HEC modules in the controlled environment of a testbeam.

Hadronic calorimetry is a necessary function of ATLAS due to the large quantities of hadronic particles produced in the proton-proton collisions that will be occurring at the LHC. The hadronic calorimeter must be precise enough to measure hadrons as well as the hadronic jets that will be produced by the hadronization processes that result from interactions. These jets can be produced in virtually any direction (although some directions are more likely than others), which means an effective hadronic calorimeter would require high hermeticity, enclosing most of the solid angle visible from the interaction point.[2] The hadronic endcaps serve to enclose the ends of the cylindrical hadronic calorimeter, without impeding the incident beams.

1.2 What Lies Ahead

The second chapter of this thesis will detail the theoretical concepts that describe the possible interactions of particles with matter. It will also describe the specific methods implemented to measure these interactions with this particular detector design, and make predictions about the results we expect to obtain from this sort

[2] If it enclosed the entire solid angle, then there would be no way for the beam particles to enter the detector unimpeded before the collision.

of design.

The third chapter of this thesis will detail the complete ATLAS detector, describing its design and components, as well as the long-range research goals that the detector is intended to achieve.

The fourth chapter will describe the HEC itself in much greater detail, as it is a piece of this particular component of ATLAS that is being studied in this thesis.

The fifth chapter will describe the testbeam environment, and how it is related to the environment in the final production version of ATLAS.

The sixth chapter will detail the specific quantities of interest to research physicists who are using this detector. It will define the various measurable quantities, such as energy resolutions, conversion factors, and linearity, and describe how those measurements are used to describe a detector's performance.

Chapters seven and eight will detail the analysis of the electron and pion data collected in the August 2000 testbeam, related in terms of the quantities defined in chapter six, and will compare these results to theory (found in chapter two) as well as to those obtained by an independent study of data taken the same year [1]. Assessments of detector performance will be made here.

The ninth chapter of the thesis will summarize the results of the analyses performed and the assessments of the detector performance.

The first appendix will detail some calculations that were performed to obtain expressions found in the theory chapter. The second appendix will detail the complete range of activities and experiences performed by the author during the period of his M.Sc. program, including the activities that are not immediately apparent when reading the rest of this document.

Chapter 2

Interactions with Matter

The variety and nature of the interactions that will be taking place within the HEC when ATLAS is in full operation are detailed in this chapter. The chapter begins with a brief introduction of some of the general properties of particle interactions and showers. It then moves on to specific interactions, such as bremsstrahlung and pair production, that are experienced by different particle types, and discusses their overall importance. These are the processes that cause a single incident particle to spawn hundreds of other particles within the detector. The overall characteristics of these resulting particles are then studied, and used to determine the type and energy of the parent particle that first entered the detector. The final portion of this chapter deals with some of the limitations and design philosophies of particle detectors used in identifying particles with energies on the order of a few dozen GeV, and the potential impacts these philosophies will have on sampling calorimeters such as the HEC. This portion will also include predictions of testbeam performance.

2.1 Introduction

One of the most useful tools available to researchers working on ATLAS is a phenomenon known as showering. Showering occurs when a particle with high kinetic energy interacts with matter, such as a dense detector, depositing energy and producing other particles. The incident particle's type and energy determine which interactions are possible, as well as their relative probability of occurance.

The particles produced as a result of the shower may be emitted in any direction in the center of momentum inertial reference frame. However, in the lab's inertial reference frame, the Lorentz boost from the original particle tends to confine the resultant particles to a cone-shaped structure. By examining the composition, shape,

and energy of this shower, we are able to reconstruct the energy and particle type of the particle that instigated the shower.[1]

As the particles from the initial shower interact with the detector, they may also undergo similar interactions, spawning smaller showers which serve to expand and compound the initial shower. Thus, any single shower is a combination of various processes and interactions. The data used in this thesis corresponds to showers that were produced primarily through electromagnetic and hadronic interactions.

It should be noted that the primary reference for this chapter was reference [2].

2.2 Electromagnetic Interactions and Showers

Particles whose behaviours are dominated by electromagnetic interactions, such as electrons and positrons, experience interactions as a direct result of their electric charge. Photons participate in electromagnetic interactions by coupling with particles that have an electric charge. These electromagnetic interactions can occur with any particle with an electrical charge (such as the π^+, for example) but they will be discussed below in terms of electrons (and positrons) for reasons that will be made clear in section 2.3 on page 14. Figure 2.1 on the next page depicts the relative importance of various interactions occuring when photons pass through copper. Figure 2.2 on page 7 shows the relative importance of processes that might occur when electrons pass through lead. The individual processes involved will be explained in more detail in the rest of this chapter.

2.2.1 Bremsstrahlung Radiation

One of the dominant interactions leading to the energy loss of electrons is known as Bremsstrahlung. Bremsstrahlung radiation is an interaction between an incoming electron and the Coulomb field of an atom in matter which results in the emission of a photon whose energy is a significant portion of the parent electron's initial energy.

An electron (with initial energy E_i) encounters matter and interacts with the Coulomb field of an atomic electron. The incoming electron emits a photon with energy k and recoils with energy E_f such that $E_f = E_i - k$. The differential cross section for this interaction is given by (equation 2.49 in [2])

$$\frac{d\sigma}{dk} = \frac{4\alpha Z^2 r_e^2}{k}\left[\left(1+\left(\frac{E_i-k}{E_i}\right)^2 - \frac{2}{3}\frac{(E_i-k)}{E_i}\right)\ln\left(\frac{183}{Z^{\frac{1}{3}}}\right) + \frac{E_i-k}{9E_i}\right] \qquad (2.1)$$

[1]The instigating particle is often referred to as the parent particle.

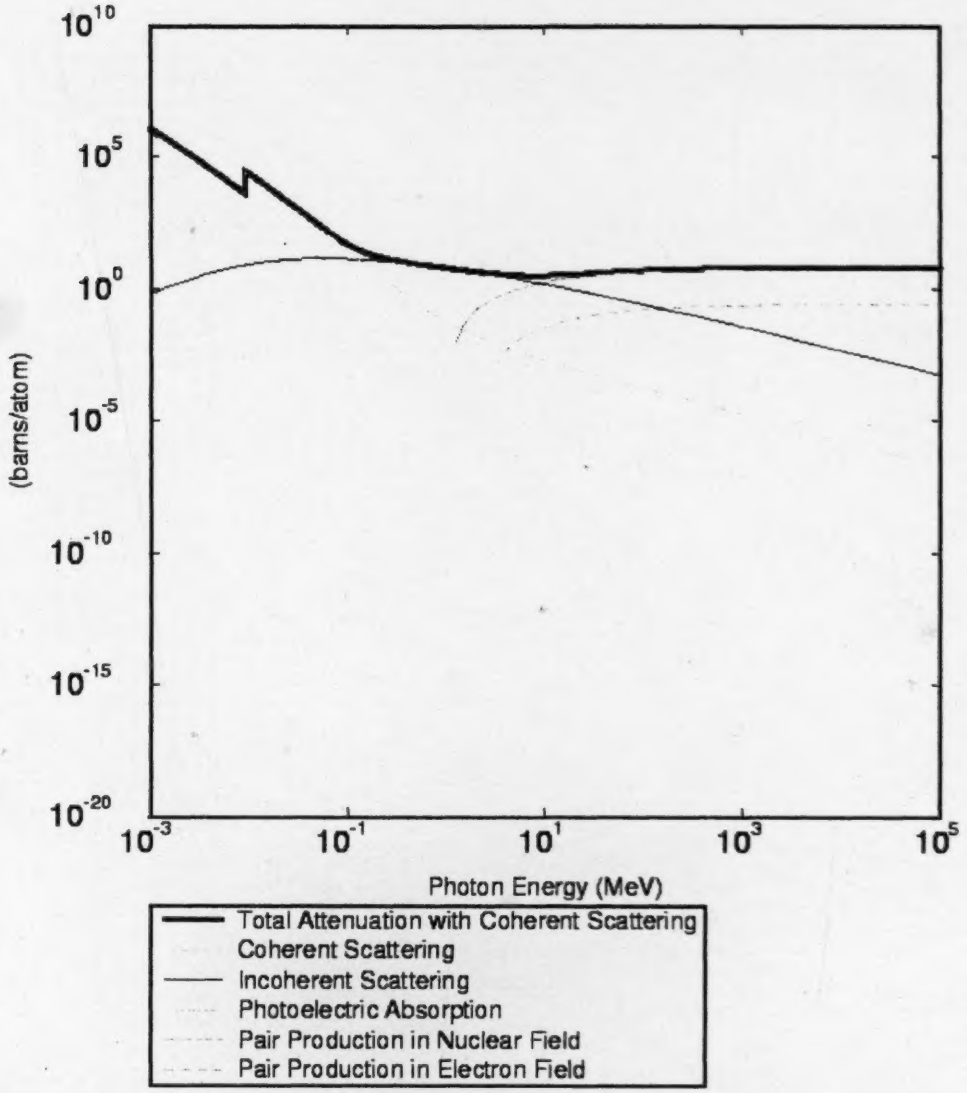

Figure 2.1: The cross section for various photon interactions in copper. Pair production is the dominant process for photons with energies above $\approx$ 10 MeV. This plot was generated at `http://physics.nist.gov/PhysRefData/Xcom/html/xcom1.html`. One barn is $10^{-24}\,\mathrm{cm}^2$.

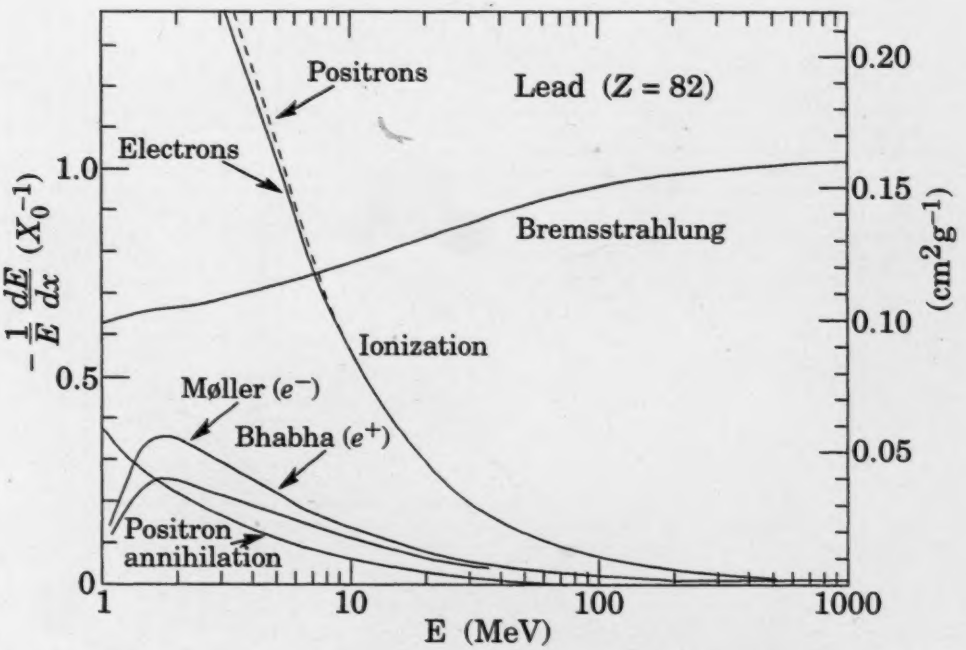

Figure 2.2: The relative importance of various electron interactions in lead. Bremsstrahlung radiation is the dominant process at the energies used in the test-beam studies. (Moller scattering is more significant than Bhabha scattering.) This figure originally appeared in reference [3].

where α is the fine structure constant, Z is the atomic number of the detector material ($Z = 29$ for copper), and r_e is the classical electron radius. While this would appear to depend on the specific energies of the particles involved, careful inspection will reveal that $d\sigma$ depends only on the fractional energy transferred from the initial electron to the photon, and some physical constants determined by the nature of the materials themselves. For this reason, the graph of the differential cross section in figure 2.3 on the next page for copper has been scaled, so that $\frac{d\sigma}{dk}E_i$ is plotted on the y-axis. (This variable is independent of E_i.) The complete integrated cross section is given by

$$\sigma = 4\alpha Z^2 r_e^2 \left(\ln\left(\frac{183}{Z^{\frac{1}{3}}}\right) + \frac{1}{18} \right) \tag{2.2}$$

which, for copper, gives $\sigma = 8\,\mathrm{b}$. (See equation 2.52 in reference [2].)

This is the dominant process of energy loss for particles interacting electromagnetically with energies in the range of $6\,\mathrm{GeV} - 200\,\mathrm{GeV}$, such as those used in the HEC testbeam. (See figure 2.2 on the preceding page. Note that this figure is for electrons in lead; the comparable plot for copper is the same at the qualitative level, but differs at the quantitative level.)

During bremsstrahlung, the particles lose energy in the form of photons. Both the resultant photons and energy-reduced parent particles are free to interact again.

2.2.2 Pair Production

Most of the photons produced in bremsstrahlung radiation of electrons from the HEC beam test particles have sufficient energy to participate in pair production. Pair production is an interaction allowing a photon to interact with a nearby atom's electron or nuclear Coulomb field which destroys the parent photon, distributing its energy over a pair of daughter particles, which are usually[2] electron-positron pairs.

The differential cross section for the production of a positron of energy E_+ from pair production by a photon of energy k is given by (equation 2.67 in [2]):

$$\frac{d\sigma}{dE_+} = \frac{4\alpha Z^2 r_e^2}{k^3}\left[\left(\frac{4}{3}E_+^2 - \frac{4}{3}kE_+ + k^2\right)\ln\left(\frac{183}{Z^{\frac{1}{3}}}\right) - \frac{1}{9}E_+\left(k - E_+\right)\right] \tag{2.3}$$

where E_+ is the energy of the daughter positron. For a photon traveling through copper, the differential cross section of pair production is at a minimum when E_+

[2]It is also possible to produce muon-antimuon pairs, which do not participate heavily in interactions involving the HEC.

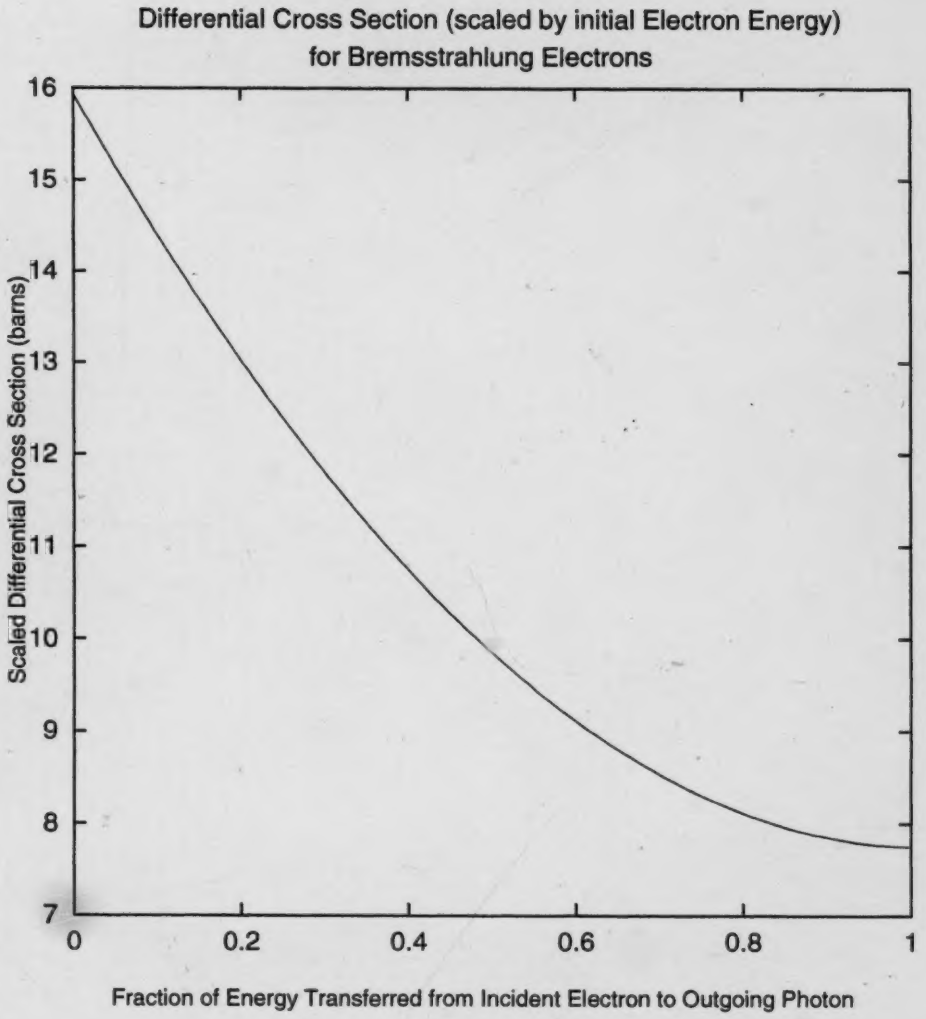

Figure 2.3: The differential cross section for Bremsstrahlung production for electrons in copper. The vertical axis is the variable $\frac{d\sigma}{dk}E_i$ which is independent of the specific E_i. The units of the vertical axis are barns, while the horizontal axis, indicating the fraction of the initial electron's energy transferred to the photon, is dimensionless.

is 50% of the photon energy k, as can be clearly seen in figure 2.4 on the next page. The total cross section of pair production from a photon is given by (see section A.1 for details)

$$\sigma = 4\alpha Z^2 r_e^2 \left(\frac{7}{9} \ln \left(\frac{183}{Z^{\frac{1}{3}}} \right) - \frac{1}{54} \right) \tag{2.4}$$

which, for photons traveling through copper ($Z = 29$), is approximately 6 b (See figure 2.1 on page 6, which shows that pair production is the dominant interaction for photons at testbeam energies.) (This assumes that the photon energy $k \gg 2m_e c^2$, where m_e is the mass of an electron, as this is the threshold energy for this process when the photon interacts with a free electron. The threshold is $k \gg 4m_e c^2$ for an atomic electron. Since most of the photons interacting in the HEC have energies at least an order of magnitude above this threshold, the approximation is valid.)

2.2.3 Low Energy Effects

The effects described above are the dominant methods of energy loss for electrons, positrons and photons in the 6 GeV – 180 GeV energy range used for the HEC testbeam. The processes described below are the less likely sources of energy loss, and are only significant once the particles in the showers have a reduced energy of a few MeV.

Ionization

As electrons travel through the medium of the detector, they can ionize the atoms within, transferring their energy to the electrons which escape atomic confinement.

The cross section for this process can be seen in figure 2.2 on page 7. The energy lost through this process is insignificant for copper at testbeam energies when compared to other processes.

Positron Annihilation

Positrons that are present either as the result of pair production or as beam particles may experience annihilation when they encounter electrons in the detector, commonly producing two photons[3].

The cross section, as seen in figure 2.2 on page 7, is a decreasing function in $\gamma = \frac{E_+}{m_e c^2}$ (where E_+ is the energy of the positron,) and as such is not significant

[3]It is possible for annihilation to produce three, or more photons, but these processes are far less likely than two photon decay. It's also possible that only a single photon will escape to be detected when an electron interacts with an atom, but this is also unlikely.

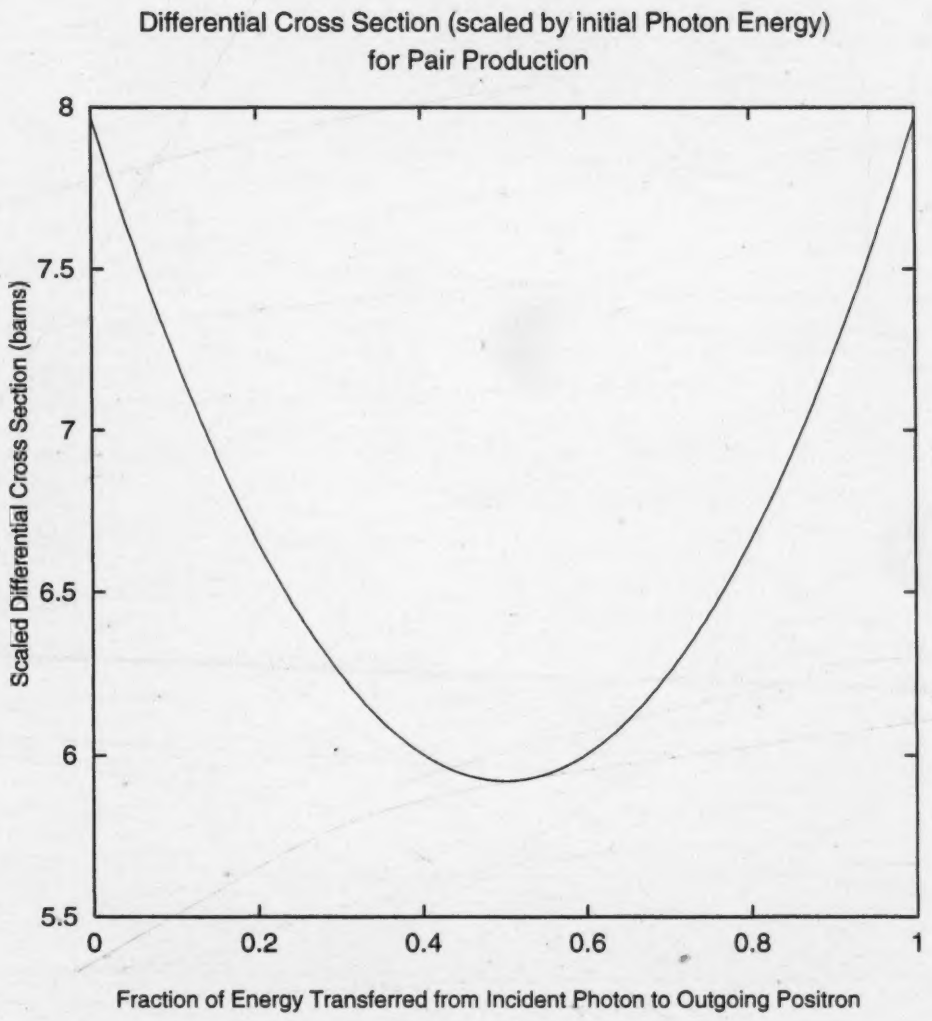

Figure 2.4: The differential cross section for electron pair production by photons in copper. The vertical axis is the variable $\frac{d\sigma}{dE_+}k$ which is independent of the specific k. The units of the vertical axis are barns, while the horizontal axis, indicating the fraction of the initial photon's energy transferred to the positron, is dimensionless.

for particles of energies as high as those used in the initial particle beam. It is approximately 19 mb for 6 GeV positrons, and 0.24 b for 1 MeV positrons, for which $\gamma \approx 2$.

Compton Scattering

Photons may scatter off electrons, be they atomic electrons or free electrons produced in the shower. This interaction is known as Compton Scattering.

This cross section, as seen in figure 2.1 on page 6 (where this process is labelled "incoherent scattering,") is approximately 6.5 mb for a 6 GeV photon, but it rises to 6.1 b when the photon energy is 1 MeV. As such, Compton scattering is not significant until the latest stages of the shower.

Photoelectric Effect

The photoelectric effect also contributes to the energy loss of a shower. When a photon of sufficient energy interacts with an atomic electron, that electron may escape its atom and join the shower. The cross section is not continuous (as the energies of the different electron orbits are quantized) but it is very low, and not significant for high energy interactions.

Atomic Excitation

A sufficiently low energy particle can collide with an atom, transferring so little energy that the atom is excited, but not ionized. The energy losses due to atomic excitation and ionization have been described in a single equation, known as the Bethe-Bloch equation. The cross sections for these processes can be seen in figure 2.2 on page 7.

2.2.4 Physical Extent of Electromagnetic Showers

Particles produced in electromagnetic interactions can themselves interact with matter, resulting in a shower of particles. These electromagnetic showers progress both transversely and longitudinally to the direction of the parent particle. These shower properties may be characterized by the Molière radius ρ_M and by the radiation length X_{rad} respectively.

One of the key elements to the measurement of the energy deposited by a shower is the accurate prediction of its size. As you increase the amount of electronics

involved in collecting a signal, you increase the amount of random noise to sift through. On the other hand, if you only examine a portion of the detector that is too small to contain the entire shower, you risk losing accuracy in the results because much of the shower's energy is not being collected.

Radiation Length

The longitudinal profile of an electromagnetic shower can be predicted using statistical approximations. All the processes discussed above contribute to the total energy loss of the particle.

The rate of energy loss of an electron by radiation with respect to depth in a detector is dominated by the Bremsstrahlung process for energies above $\approx 10\,\text{MeV}$ (as seen in figure 2.2 on page 7), and is given by

$$\frac{dE}{dx} = -\frac{E}{X_{rad}} \tag{2.5}$$

where x is the depth the electron has penetrated. A commonly used quantity for measuring penetration depth is the radiation length X_{rad}. This is the distance over which a particle of energy E is likely to be reduced to an energy of $\frac{E}{e}$. This radiation length for electromagnetic showers is given by (see [2])

$$X_{rad} \approx \frac{180A}{Z^2}\text{g/cm}^2 \tag{2.6}$$

where X_{rad} is the radiation length, A is the atomic weight of the detector atoms in atomic mass units, and Z is the familiar atomic number. For pure copper, this is approximately $12.86\,\text{g/cm}^2$, corresponding to a physical distance of $1.43\,\text{cm}$ (see [3]).[4] The particle energy on average will continue to drop by approximately $\frac{1}{e}$ for each radiation length the particle traverses until it reaches a critical energy $E_c \approx \frac{800\,\text{MeV}}{Z+1.2} \approx 26\,\text{MeV}$ (for copper), at which time the particle loses all its energy through collisions and the shower progression stops.

The energy E of an electron which has traversed x distance in some absorber is described by

$$E(x) = E_0 e^{-\frac{x \cdot \rho}{X_{rad}}} \tag{2.7}$$

where $X_{rad} \approx 12.86\,\text{g/cm}^2$ for copper, ρ is the density of the material, and E_0 is the initial energy. Thus, an electron will be reduced to an energy $E(x) = E_c$ when it

[4] It should be noted that the range of a particle is often expressed in units of g/cm^2. A physical distance is the quotient of this range and the density of the material.

E_0 (GeV)	x (cm)
6	7.75
10	8.49
20	9.48
30	10.06
40	10.47
50	10.79
60	11.05
80	11.46
100	11.78
120	12.04
150	12.36

Table 2.1: The penetration depths x of electrons of various initial energies E_0 in pure copper.

has penetrated a distance

$$x = -X_{rad} \ln\left(\frac{E_c}{E_0}\right) \tag{2.8}$$

into the material. Penetration depths for various energy electrons in copper can be found in table 2.1.

The range R of an electron is given by

$$R(E) = \int_0^E \frac{1}{\left(\frac{dE}{dx}\right)} dE \tag{2.9}$$

Molière Radius

The transverse progression of electromagnetic showers is given by the Molière radius ρ_M. Statistically speaking, integrated over depth, 10% of the energy of a shower is deposited outside a circle of radius ρ_M. For showers produced through electromagnetic interactions, this radius is given approximately by (see [2])

$$\rho_M \approx X_{rad} \frac{(21\,\text{MeV})}{E_c} \tag{2.10}$$

where ρ_M is the Moliere radius. For copper, this number is approximately $10.3\,\text{g/cm}^2$, corresponding to a physical distance of 1.15 cm. For 99% containment, we require containment as far as $3.5\rho_M$ from the center of the shower.

2.3 Hadronic Interactions

Particles whose behaviour in a detector is dominated by the strong interaction, such as pions and other hadrons, exhibit different behaviours than particles whose

interactions are dominated by the electromagnetic interactions.

When hadrons enter matter, they can interact with the nuclei within. Some of these interactions are elastic (scattering), some are inelastic (absorption), and others still are quasi-elastic. In these interactions, the incident particle scatters off of nuclei, converting some of its energy into new daughter particles (such as mesons or baryons) that carry momentum away from the interaction. These new daughter hadrons can continue to interact with other nuclei, creating new daughter particles, propagating a shower. This shower is actually a combination of showers; some particles involved, such as the $\pi^{\pm}$, produce hadronic showers, while other particles involved, such as the π^0 produced electromagnetic showers. This combination of shower types is important for the determination of the ratio $\frac{e}{h}$, which will be discussed in greater detail in section 6.3.

According to reference [2], the interaction cross section for hadrons in copper is approximately 1.232 b. The mean absorption length λ (also called nuclear interaction length) for hadrons in an absorber material is defined as (see reference [2])

$$\lambda = \frac{A}{\sigma_{abs} \cdot N_A} \tag{2.11}$$

where A is the atomic weight of the absorber material, N_A is Avagadro's number, and σ_{abs} is that material's absorption cross-section. For pure copper, the absorption length is approximately $\lambda = 135\,\mathrm{g/cm^2}$, corresponding to a physical distance of 15 cm.

Because hadronic showers take longer to develop, they tend to be wider and deeper than electromagnetic showers. The depth over which a hadronic shower will deposit 90% of its energy has been parameterized as (see reference [2])

$$L(E) = -1.26 + 1.74 \ln(E) \tag{2.12}$$

where E is the parent hadron's energy in GeV and L is the depth of the shower, expressed as a multiple of the interaction length. Because the energy loss by the shower over the depth of the detector is exponential in nature, the depth required to deposit 95% of the energy is $2L$.

The width of a pion shower can also be described in such a parameterization. While the electron showers tend to spread out only slightly, pion showers tend to spread out rapidly in the early stages. Both shower types then close back in again toward the end. The width containing 99% of the energy of these showers can be

E (GeV)	L (cm)	W (cm)
10	41.5	15.6
20	59.7	25.5
30	70.4	31.3
40	78.0	35.5
50	83.8	38.6
60	88.6	41.2
80	96.2	45.4
100	102.1	48.6
120	106.9	51.2
150	112.7	54.4
180	117.5	57.0
200	120.3	58.5

Table 2.2: The pentration depth and shower width for pion-instigated hadronic showers at various energies within copper.

parameterized as (see reference [2])

$$W(E) = -17.3 + 14.3 \ln(E) \tag{2.13}$$

where W is the width of the shower in centimeters, and E is the energy of the parent hadron in GeV. Values of W and L for the testbeam pions can be found in table 2.2

2.4 Sampling Calorimetry

In systems with center of momentum frame energies as high as those used in ATLAS, the particles to be detected can have remarkably high energies. In these cases, a very efficient use of the limited space available is to build a sampling calorimeter.

A sampling calorimeter is a type of detector that is not designed to collect all the energy deposited by a shower. Instead, the detector has alternating layers of high density material, such as copper, and layers that take an active role in energy collection, such as liquid argon.

When the particles in the shower pass through an active material, they either collide with the atoms, depositing energy and leaving them in an excited state, or they ionize the atoms. In the case of an excited atom, the atomic electrons then drop to a lower energy state, emitting a photon in the process. These photons are then collected by the detector, or alternatively, they ionize other atoms, and the newly freed electrons are collected instead.

In a sampling calorimeter, the energy measured directly is only a fraction of the energy deposited in the detector by the shower. Much of the energy is deposited in the dense absorption layers, where readout electronics are not present and deposited energy cannot be easily measured. However, the radiation length of a shower in material such as copper is much smaller than it is in material such as argon, which means that the detector can be much more compact than it would be if it were entirely made of the active layer material.

Unfortunately, the design improvements that result from a compact detector come at a cost. The energy deposited in the dense absorption layers is not measured directly, and therefore must be estimated. This estimation comes with its own statistical uncertainties. Furthermore, the use of a sampling calorimeter gives rise to a non-uniformity in the detector, as the material that the particles pass through changes as a function of depth.

2.5 Testbeam Predictions

Now that we have covered the theory behind the interactions involved, we can make some predictions specific to the data examined in this thesis. Some of this discussion requires knowledge of the physical properties of the hadronic endcap detector that is being studied in this thesis. Therefore, a cursory discussion of these properties can be found in the next paragraph, but more detail is given in chapter 4.

The detector is composed of copper absorbing layers sandwiching layers of readout electronics. A set of readout electronics that is treated by the data acquisition software as a single unit is called a cell. Since normally no single cell is large enough to contain a shower initiated by the testbeam particles, the studies are done by examining the combined results of several cells. These groups of cells are called clusters.

The first predictions to make are for the physical extent of the showers, which will dictate the number of cells in a cluster, as well as describe the amount of the shower that will escape the detector. When a portion of a shower is not contained in a detector, it is said that leakage occurs.

The physical extent of the electron showers is straightforward to calculate. Knowing that the depth of a shower is given by equation 2.8 on page 14, and that the radius of a shower is given by equation 2.10 on page 14, one can quickly calculate that an electron with an initial energy of 150 GeV will likely only shower

to a depth of approximately 12 cm with a radius of only 4 cm to be 99% contained. (See table 2.1 on page 14.) Depending on the impact point of the incident particle, this can span 1 to 4 cells. Leakage is expected to be insignificant for electrons.

To estimate the number of cells that will be required to enclose a pion shower, we must describe the maximum size of such a shower within the detector. We begin by using twice the result of equation 2.12 on page 15 to describe the depth of the detector required for the shower to deposit 95% of its original energy. For our highest energy particle (200 GeV), this is a depth of 240 cm, which is approximately 90 cm longer than the entire HEC. Therefore, based on this simple estimation it is unreasonable to assume that we will be able to contain 95% of the largest pion showers. However, since one only requires 120 cm of copper to absorb 90% of the shower, the 144 cm of copper in the detector should be sufficient to contain more than enough of the shower to provide meaningful experimental data. There will be several percent leakage of energy out of the back of the detector.

The width of the hadronic shower is the other major concern. At its greatest extent, equation 2.13 on page 16 tells us that the minimum width of a detector which can contain 99% of the shower from a pion with energy of 200 GeV is approximately 58 cm. A width this large will exceed the confines of the detector for pions incident at most impact points, so lateral leakage out of the module is to be expected under testbeam conditions. (This is why several adjacent modules are used to contain the shower.) It would likely require no more than 60 cells to contain most of the shower, but this number strongly depends on the incident energy.

Since each beam impact point on the detector will have slightly different geometry than the others, a slightly different cluster size may be optimal for each impact point. (This is true for both electromagnetic showers and hadronic showers.) Therefore, these predictions for the size of the required clusters should only be treated as estimates. Studies of a wide variety of cluster sizes will be used to make an optimal recommendation. These results will be compared (in chapter 8) to the detailed Monte Carlo simulations of the detector behaviour (described in reference [1]) to ensure consistency with predicted results.

Chapter 3

ATLAS: Physics Potential and Design

The design of ATLAS, both on its own and in relation to the LHC, will be described in this chapter. The ATLAS physics potential is described, and the importance of some of these discoveries is highlighted.

Following this general discussion, there will be a cursory description of the various components of ATLAS, working through them sequentially from the interaction point in the center of the detector to the outer reaches. The description of the Hadronic Endcap Calorimeter given below will be expanded upon in the next chapter.

3.1 The Role of ATLAS at the LHC

ATLAS is one of four detectors that are planned to be in operation on the LHC when it begins operation in 2007. The LHC layout can be seen in figure 3.1 on the next page.

The technical specifications of the LHC can be found in table 3.1 on page 21. There will be two beampipes used in the ring, both able to provide protons of up to 7 TeV for experiments. The beamlines (which run in opposite directions) will cross in four locations, each of which will be the home of a detector situated to take advantage of the 14 TeV worth of energy in the center of momentum frame.

3.2 ATLAS Physics Potential

There are several goals for ATLAS in terms of exploration and validation of particle physics theory, many of which involve the study of physics beyond the Standard

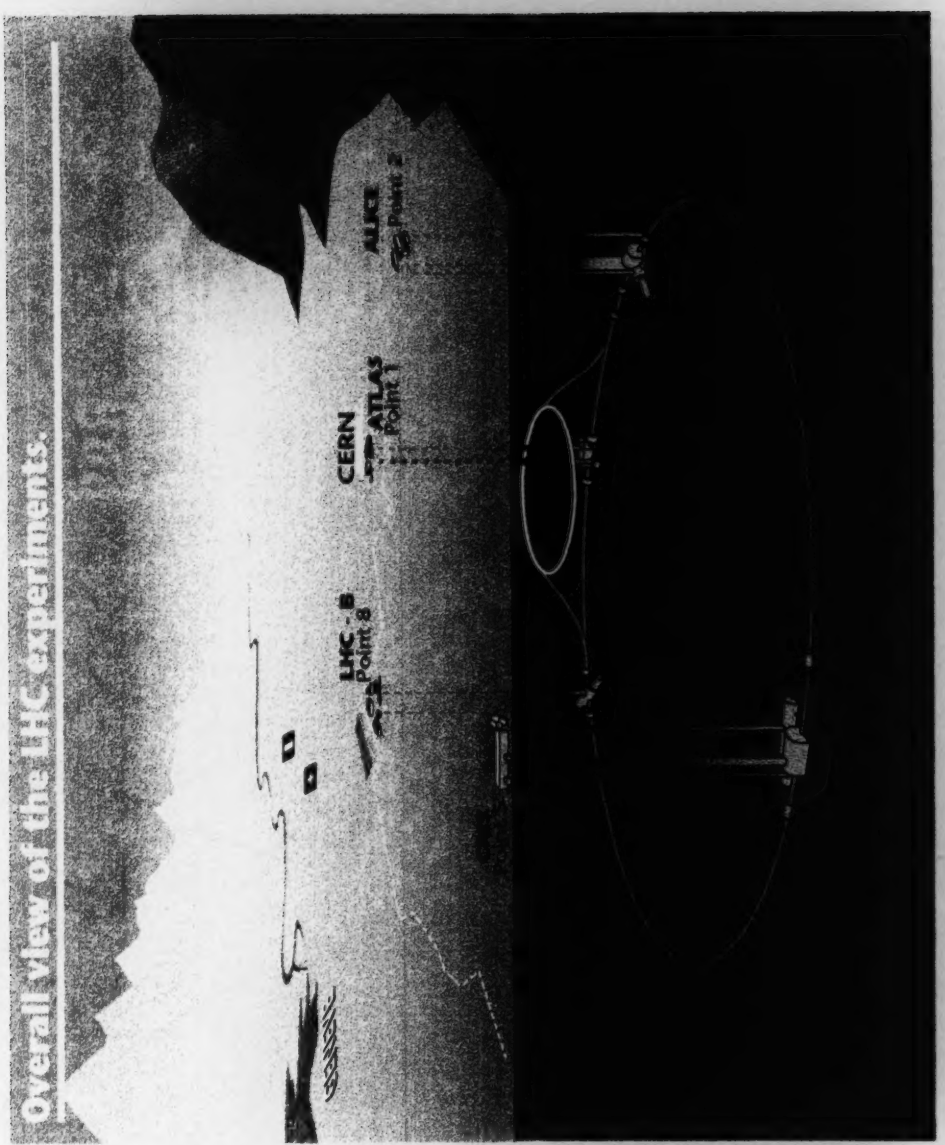

Figure 3.1: An artist's conception of the LHC layout.

LHC General Parameters

Energy at collision	7 TeV
Energy at injection	450 GeV
Luminosity	$1 \times 10^{34}\,\mathrm{cm}^{-2}\mathrm{s}^{-1}$
Bunch spacing	7.48 m
Bunch separation	24.95 ns
Number of particles per bunch	1.1×10^{11}
Luminosity lifetime	10 h

Table 3.1: The specifications of the LHC, copied directly from the official website at `http://wwwlhc01.cern.ch:8050/lhc_proj/owa/lhcp.page?p_number=1000`.

Model. Some of the most important goals, as described in great detail in the ATLAS Technical Design Report[4], are briefly described below.

QCD Processes

There are two main thrusts to the QCD studies that will happen at the LHC. The first is to measure known quantities (such as the distribution of partons within the proton, and the value of the strong coupling constant α_s) with greater accuracy, allowing us to place greater constraints on the existing parameters of our theoretical models.[1][5] The second QCD focus area is to check the predictions of the existing models in the new energy regimes available to the detectors at the LHC, which will allow us to better understand the QCD background processes present in other processes, improving the ability to isolate the physics processes.

Electroweak Gauge Bosons

The LHC beams will result in collisions that can be used to accurately measure the mass of the W boson, as well as the Triple Gauge Couplings[2]. Improved knowledge of these parameters is necessary input to other experiments at other accelerators which depend on these values to produce more accurate results based on their own data. Improved measurements of gauge boson production will provide a more accurate determination of the background processes that may mask new physics.[4]

[1]The main areas being looked at specifically are the proton structure in the parton model, the structure of minimum-bias events, hard diffractive scattering, jet physics, photon physics, Drell-Yan physics, gauge boson production, and heavy flavour physics.[4]

[2]The Triple Gauge Couplings refer to couplings such as $Z^0W^+W^-$, involving the combination of three gauge bosons.

B-physics

The high energy and luminosity of the LHC beams provide excellent opportunities for the study of Standard Model physics involving the "bottom" (or "beauty") quark. The thrust of this portion of the research is to use the data from collisions resulting in one or more b-quarks (about 1% of all collisions[4]) to study *CP* violation, B_d^0 and B_s^0 oscillations, and relative decay rates, all in the hopes of developing a better determination of the *CKM* quark mixing matrix[3],[6] thus assisting other experimentalists as well as theorists in predicting b quark physics.[4]

Top-physics

ATLAS can, at high luminosity, produce approximately 80 million $t\bar{t}$ pairs per year, providing an excellent opportunity to study a variety of physics processes involving this elusive quark. Some of the more interesting studies that can be done include obtaining a more accurate measurement of the top quark mass, and finding a firm upper limit on the mass of the Standard Model Higgs boson.[4]

The "top" (or "truth") quark's high mass also provides an opportunity to search for new physics in the realm of electroweak symmetry breaking, fermion mass generation, and the possible existence of other massive particles.[4]

Since the dominant decay mode for a top quark is to a bottom quark, the detector must be highly capable of b-physics to be an effective tool for t-physics.

The Higgs Boson Search

One of the most desired goals of the ATLAS project is to observe the Higgs boson.[7][8] The Higgs is a particle required within the Standard Model to explain how matter acquires mass. This elusive boson may only be produced through collisions of particle beams with energies and luminosities such as those produced in the LHC. The Higgs is a necessary component of the current Standard Model of particle physics. If it is not observed at the LHC, much of our current understanding of the Standard Model will have to be reexamined; current theory predicts the mass of a Standard Model Higgs Boson to be less than $1\,\mathrm{TeV/c^2}$.[9] Because such energy regimes are easily reached at LHC experiment such as ATLAS, the ATLAS experiment will prove a useful tool regardless of the outcome of a Higgs search.

[3]The CKM matrix is a representation of the probability and capability of quarks to change from one flavour to another during an interaction. It relates the mass and weak eigenstates of the quark families.

The properties of the various Higgs boson searches were used as benchmarks for setting up some the detector's performance parameters. High resolution measurements of photons, electrons, pions, and muons for example, are essential in the search for the Higgs.[4]

The Search For SUSY

Some theories of supersymmetry (or SUSY for short) call for the existence of supersymmetric particles at the scale of less than 1 TeV. If this is the case, SUSY particles could be found at the LHC. As SUSY is one of the best known and most developed extensions of the Standard Model, the study of its nature is one of the primary goals of research at ATLAS. Some of the specific extensions which will be examined are the supergravity (SUGRA) models, the gauge mediated SUSY breaking models, and the R-parity breaking models.[4]

Other Physics Beyond the Standard Model

One example of the new physics that can be examined with the new energy regime is that of the technicolor models, in which hadrons form that are not colour neutral. These models provide an alternative to the Higgs boson in theory, and they may be detectable if they occur at mass scales below 1 TeV. New gauge bosons (common predictions of extensions to the electroweak gauge group), leptoquarks and excited quarks (which would signify new physics), and monopoles (which may explain charge quantization) are other potential discoveries that can be made at LHC energies. (See, for example, the review in [10].)

3.3 The Components of ATLAS

The individual components of ATLAS are described below.

The components combine to form a detector of high hermeticity. Studying phenomena such as showering demands high hermeticity, as showers must be contained within the detector for the best possible energy measurements. Hermeticity is also required for accurate studies of processes involving energy, as the high hermeticity will minimize the amount of "missing" energy that escapes the detector. The beam pipe itself has a radius of 3 cm,[11] although the beam spot is described by Gaussian parameters $\sigma_x = \sigma_y = 15\,\mu$m, $\sigma_z = 5.6$ cm.[4]

A schematic diagram of the ATLAS layout can be found in figure 3.2 on the next page.

3.3.1 Inner Tracker

The inner tracker is the first portion of ATLAS that a particle with high transverse momentum is likely to encounter after leaving the interaction point. It is capable of determining the location of an interaction vertex with high precision, and identifying the track (and, therefore, the momentum) of a particle in the chamber. In the barrel region, a typical track crosses three layers of high-resolution pixel detectors[4] and eight layers of lower resolution[5] silicon strip detectors. The inner tracker also contains a transition radiation detector. The purpose of this detector is to identify the transition photons emitted by particles of high[6] $\frac{v}{c}\gamma$. The entire tracking system makes use of the 2 T central solenoid magnet to produce its central field.[7][4]

3.3.2 Calorimeter

The ATLAS calorimeter, like any other calorimeter, is responsible for determining the energy of the incident particles. The ATLAS calorimeter is further subdivided into different components, each of which is specialized for measuring the energy of a different type of particle.

All performance figures and designs in this subsection are from reference [12] unless otherwise noted.

Electromagnetic Calorimeter

The electromagnetic calorimeter is the detector that precedes the hadronic calorimeter from the perspective of a penetrating particle. Its primary purpose is to identify particles whose interactions are primarily electromagnetic in nature, such as photons, electrons, and positrons, by absorbing and measuring the energy loss when traversing matter [12].

All particle detectors suffer from the inability to cover the complete 4π steradian solid angle, as there must be gaps for the beam particles to enter through[8]. Most

[4] Each pixel measures $50\,\mu\text{m} \times 300\,\mu\text{m}$.[4]

[5] The resolution is $\approx 200\,\mu\text{m}$.[4]

[6] "High" $\frac{v}{c}\gamma$ means $\frac{v}{c}\gamma \gtrsim 1000$.

[7] The central solenoid is one of the two major components of the ATLAS magnet system. The other main component is used in the muon spectrometer, described in its own section.

[8] The gaps are included by design to allow the shared source beam to pass through the detector and continue on for use by other experiments. Many of the beam particles pass through the

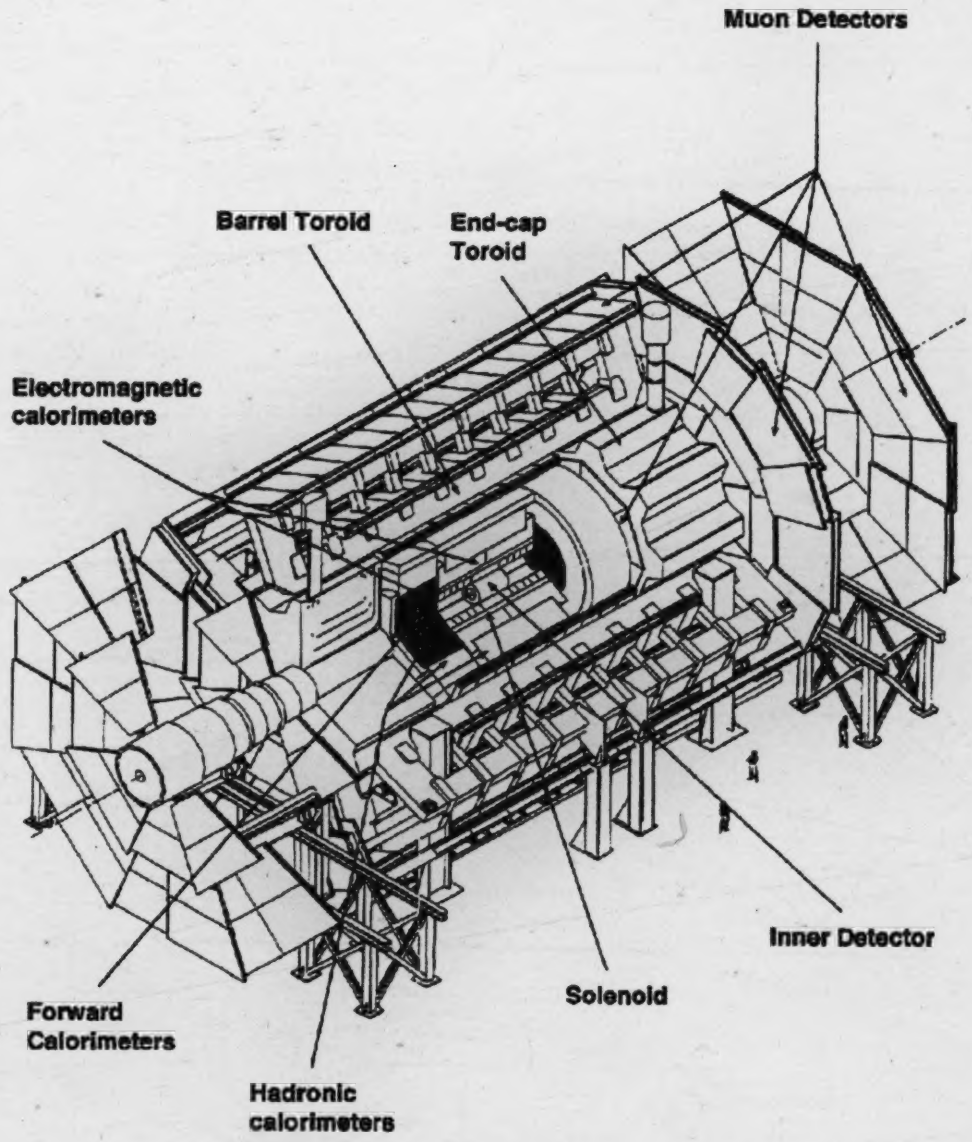

Figure 3.2: A schematic view of ATLAS. The hadronic endcap calorimeters are coloured in red.

detectors also have small cracks where the components are connected, which have a small but measurable impact on the efficiency of detecting particles incident in that area. The electromagnetic calorimeter, which consists of a barrel and two endcaps, employs a rather clever design to circumvent part of this issue. The absorber plates they employ are designed in an accordion-like fashion, assuring that all particles pass through the same proportions of active and passive layers. The lead absorber being used is very soft, and does not maintain the accordion shape easily. This problem is being circumvented by reinforcing the lead with thin sheets of stainless steel [12]. The entire electromagnetic calorimeter will be enclosed in a barrel and two endcap cryostats.

The barrel calorimeter covers the region of pseudorapidity defined by $|\eta| < 1.4$, while the endcaps cover $1.375 \leq |\eta| \leq 3.2$.[12] It is expected to obtain an intrinsic energy resolution of

$$\frac{\sigma}{E} = \frac{(11.6 \pm 0.2)\ \%\sqrt{\text{GeV}}}{\sqrt{E}} \oplus (0.32 \pm 0.04)\ \%$$

for electrons and

$$\frac{\sigma}{E} = \frac{(10.7 \pm 0.3)\ \%\sqrt{\text{GeV}}}{\sqrt{E}} \oplus (0.28 \pm 0.04)\ \%$$

for photons[4].[9]

Tile Calorimeter

The Tile Calorimeter, or Hadronic Barrel Calorimeter, is a sampling calorimeter that uses iron as an absorber.[4] The detector will be located behind the electromagnetic calorimeter.

The tile calorimeter is so named because it uses scintillating tiles as the active material which are embedded in the absorber material. The tiles are arranged into one barrel and two extended barrels.[10] When assembled, the tile calorimeter will have an inner radius of 2.28 m and an outer radius of 4.25 m. The barrel covers the pseudorapidity range of $|\eta| < 1.0$, while the extended barrels cover $0.8 < |\eta| < 1.7$[4]. The readout system for the tiles involves wavelength shifting fibers and photomultipliers.

---

interaction point without interacting.

[9] This function will be defined and described in more detail in section 6.1.2 on page 49. In this notation, $a \oplus b = \sqrt{a^2 + b^2}$.

[10] The barrels are closed on the ends by the Hadronic Endcap Calorimeter, which will be discussed in greater detail in the next section and the next chapter.

The intrinsic energy resolution of this calorimeter when dealing with pions was found to be

$$\frac{\sigma}{E} = \frac{(52.0 \pm 0.6)\ \%\sqrt{\text{GeV}}}{\sqrt{E}} \oplus (4.1 \pm 0.1)\ \%$$

during the 1996 testbeam[4].

Hadronic Endcap Calorimeter

The Hadronic Endcap Calorimeter, or HEC, will be the focus of this thesis. Its primary responsibility is to detect and measure the energy of hadronic particles in the solid angles defined by $0 \leq \phi \leq 2\pi$ and $1.5 < |\eta| < 3.2$.[12]

The HEC itself is a large circular wheel with an outer diameter of $2.030m$. The mass of the wheel is dominated by large copper segments, each of which subtends an angle of $\frac{\pi}{16}$ radians in the ϕ variable. The spacings between the copper plates within these 32 segments are instrumented with layers of electronics used in data collection.[12]

The intrinsic energy resolution of this calorimeter when dealing with pions was found to be

$$\frac{\sigma}{E} = \frac{(75 \pm 2)\ \%\sqrt{\text{GeV}}}{\sqrt{E}} \oplus (5.0 \pm 0.3)\ \%$$

during the 1996 testbeam[4].

This section of ATLAS will be described in more detail in the next chapter.

The Forward Calorimeter

The Forward Calorimeter (FCAL) was a particularly challenging detector to design. It experiences intense radiation, given its proximity to the beam line and thus its coverage of high η values.[4]

The FCAL is comprised of three components. The first uses copper absorber, while the other two use tungsten. The active portion of the detector is liquid Argon. The unusual part of this design is the metal matrix with concentric tubes and rods parallel to the beamline as the absorber material. This uncommon geometry allows energy deposited by interactions in gaps as small as $250\,\mu$m to be measured.[4]

The intrinsic energy resolution of this calorimeter when dealing with pions was found to be

$$\frac{\sigma}{E} = \frac{(80.9 \pm 15.5)\ \%\sqrt{\text{GeV}}}{\sqrt{E}} \oplus (7.7 \pm 1.2)\ \%$$

during previous studies[4].

3.3.3 Muon Spectrometer

The Muon Spectrometer, unlike some of the previous systems, is not a calorimeter. It is, instead, a spectrometer composed of magnets and high-precision tracking chambers. The air-core toroidal magnets are designed to maintain the magnetic fields perpendicular to the direction of the muons. (This is accomplished with the aid of a design that allows the different magnet geometries in the barrel and endcap portions to mesh effectively and efficiently.) The system covers the pseudorapidity range $|\eta| < 2.4$, with a single-wire resolution of approximately $80\,\mu$m.[4]

The muon spectrometer also employs eight barrel toroid magnetic coils, as well as 16 interleaved end-cap coils, to form a magnetic region which slows the escape of the muons which pass through the inner portion of the detector. These magnets produce a non-uniform magnetic field which guides muons through the trigger chambers and precision tracking chambers. The expected momentum resolution of the detector ranges from $2 - 10\,\%$ at full ATLAS production for muons with up to $1\,\mathrm{TeV/c}$ transverse momentum[13].

3.3.4 Trigger And Data Acquisition System

The LHC will produce beams with sufficiently intense luminosity that there will be an interaction rate of $\approx 10^9\,\mathrm{Hz}$ when ATLAS is in operation, while the storage will be limited to $\approx 100\,\mathrm{Hz}$.[4] This difference will be dealt with by the trigger and event filter systems, which will systematically analyze the data and decide which events are worth recording. Obtaining this rejection factor of 10^7, while still retaining the ability to detect rare events such as Higgs production, is difficult to do.

The triggering system is divided into two "levels." The Level 1 trigger is designed, through the use of various coincidence and veto triggers, to identify muons, electrons, photons, jets, tau leptons decaying into hadrons, and large missing and total transverse energies. This trigger also provides "region of interest" information, indicating where one might find the interesting processes.[4] The region of interest information is used by the Level 2 trigger to determine which portions of the detector contain information worth retaining, and transfers that information from the read out buffers that were filled by the Level 1 trigger. This level of trigger should be able to reduce the data rate to the desired $1\,\mathrm{kHz}$. The event filter trigger level then reduces this to the required $100\,\mathrm{Hz}$.[4]

3.3.5 Computing System

The computing requirements of ATLAS will be remarkable. The ATLAS experiment is expected to have a lifetime of about 10 years, and should produce about one Petabyte of data per year. The necessity of world wide access to this data places heavy demands on the system.

The first proposed method to handle such an influx is to preprocess the data (through the Level 1, Level 2, triggers and Event Filter) soon after its collection, thus reducing the final load on the analysis processors, while reducing the amount of data that needs to be transferred from point to point. Another method that is implemented to reduce loads on the network is to distribute the data among sites other than CERN as well. This reduction on the network load will help cut down on the necessary transfer times from point to point. This form of distributed computing will be aided greatly by the idea of the GRID, a network concept developed at CERN as a new alternative to the World Wide Web.

For more information on the GRID, look at `http://www.eu-datagrid.org/` with your favourite web browser.

Chapter 4

The HEC and its Design

The focus of this chapter will be on the purpose and design philosophy of the HEC. The individual subsystems of the HEC will be discussed in the sequence in which a signal from an interaction moves through the system.

4.1 The Location and Purpose of the HEC

The HEC's planned destination in ATLAS will be immediately behind the electromagnetic endcap calorimeters (from the perspective of an incident particle) and before the muon spectrometer. (The HEC is indicated by the upper arrow to the Hadronic calorimeters in figure 3.2 on page 25.) It will subtend the range $1.5 < |\eta| < 3.2$, and will be primarily responsible for measuring the quantity and distribution of hadronic energies. These results will then be compared to the expected behaviour of hadrons, photons, and charged leptons.

The hadrons are studied in detail by reconstructing the showers generated by their interactions in the copper plates. The progression of the showers is sampled at various points allowing the energy and spread of the showers to be determined. Each step of the process will be described in more detail in the following sections.

4.2 Design of the HEC

The Hadronic Endcap Calorimeter is a sampling calorimeter[1] which uses copper as the absorber and liquid argon as the active material. The electrons freed from the liquid argon after the passage of particles are then collected by readout electrodes which are later interpreted as an energy deposit.

[1] For a summary of sampling calorimetry in general, see section 2.4.

The design and construction of the hadronic endcap calorimeter is the joint responsibility of several countries and institutes, of which the University of Alberta is a member.

4.2.1 The Copper Absorbers

Unless otherwise specified, all physical specifications in this section are from reference [12].

The HEC is divided into two endcaps, which are positioned concentric with the beam line, with the front of each endcap 4262 mm from the interaction point. Each endcap is composed of two distinct wheels of modules. The "front" wheel (ie. closest to the interaction point) has 24 layers of 25 mm thick copper absorbers, while the rear wheel has 16 layers of 50 mm thick absorbers. Each wheel has one layer of copper absorber half the thickness of the layers in the rest of that wheel on the side closest to the interaction point. The first 9 layers of absorber in the front wheels have an inner radius of 372 mm, while all other absorbers in both modules have an inner radius of 475 mm. The outer radius of all 42 layers of absorber is 2030 mm. This can be seen more clearly in figure 4.1 on the following page.

Each wheel is further subdivided into 32 wedges or modules, which together cover the 2π radian ϕ range of the outgoing particles. The layers of copper in each wedge are stacked vertically, and are fastened with 7 tie rods per module. The tie rods in the front modules have diameters of 12 mm, while the tie rods in the rear modules have diameters of 16 mm. The heavier tie rods are required in the rear modules as the copper absorbers in those modules are thicker and hence heavier than in the front modules. The mass of a front module is ≈ 2100 kg, while the mass of a rear module is ≈ 2800 kg.

The tolerance on the variations in thickness in all copper plates is 0.050 mm. The tolerance on the flatness of a face is 0.5 mm for the 25 mm thick plates used in the front modules and 0.25 mm for the 50 mm plates used in the rear modules. The copper used in the manufacturing process is quarter-hard copper with density between $8.89\,\mathrm{g/cm^3}$ and $8.94\,\mathrm{g/cm^3}$.

4.2.2 Readout: The EST and PAD Boards

Unless otherwise stated, all physical specifications in this section are from reference [12].

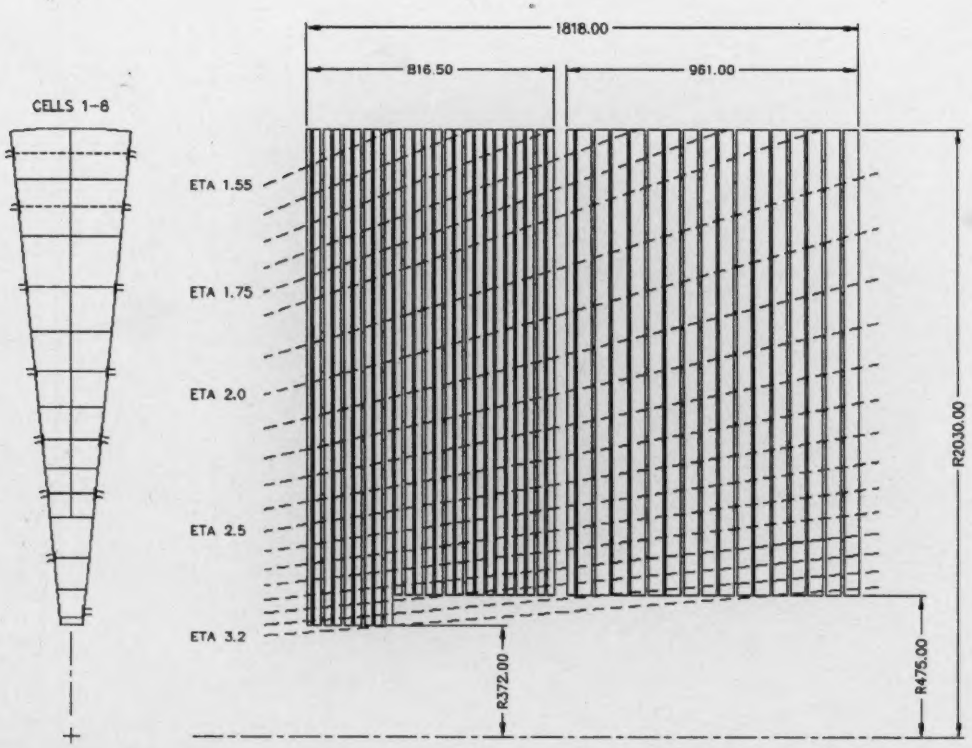

Figure 4.1: A side view of a single wedge of the HEC wheel. The interaction point is to the left, parallel to the dashed line, where the *eta* lines intersect.

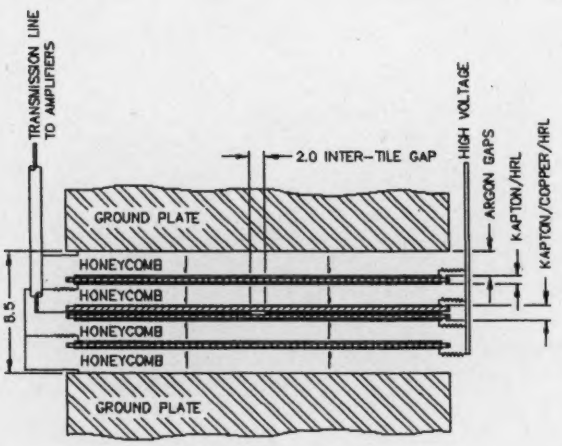

Figure 4.2: A close-up view of the gap structure between two layers of absorber in the HEC.

The copper absorbers in both modules are spaced 8.500 mm apart. These liquid argon gaps are where the actual shower sampling takes place. (See figure 4.2.) Each gap contains EST (*E*lectro*S*tatic *T*ransformer) and PAD data collection boards (each 0.685 mm thick), and four layers of honeycomb spacers (each 1.774 mm thick). These spacers then define four subgaps for the liquid argon that are each 1.954 mm wide. The gaps are instrumented with read-out structures forming an electrostatic transformer.[12] Each gap contains one central board containing read-out electrode pads, two boards that are part of the EST, and "honeycomb" shaped spacing mats to maintain physical separations between the layers. The EST technology was chosen to optimize the signal-to-noise ratio, while minimizing the high voltage requirements.

The nominal operating voltage of the system is 2000 V, with a maximum operating voltage of 2500 V.

The EST-PAD combination is arranged in the electronics in various cells. The cells can be analyzed individually, allowing for versatile combinations of cells to be examined for shower characteristics. This flexibility will be thoroughly examined, and an optimum arrangement for these cells for each beam impact point will be sought. The goal is to find a set of cells that contains enough of the shower to be confident that the majority of the energy was collected, while still keeping the collection of cells small enough to prevent unnecessarily large amounts of electronics

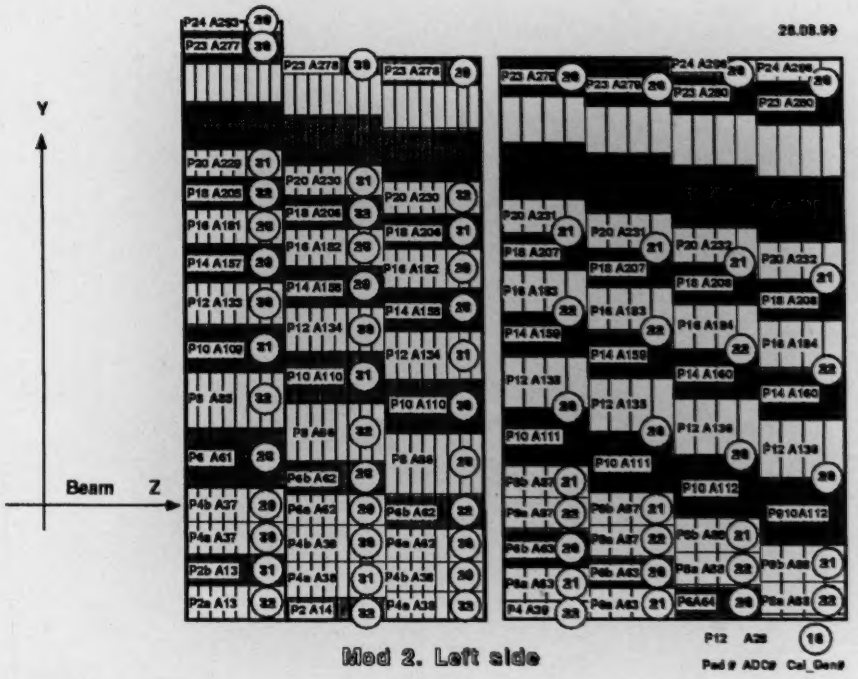

Figure 4.3: A side view of a single wedge of the HEC wheel. The cells are labelled. The cell number for a rectangle is the number following the A in that rectangle. For example, the two rectangles labelled "P6a A62" and the two labelled "P6b A62" combine to form cell 62. Comparing cell 62 to cell 14 makes it clear that different cells have different volumes.

noise from being collected in the data. The optimal cell collection, or cluster, will depend on the geometry and size of the shower, so the clusters selection will also depend on the original parent particle that initiates the shower. The cells are of unequal sizes, and are designed to subtend a particular solid angle ($\Delta\eta \times \Delta\phi$) rather than a specific volume (see table 4.1 on the following page,) which will make the cluster selections more efficient in the analysis stages. A cut-away view of a single HEC module with the cells labelled can be seen in figure 4.3.

4.2.3 The DAQ System

The data collected by the electrodes will be collected first by the read-out architecture. This architecture is organized such that there are four main read out locations evenly spaced about each wheel. This architecture, a combination of preamplifiers,

HEC granularity

η	$(\Delta\eta \times \Delta\phi)$	
	Front	Rear
$1.4 - 2.5$	0.1×0.1	0.1×0.1
$2.5 - 3.1$	0.2×0.2	0.2×0.2

Table 4.1: The granularity of the HEC.

shapers, pipeline memory, digitization, and digital filtering, will collect the data before passing it along to the Level 2 buffers.[12] This equipment will be easily upgradable and up to date, as many components are in rooms separate from the detector itself. Once the data has passed through the Level 2 buffers, it will be routed through the clock and control signals in the trigger room, after which it is finally delivered to the DAQ system for permanent storage.

Chapter 5

The August 2000 Testbeam Conditions

The testbeam conditions for the HEC are somewhat different from the conditions that will be implemented in the ATLAS arrangement. The testbeam setup and the differences between this and the final ATLAS setup are discussed here. The data acquisition software specific to the testbeam will also be described.

5.1 Testbeam Environment and Design Philosophy

5.1.1 H6 Beamline

The testbeam studies are conducted at the CERN Prevessin site in France. This is the home of the H6 beamline of the CERN SPS, which is employed in the testing of HEC modules. This beamline is capable of delivering pions, electrons and muons of both charges and a range of momenta. The electrons analyzed in this thesis have a momentum range of $6\,\mathrm{GeV/c} \leq p \leq 147.8\,\mathrm{GeV/c}$ while the pions have momentum $6\,\mathrm{GeV/c} \leq p \leq 200\,\mathrm{GeV/c}$. For more details about the H6 beamline, see reference [14].

5.1.2 The Cryostat

The HEC is designed to operate at low temperatures ($87\,\mathrm{K} - 89\,\mathrm{K}$) in liquid Argon. For the testbeam setup, that means HEC modules under examination are placed in a cryostat which is then filled with 90 K liquid Argon. The cryostat is then placed in the beam's path. A circular window in the upstream side of the cryostat permits the passage of beam particles into the cryostat with minimal interaction. The cryostat is large enough to contain six modules, if it is arranged with three front modules

and three rear modules.

The cryostat is mounted on horizontal tracks (which run perpendicular to the testbeam direction) and is motorized. In this way, the horizontal position of the testbeam's impact point can be modified by moving the cryostat itself.

5.1.3 Orientation of Modules

Once in the testbeam cryostat, the HEC modules are oriented with the flat face perpendicular to the incident particles. This is contrary to the final arrangement within ATLAS where the particles incident on the HEC will come in (approximately) along lines of constant η. Thus, the electronics towers built within the HEC have been designed such that a single tower is centered around a constant value of η. This will minimize the number of cells needed in clusters at ATLAS, and thus minimize the noise in the signal. The testbeam cryostat is not large enough to orient the modules in this fashion and so the testbeam cannot take advantage of the pointing geometry the HEC was designed with. Figure 5.1 on the following page shows a side view with the comparison of the two configurations.

In the August 2000 testbeam, six modules were tested. The three front and three rear modules used included samples of each type of module from both the Canadian and Russian manufacturers.

5.2 The Testbeam Setup

5.2.1 Trigger and DAQ Systems

The triggering system for the HEC testbeam has several stages devoted to distinguishing between the three primary particle types (electrons, pions, and muons.) A series of scintillators is placed in the beamline, and is combined in the trigger logic by an AND gate, ensuring that the recorded event corresponds to an actual particle coming down the beam pipe, and not random noise from elsewhere. Another scintillator (referred to as "hole") is designed to surround the beamline without crossing it. Data is not recorded if this detector triggers, as that would imply a particle in the beam "halo" of unknown energy is present. A more stringent requirement is formed by placing two smaller, mutually perpendicular scintillators (whose surfaces are parallel to the surface of the HEC, known as the F1 and F2 scintillators) on the upstream side of the HEC so that their intersection is between the incident beamline and the impact point under examination, thus ensuring that the particle is incident

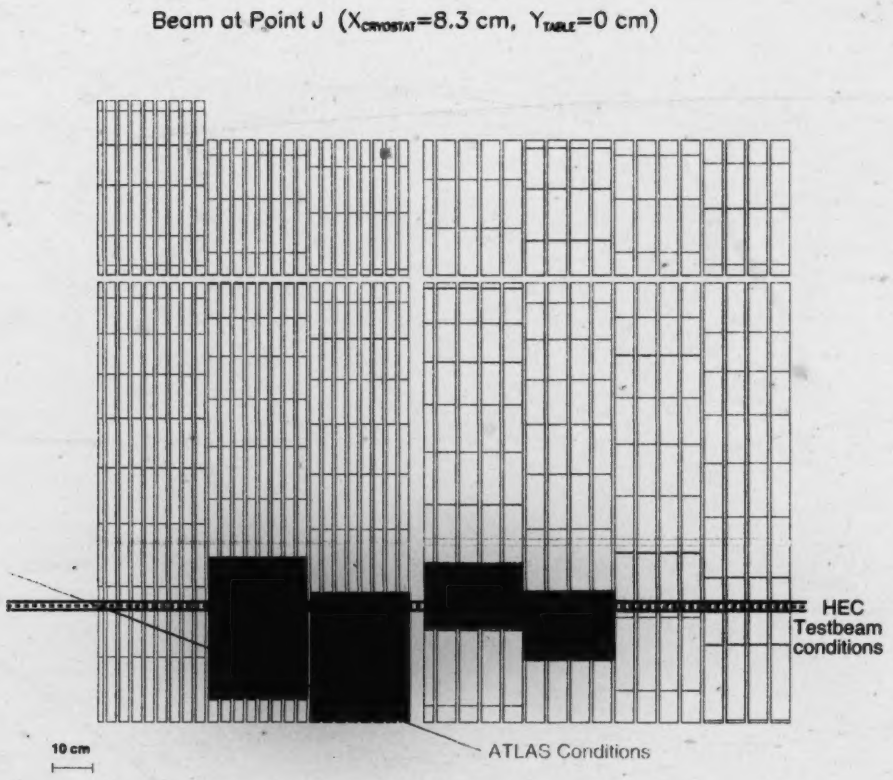

Figure 5.1: A side view of the HEC, with depiction of the cells in the path of the beam. The magenta beam is the kind of path that would be followed by a particle at ATLAS, while the blue path is a path from the HEC testbeam. The yellow cell intersects both paths. The green cell intersects the ATLAS path only, while the three red cells intersect the HEC testbeam path. (The original version of this image can be found in reference [15].)

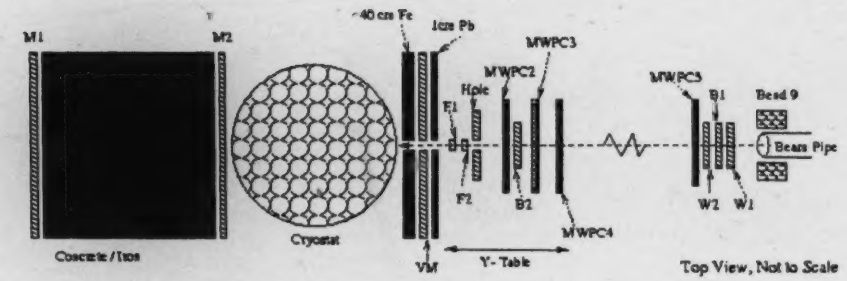

Figure 5.2: A schematic diagram of the triggering system used for the HEC testbeam. Beam particles move from right to left. This image was created by Matt Dobbs.

upon the area under consideration. A schematic view of this trigger system can be seen in figure 5.2.

Once these two criteria are met, the triggers can be used to distinguish between different particle types. Muons are distinguished from pions or electrons through the simple condition that muons are also found in the scintillator detector downstream of the HEC and the concrete and iron walls behind it. Electrons and pions can then be distinguished by the Čerenkov detector, provided their momenta are sufficiently low.[1] Higher energy electrons and pions must be distinguished using software techniques separate from the trigger system.

The DAQ system used in the HEC testbeams is not the system that will be used at ATLAS (since the HEC will be working in conjuction with other equipment when ATLAS begins operation.) Measurements of current registered by the PAD boards are sent to the recording hardware in the beam control hut. This hardware applies the logical triggers required for the particle type being examined, and determines which events correspond to the set of physics being investigated. These are the data that are recorded for later analysis. Note that an adjustable percentage (usually

[1]Experience tuning the signal in the beam hut at the testbeam indicates that the Čerenkov detector is ineffective at separating pions and electrons with momenta greater than 80 GeV/c.

5-10%) of the data is selected at random, to provide a way to ensure that there are no processes taking place that are not registering in the existing physics triggers.

5.2.2 Impact Points

The incident testbeam and the cryostat were steered over 15 specified impact points in these studies, labelled with the first 15 letters of the Roman alphabet (see figure 5.3 on the following page.) All fifteen points were accessible through the target window in the upstream side of the cryostat. The points were selected to test all six modules at various locations and cell geometries. One point, labelled I, was selected to demonstrate the behaviour of the testbeams on a division in the electronics. Although point I falls on a solid portion of the absorber layer, the active areas are divided along the vertical axis immediately beneath it. The upstream side of the HEC modules tested is visible in figure 5.3 on the next page.

Each impact point can be described using two variables which are the Cartesian coordinates (x, y) relative to the origin, given by impact point I. The horizontal position x is adjusted by physically moving the cryostat with respect to the beamline, while the vertical variable y is adjusted through the use of bending magnets. Limitations of the strength and physical extent of the bending magnets prevented the highest energy pions from reaching the impact points not on the $y = 0\,\text{mm}$ level. For example, pions at the lowest impact points (such as point N) were not studied above $180\,\text{GeV/c}$ in momentum.

5.3 The Software

5.3.1 The `hec_adc` Software Package

Once the data have been collected by the DAQ system, they must be analyzed. The first stage of the analysis is accomplished with the `hec_adc` software package.

The `hec_adc` package, described in detail in [16] and [17], interprets and condenses the data collected by the DAQ system. The user can select which analyses will be performed, such as the beam chamber reconstruction, digital or cubic calibration calculations relating current measured to energy deposited, measurement of the energy with user-defined clusters, and which histograms will be filled for analysis. If the built-in options are not sufficient, the user can create new routines, and plug them into existing points in the program code. This allows for a very versatile analysis to be performed quickly. A flowchart is available in figure 5.4 demonstrating

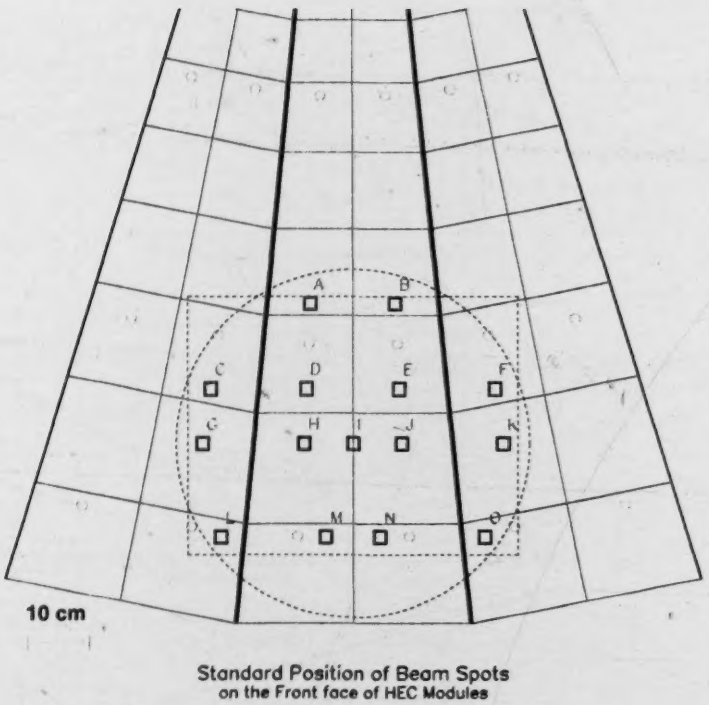

Figure 5.3: The view of the HEC module from upstream. The letters correspond to the 15 predetermined impact points, the red circles mark the tie-rods, and the dotted circle indicates the projection of the cryostat window. The dashed rectangle represents the extent of the area which can be targeted with the current trigger and positioning systems. Solid black lines indicate divisions in the copper, while lighter black lines indicate divisions in the electronic readouts.

the three passes over the data, which may each have their own user-selected analysis code.[2]

The `hec_adc` package has both online and offline versions. The offline version takes full advantage of the versatility already mentioned, while the online version performs a rapid predetermined set of analyses which are designed to serve as indicators of any serious problems with the incoming data. This means that the experimenters collecting the data can see if the recorded data is sensible before the next data run begins. This works because the important information for the data structure is stored at the start of a data file. An analysis of the first 10% of the data in a run can often be completed before the last 10% are collected.[17]

5.3.2 The New Software Package

The software written specifically for this thesis uses a different design philosophy than the pre-existing `hec_adc`. Instead of creating a program that can perform all the calculations necessary for the analysis through user-controlled calls to various optional subroutines, a series of small, specialized modular programs was created that can call each other at the various stages of analysis. Each program was responsible for calculating a different quantity in the analysis, beginning with an iterated fitting routine that resulted in a description of the particular shower, and then proceeding sequentially with programs that use these results to determine all other quantities. Individual analyses (as well as partial analyses) can then be performed. This method allows for more flexibility in the event of alterations to the methodology of analysis, as well as reducing the overhead demanded of the computing system at any given time. It also allows some portions of the analysis to be decoupled from others, allowing the physicist to obtain certain measurements without altering software settings or waiting for the analysis of unnecessary data.

The individual software programs are written in either FORTRAN 77 or C, depending on the task required. The output data files are all in ASCII text format. This increases the demands on the required disk space, but it also allows the data to be read in to any software without the use of specialized or proprietary software libraries. The software package will be released in an open source form to members of the ATLAS community for use in any future analyses in which it may be useful.

[2]This feature was not exploited in this analysis, as a different set of analysis programs were created instead.

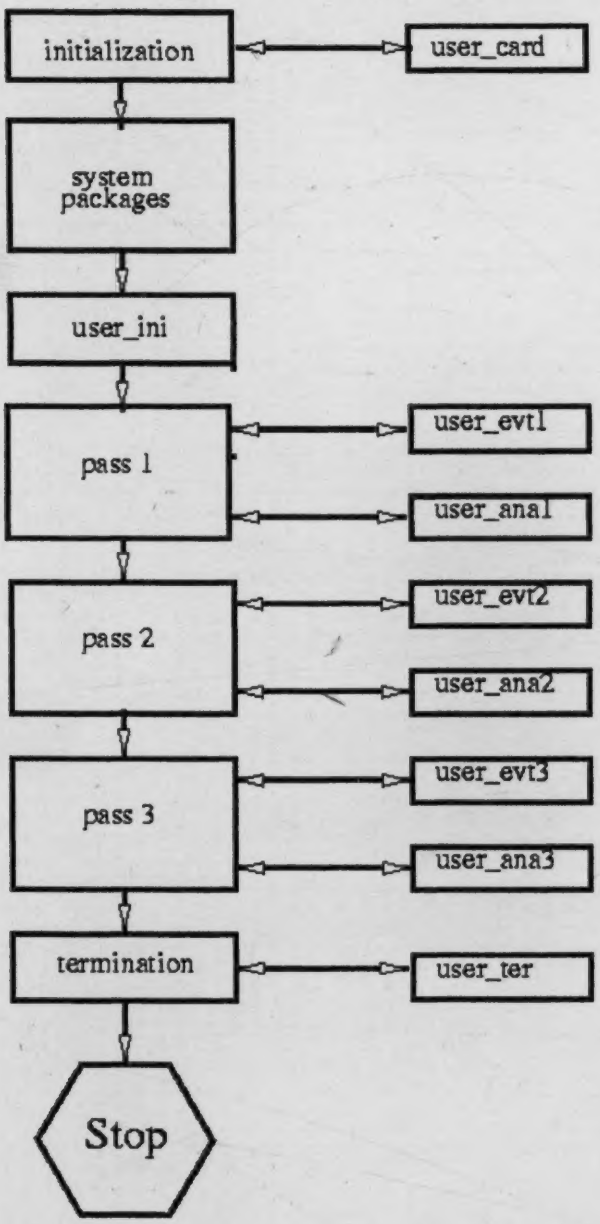

Figure 5.4: A flowchart of the **hec_adc** software package. This image was originally published in [16]. The **user_card** subroutine initializes the system with the user controlled options in the datacard file. The system packages perform the translation of the data from the raw format into a structured format determined by the user options. Each pass allows the user to perform his or her own program code, which is inserted into the user event (called after each event is read from the source data) and analysis (called after all events have been read) subroutines.

The software analyzes the total energy in each cell, sorts them by the energy deposition, and then chooses the most energetic cells (within a certain physical extent) to analyze. Several different cluster sizes and impact points are analyzed, and the results are compiled. The user simply determines which runs to use in that portion of the analysis, and the rest is automatic.

The relationships between the various analysis programs is depicted in figure 5.5 on the following page.[3] The `hec_adc` package is discussed in detail above. The `cellsort` program takes each run, and sorts out the physical cells into the order of energy deposition. (ie. The first two cells on the list would be the two with the most deposited energy.) At this point, human intervention in involved, examining this list and comparing it to a design schematic of the HEC modules being used, ensuring that there are no noisy cells, high voltage trips, or other deviations from theoretical predictions of the shower size and shape as discussed in chapter 2.[4] The `analyze` program iteratively fits gaussian distributions to the output of the `hec_adc` program, using five iterations to close in on the actual data with a fit width of just over 4 standard deviations. (The initial range is broad, with initial guesses determined by manually examining the data. This provides a means of obtaining the analysis input that is independent of previous analyses.) The `nrg_res` program computes the energy resolution for each impact point and cluster size, while `nrg_res2` computes the corresponding intrinsic energy resolutions. At this point, the analysis forks, computing differing results. The `alphaem` and `make_alphas` programs work in sequence to calculate the α_{em} and α_h quantities, the linearities, and the fraction $\frac{e}{h}$. The line of computing that begins with `plotter` calculates and plots the evolution of all variables with changing cluster sizes.

Unfortunately, the goal of creating a single universal algorithm for all conditions and particle types has proven difficult to achieve. The differences in the distributions for different incident particle types, as well as compensating for different types of noise in different runs, has proven to be a taxing exercise, and no single algorithm has been found. Therefore, for a small number of runs, the analysis steps were performed manually by following as closely as possible to the original algorithm,

[3]This paragraph, describing the role of the individual programs in the analysis process, uses terminology that won't be defined until the next chapter in this thesis. This should not be a large concern, as this section merely states which quantities are calculated by a particular program, without delving into detail about the results of those calculations.

[4]There were no such problems in the final set of data used in the analysis. Lists of these runs can be found in the relevant analysis chapters.

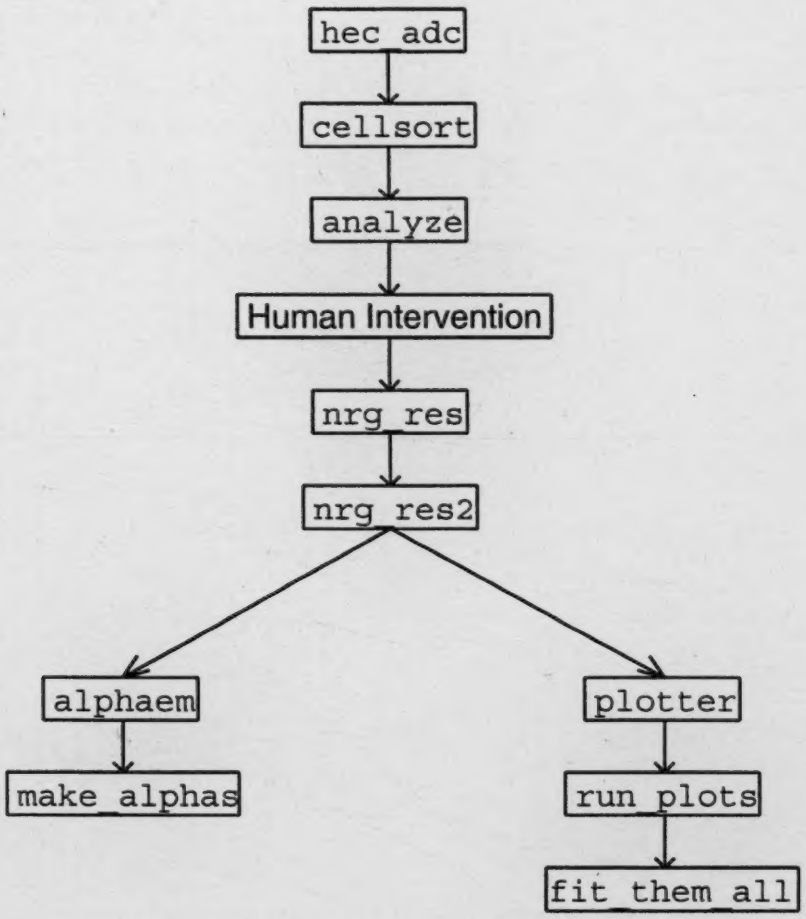

Figure 5.5: A flowchart depicting the structure of the new programs.

differing only in steps for which the algorithm fails. The techniques used for handling these difficulties are discussed on a problem-by-problem basis in chapters 7 and 8.

Chapter 6

The Interesting Quantities: Energy Resolution and Other Measured Quantities

Four different quantities are being studied to determine the performance of the HEC. The first quantity is the energy resolution, a measure of a detector's ability to accurately determine the energy of an incoming particle. The second quantity is a measure of the conversion factor between the current recorded by a detector and the energy of the particle that instigated the shower. The third quantity, known as linearity, is the measure of the variation of the aforementioned conversion factor throughout the various data collection runs as a function of energy or impact point. The fourth quantity, $\frac{e}{h}$, is a comparison of the detector's response to electromagnetic events to its response to hadronic events.

The origin of these quantities and the effects of the testbeam setup on their expected values will be discussed. Understanding these quantities will lead to an understanding of the performance of the calorimeter.

6.1 Energy Resolution

The energy resolution is an intrinsic property of a detector, describing its ability to accurately determine the energy of an incident particle by relating the current recorded by the detector to the energy of the particle that instigated the shower.

To determine the energy resolution of a detector, one must first measure the mean signal E and the width σ of the signal produced by particles in a shower as measured in the readout channels. These data can then be plotted, and the energy resolution can be extracted via a fit to the data.

The energy resolution is a function of the form

$$\frac{\sigma}{E} = \frac{A}{\sqrt{E_0}} \oplus B \oplus \frac{C}{E} \tag{6.1}$$

where E_0 is the nominal beam energy, $\frac{A}{\sqrt{E_0}}$ is the sampling term, B is the constant term, and $\frac{C}{E}$ is the linear term.[1].

The sampling term is related to the random fluctuations in the detector signal, which in turn is related to the uncertainty in the number of particles produced in a shower. Since the number of particles produced in a shower is proportional to the energy of the particle that instigated the shower, the sampling term acquires a $\sqrt{E_0}$ dependence.

The constant term is related to such quantities as leakage and calibration errors, which serves primarily as an expression of the non-uniformity of the detector. It is a constant that is determined by the geometry and configuration of the detector itself. The contribution to this term due to leakage should be reduced when the complete HEC wheel is in operation in ATLAS, and a larger solid angle is subtended. The contribution due to calibration errors may also be improved over time as the detector is studied in full operation.

The linear term is primarily related to the electronics noise within the detector. Therefore, it is proportional to the specific electronics included in the system, which is in turn related to the definition of the clusters. A cluster which encompasses a greater physical volume of the detector will also include more electronic readout components, each of which makes a small contribution to the total electronic noise in the system. This term would be reduced if the physical layout of the testbeam permitted us to take advantage of the pointing geometry of the detector, as we would then require fewer clusters to encompass the volume of the shower. The implications of this statement are discussed more completely in subsection 6.1.1.

6.1.1 Clusters and Energy Resolution

As mentioned in subsection 4.2.2, a collection of cells within the HEC detector can be treated as a single unit, called a cluster. When combined in this fashion, the cells behave like puzzle pieces which can be combined (through the addition of all of the energies deposited in these cells) to give more complete picture of the shower being studied. When analyzing an event, one should select a cluster to ensure that

[1]In this thesis, $\oplus$ signifies addition in quadrature such that $x \oplus y = \sqrt{x^2 + y^2}$

most (if not all) of the shower's energy is deposited within the cells of the cluster. However, one should also be careful not to select a cluster that is too large, as the linear term of the energy resolution (the $\frac{C}{E}$ term in equation 6.1 on the page before) would increase accordingly.

The clusters in the testbeam setup will contain more cells (and be "larger") than the clusters required in ATLAS to detect a single incident particle.[2] This is because the physical constraints of the testbeam setup do not allow the experimenter to take advantage of the pointing geometry of the detector. (See figure 5.1 on page 38 and the discussion in section 5.1.3.)

6.1.2 Intrinsic Energy Resolution

The intrinsic energy resolution of a detector is a slight modification of the energy resolution discussed in section 6.1. The intrinsic energy resolution takes advantage of the fact that electronics noise can be measured in an experiment, and can be accounted for directly within the analysis.

The intrinsic energy resolution is given by the equation

$$\frac{\sigma}{E'} = \frac{A}{\sqrt{E'_0}} \oplus B \tag{6.2}$$

This is very similar to equation 6.1 on the page before, but in this case, the noise term has been subtracted. The intrinsic resolution can be calculated by beginning with the same Gaussian distribution of signal found for the normal energy resolution, and then subtracting the measured electronics noise from it. Once the noise subtracted signal is obtained, the results may be plotted, and fit to equation 6.2. The intrinsic energy resolution is advantageous over the normal energy resolution in that it is independent of the noise in the electronics of the system, which eliminates the dependancy of the results on the specifics of the readout electronics, and other such factors which are not directly related to the physics processes being studied. The mean signal E has been replaced by E', to remind the experimenter of the change in the mean resulting from the subtraction of noise from the signal.

[2] ATLAS will be looking for incident jets rather than single particles, however, so the actual cluster size at ATLAS should be larger than that found in this analysis.

6.2 Conversion Factor α

The second important quantity is the conversion factor α. As described in chapters 2 and 4, when a particle is incident on the detector, a shower will be instigated.[3] These showers then produce ionized atoms in the liquid argon layers of the detector, with the freed electrons producing currents in the PAD boards, which are interpreted as a signal.

Thus, the energies of the incident particles are detectable only by the amount of current they produce within the detector. These currents have to be translated into the corresponding energies of the original particles.

The conversion factor α is defined by

$$E_0 = \alpha E \tag{6.3}$$

where E_0 is the nominal beam energy (as defined in section 6.1) measured in GeV, and E is the mean of the signal of a run, which is related to the energy loss in the liquid argon, and is measured in nA.

The variable α will vary depending on the specific hardware, so it may not be identical for all possible impact points of the detector. The variations in the geometry (as well as the corresponding differences in the electronics) of each cell should affect the conversion factor. However, these differences should be small enough to allow for meaningful comparisons of the conversion factor at different impact points.

It should also be noted that, due to the differences in energy deposition processes for electromagnetic and hadronic events, the variable α is dependent on the type of interactions the incident particle is involved in. For this reason, it should be measured for electromagnetic events and hadronic events separately.

The electromagnetic conversion factor α_{em} for a given impact point, defined by

$$\alpha_{em} = \frac{E_0}{E} \tag{6.4}$$

is determined by minimizing the expression

$$\chi^2 = \sum_{i}^{runs} \frac{(\alpha_{em} E_i - E_{0,i})^2}{(\alpha_{em} \delta E_i)^2} \tag{6.5}$$

[3] In quantum mechanics, there is always a chance that there will be no interaction. However, the probability of any electrons or pions passing through this detector without interaction is certainly negligible.

where E_i is the mean of the signal for the i-th run at this impact point (measured in nA), $E_{0,i}$ is the nominal beam energy of the i-th run at this impact point (measured in GeV), and δE_i is the uncertainty of the mean of the signal (measured in nA). The electromagnetic conversion factor should be independant of the energy of the incident electrons and positrons. Past testbeam results indicate it should be on the order of $2.93 \pm 0.03\,\mathrm{MeV/nA}$.[1]

The hadronic conversion factor α_h is determined in a different fashion. A purely hadronic conversion factor should, like the electromagnetic conversion factor, be independant of the energy of the particle instigating the showers. However, the pions which initiate our hadronic events experience interactions that are both electromagnetic and hadronic. Therefore, the conversion factor for pions[4] is measured as a function of energy (since the relative proportion of hadronic and electromagnetic events will be determined by the energy available to the interacting particles) and then used to determine a purely hadronic conversion factor. The process involved will be discussed in more detail in section 6.3.

6.2.1 Linearity

The linearity of a detector is, in effect, a measure of its consistency; a perfectly linear detector would have the same electromagnetic conversion factor for all impact points and beam energies. The linearity is studied by comparing the conversion factor of each impact point to some sort of average or reference conversion factor.

The linearity of the HEC will be determined by measuring α_{em} for each impact point, finding the weighted average of these conversion factors, and then plotting the ratio of the weighted average conversion factor for all impact points to an individual impact point's conversion factor. A general rule of thumb is that a linearity of 1% (ie. all ratios fall between 0.99 and 1.01) is considered a good linearity. The linearity is only used for the electromagnetic conversion factor, because the energy dependance of the pion's conversion factor ensures that the variation of the pion conversion factor is more than 1% of its value.

[4]It should be noted that the "conversion factor for pions" is really a weighted average of the conversion factors for electromagnetic and hadronic processes. So, for example, if a parent pion deposits half of its energy through hadronic processes, and the other half through electromagnetic processes, then the conversion factor for that pion shower would be the mean average of the electromagnetic and hadronic conversion factors.

6.3 The Fraction $\frac{e}{h}$

As mentioned in chapter 2 and section 6.2, electromagnetic events and hadronic events produce different characteristic signals within a detector. One way to measure the difference is to compare the electromagnetic and hadronic conversion factors α_{em} and α_h.

One way to facilitate this comparison is to measure the fraction $\frac{e}{h}$. e is a variable which represents the response of the HEC to purely electromagnetic events, while h represents the response of the HEC to purely hadronic events. Since there are no purely hadronic events available in this testbeam (as described above), the experimenter is forced to improvise.

Let us represent the response of the detector to electron events as $e = \frac{E}{E_0}$, as electron showers are purely electromagnetic. Let us represent the response to pion showers as π. Let us also represent the fraction of electromagnetic events present within a pion shower of total energy E as $f(E)$. Thus, we find that

$$\pi = ef(E) + h(1 - f(E)) \tag{6.6}$$

With some algebraic manipulations, we find that

$$\frac{e}{\pi} = \frac{e/h}{1 - (1 - \frac{e}{h}) f(E)} \tag{6.7}$$

where $f(E) = 1 - \left(\frac{E}{E_0'}\right)^{-0.15}$ and E_0' is the parameter $E_0' \approx 1\,\text{GeV}$ [18]. The fraction $\frac{e}{\pi}$ is

$$\frac{e}{\pi} = \frac{\alpha_\pi(E_0)}{\alpha_{em}} = \frac{E_0}{\alpha_{em} E_\pi} \tag{6.8}$$

where E_π is the mean of the signal obtained from pion run data, measured in nA, and α_{em} is the weighted average conversion factor over the points along the detector's $y = 0$ position.[5] The value of the fraction $\frac{e}{h}$ can then be determined by doing a fit to this data, as this is the only remaining unknown quantity. Past testbeam results indicate an expected value on the order of 1.5 is reasonable.

[5] The reasons for using a subset of all impact points will be discussed in more detail in chapter 7.

Chapter 7

The Electron Testbeam Results

This chapter contains the results of the analyses of the electron data from the August 2000 testbeam period. It will culminate with the measurements of the energy resolution, electromagnetic conversion factor, and linearity as defined in the previous chapter, and comparisons of these results of the independent June 2000 analysis and to the predictions made in chapter 2. The June 2000 data is chosen as the comparison data, as it is the most comparable testbeam; it examined different HEC modules, but all other hardware and methodology were identical to that in the August 2000 testbeam. The modules used in the June 2000 testbeam were, naturally, built to the same set of design specifications as the modules used in the August 2000 testbeam. This analysis will use software independent of previous analyses, and will also analyze data at impact points that do not fall on the $y = 0$ line of the HEC modules used in the testbeam.

Before these analyses and comparisons can be made, however, the data being studied and the numbers of cells in a cluster must be determined.

7.1 The Selection of the Data Subset

HEC testbeams have been performed on a regular basis since 1997. This analysis will focus on a portion of the data collected in August 2000.

The portion of the August data set to be studied was determined by selecting beam impact points that provided the greatest extent of coverage of the detector and its electronics. (See table 7.1 on page 60.) The points selected for study are those labelled E, G, I, J, K, and N.[1] (See figure 7.1 on page 55.) These impact points fall along two lines. The impact points selected along the horizontal line

[1]The June 2000 testbeam examined only points G, H, J, and K.

will demonstrate the behaviour of each of the modules, as well as the effect of the incident beam falling on a division in the electronics (at point I.) The impact points selected along the vertical line are chosen to demonstrate the effects of the various geometries[2] of the cells and clusters. While ATLAS will take advantage of the HEC's pointing geometry, the testbeam conditions do not. As such, clusters chosen to contain a certain number of cells will have differing volumes, determined by the vertical position of the impact point.

7.2 Defining Potential Clusters

The signal in each HEC cell is measured, and these cells are then sorted in order of decreasing signal. The signal will consist of energy deposited when a particle penetrates the HEC and some noise from the electronics. Sorting cells by signal will usually ensure that the cells included in the cluster are those with the largest physics signal present. The exceptions to this idea occur when the amount of noise in a cell is greater than the amount of physics signal in that cell. When this occurs, there is either a problem with the electronics causing a large amount of noise, or all the cells which contain significant amounts of energy have already been added to the cluster, with the remaining cells mainly containing noise. The clusters are checked to ensure that the system is not being deceived by unusually large noise in an otherwise irrelevant cell.[3]

Once clusters are selected, several analyses are performed, each with a different number of cells in the cluster. The data for impact point K were analyzed at all cluster sizes from one to eighteen cells[4]. From this, it will be shown in section 7.3 that the optimal cluster size is in the four to six cell range. Since the geometry is slightly different for each impact point, all impact points were examined at these three sizes to determine the optimal cluster size.

[2]Although each cell of the HEC has a different volume, and therefore different amounts of electronics, all are designed to subtend the same solid angle $\Delta\eta \times \Delta\phi$ when viewed from the interaction point.

[3]More specifically, the list of cells in the detector, sorted by their average energy deposition over the course of the run, was manually compared to a schematic diagram of the HEC to ensure that the cells were adjacent, and that they corresponded to the physical shape of a shower as predicted by theory in Chapter 2.

[4]The numerical analysis ran as high as 20 cell clusters, but the 19 and 20 cell clusters had uncertainties too large for any meaningful conclusions to be drawn.

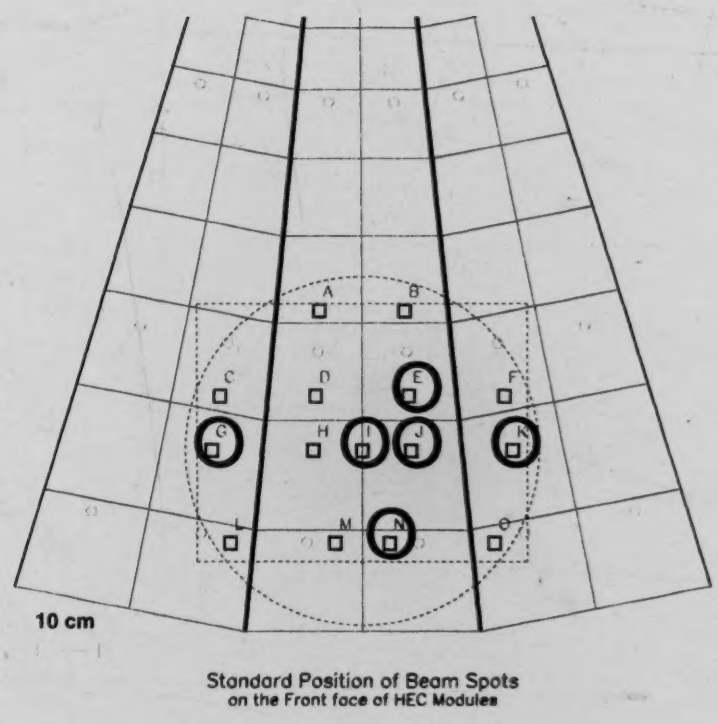

Figure 7.1: A diagram of the face of the 3 front HEC modules used in the testbeam. Impact points are marked by squares with their corresponding letter labels, while the impact points being examined in this analysis are circled in black. Solid black lines indicate divisions in the copper, while lighter black lines indicate divisions in the electronic readouts.

7.3 Optimizing Cluster Sizes Using Point K Data

The possible cluster definitions as a function of energy for impact point K were determined. The energy per cluster from each run were fit to a Gaussian distribution to find the mean and standard deviation of the signal (given in nA). (See figures 7.2 on the next page and 7.3 on page 58.) Some runs produced data which do not form a Gaussian distribution. The most common cause of such an anomaly is the absence of data from an important cell. This is almost always the result of a trip in the high voltage power supply, which would then leave a portion of the detector inactive for part of that run. Afflicted runs are characterized by a long low energy tail in the energy distribution. (See figure 7.4 on page 59, for example. The first iteration of this fit failed completely, and required manual intervention to obtain the fit seen here.) Another notable cause for concern was an apparent problem with the data for runs taken between two equipment accesses (see figure 7.5 on page 64)[5]. The few runs afflicted by those accesses are all for electrons at a beam momentum of 119.1 GeV/c.[6] Fortunately, this is the momentum at which both secondary and tertiary beam sources were available, so data were collected at a beam momentum of 119.8 GeV/c with the other beam source, which "fills in" the gaps in the resolution plots that might have otherwise occurred at 119.1 GeV/c.

Using the mean energy E and the standard deviation σ determined from the Gaussian fits for each run, the optimal size of the cluster was determined by first calculating the resolution and intrinsic resolution of the detector with varying cluster sizes (see figures 7.6 on page 65, 7.7 on page 66, and 7.8 on page 67), and then examining the changes in the fitted parameters A and B in the distribution

$$\frac{\sigma}{E'} = \frac{A}{\sqrt{E_0}} \oplus B$$

as a function of cluster size. As can be seen (by the rapid increase in the size of the error bars which remain consistent with earlier numbers) in figures 7.9 on page 68 and 7.10 on page 69, which plot the values of the fitted A and B parameters as a function of cluster size for impact point K, the results for clusters with six or more cells begin to suffer problems due to the relatively large amount of noise in the low energy runs. (Five cells are usually enough to contain the entire shower at electron

[5] No cause was determined for this abnormality.

[6] A single electron peak is present in the uncalibrated data, which strongly indicates that the two peak structure is a direct result of the calibration process. The calibration is designed to account for the subtle differences in timing and geometry of the equipment.

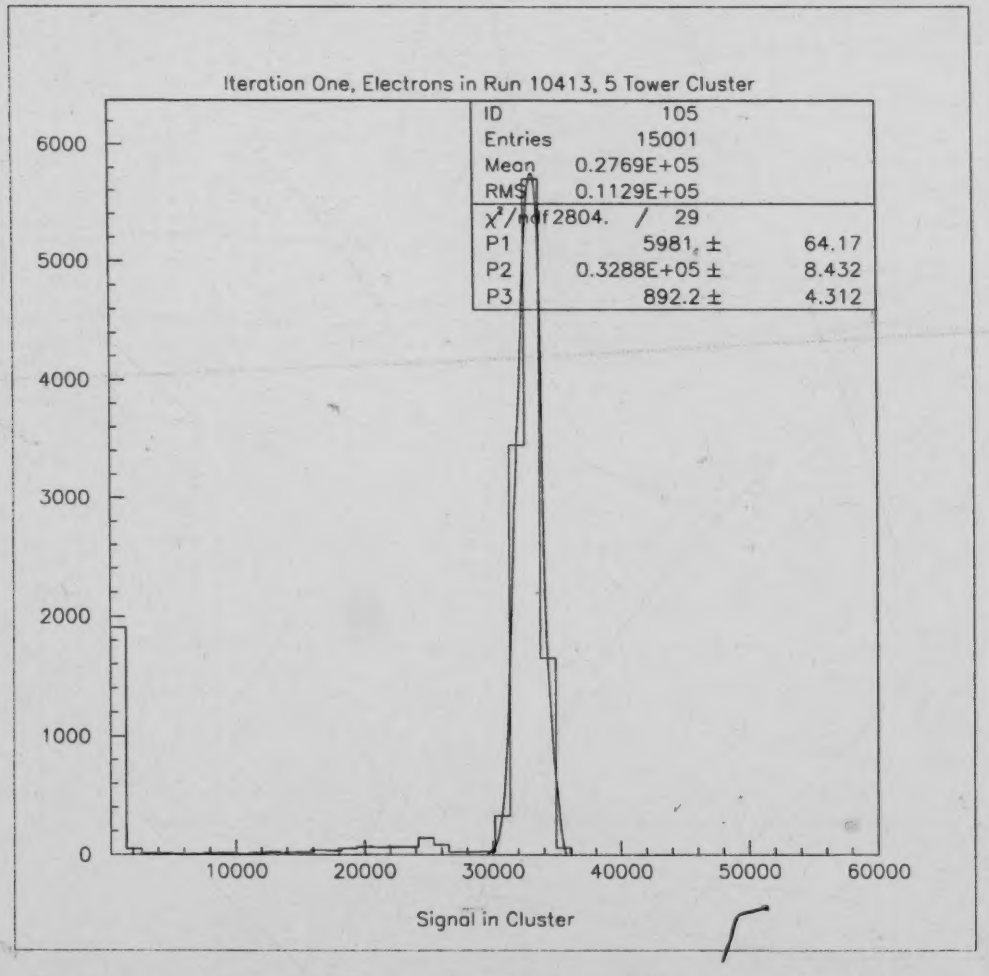

Figure 7.2: In the first iteration of the fitting routine, the signal distribution is not sufficiently detailed for a complete analysis (due to the large horizontal range), but the peak in the central region may be Gaussian in shape.

beam momenta of 10.0 GeV/c.) Clusters larger than six cells have high uncertainty in their fitted parameters, as the problems at the lower energies (in which most of the energy is deposited in one or two cells, and other cells contain mostly noise) become more significant. These low energy problems can be seen in figure 7.8 on page 67.

The five cell clusters selected by the software include, for all impact points but point I, one cell from the first layer, three cells from the second layer, and one cell (the fifth cell) from the third layer. Point I includes two cells from the first layer (the two that define the boundary point I lies upon) as well as three from the second

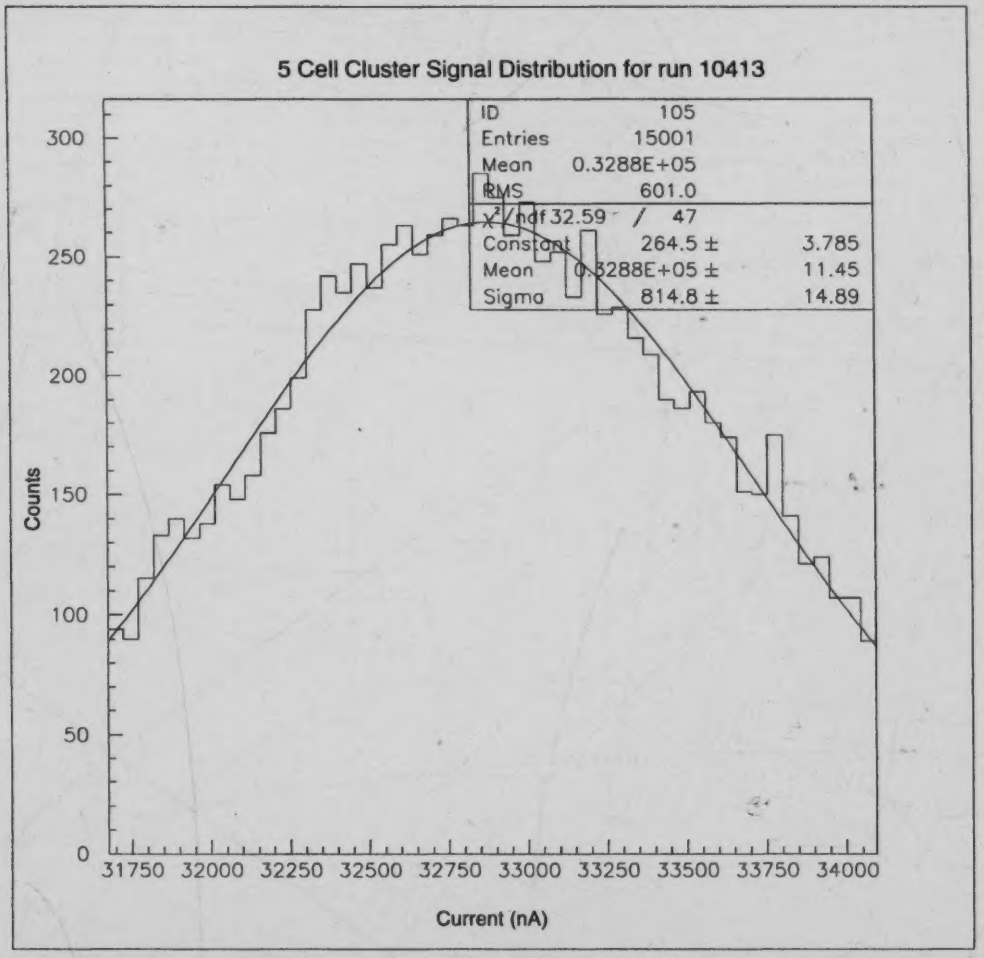

Figure 7.3: A sample Gaussian fit. This is a Gaussian fit to the data collected with electrons of momentum 100.0 GeV/c impacting at point G. Gaussians like these were examined for abnormalities before being committed to the final data set.

layer. The front face of the cells most of these impact points lie upon[7] usually measure 15 cm × 15 cm, so the inclusion of a single cell only is perfectly consistent with the predicted (see chapter 2) Molière radius of 1.15 cm. The predicted depth of the showers (see chapter 2) was up to 12.36 cm. The first layer of the HEC contains 21.25 cm thickness of copper, which would seem to indicate that we would not require the use of cells in more than the first layer of the detector. However, the 12.36 cm limit is a statistical average. In order to ensure collection of over 99% of a shower's energy, one must use more cells than this number would naively suggest.

[7]Point I is the exception again, as it does not lie on a single cell.

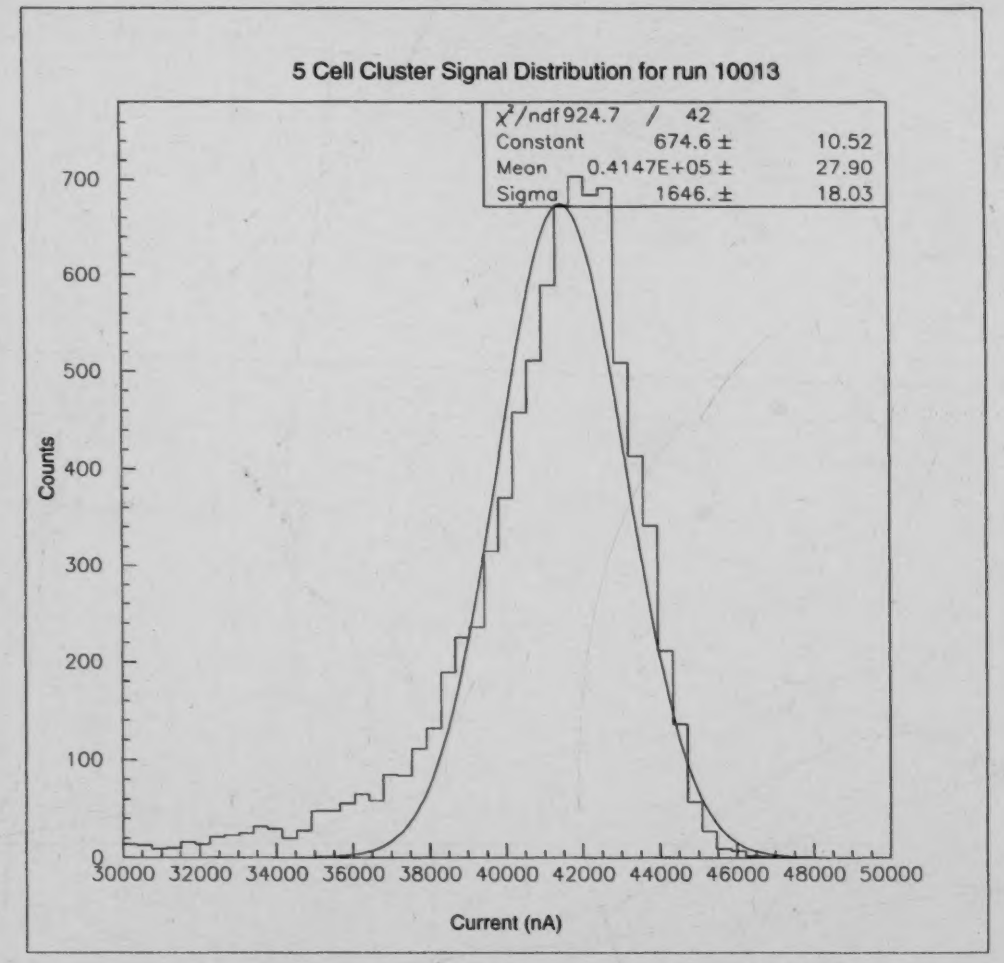

Figure 7.4: An example of a run with a non-Gaussian structure as a result of a trip in the high voltage system. This run is for a beam momentum of 147.8 GeV/c at impact point E.

Reference [1] includes (as its Figure 15) a Monte Carlo simulation depicting the portion of an electromagnetic shower's energy that would be collected by a given number of cells. It indicates that 4 cells are required for 99% containment of the shower. This figure is reproduced here as figure 7.11 on page 70.

7.4 Measuring the Intrinsic Energy Resolution

The results from the fitted Gaussians with standard deviation σ and mean E' for every run in table 7.1 on the following page, were then plotted and fitted to the

	Impact Point					
Energy (GeV)	E	G	I	J	K	N
10.0	10551	10561	10554	10550	10547	10553
20.0	10605	10599	10603	10582	10579	10583
30.0	-	-	10629	10544	-	-
40.0	-	-	10368	-	-	-
50.0	10536	10526	10533	10537	10540	10534
60.0	10393	-	10390	10394	10397	10391
80.0	10402	10412	10405	10401	-	10404
100.0	10428	10413	10420	10429	10432	10421
119.1	-	-	9983	-	-	-
148.0	-	-	9978	-	10025	10049

Table 7.1: The run numbers corresponding to the data used at each impact point and beam energy. Runs that were eliminated due to hardware troubles, and runs for which data were unavailable, are marked with a '-'. There is more than one occasion in which a run is included in the table because some data was used from it, but it wasn't possible to fit a Gaussian function to the data with certain cluster sizes with a reasonable χ^2 value. (The cutoff for χ^2 used was 2.0.)

resolution function

$$\frac{\sigma}{E'} = \frac{A}{\sqrt{E_0}} \oplus B \tag{7.1}$$

first introduced in Eq. 6.2 on page 49, where A and B are the fitted parameters, and E'_0 is the nominal beam energy.[8]

From section 6.1.2, the A term is the sampling term, which quantifies the effects of the statistical fluctuations of the particle interaction within the detector, while the B term is the linear term, which quantifies leakage and calibration errors. The effects of leakage in the electron data set included should not be significant, as supported by both the theoretical predictions given in chapter 2. None of the impact points are close enough to an edge of the detector for this term to vary greatly from point to point. Small variations may occur as the cells in a cluster are of varying volume. Large variations will most likely be due to calibration issues rather than leakage issues for the electron runs data set. Table 7.2 on the next page contains a complete list of the values for the constants A and B for 5 cell cluster sizes. The weighted average of these values give $A = (21.27 \pm 0.08)\,\%\sqrt{GeV}$ and $B = (0.92 \pm 0.03)\,\%$ for electrons. (See figures 7.12 on page 71 and 7.13 on page 72.) However, given the geometry of the system, one could support the notion that we should not include

[8]Technically, the data are first fit to Eq. 6.1 on page 48. Then the noise term is subtracted in quadrature from the data, which is then fit to the two parameter equation shown above.

Tabulated Results of the
Intrinsic Electron Resolution

Impact Point	A $\%\sqrt{GeV}$	B %	χ^2
E	20.4 ± 0.2	0.91 ± 0.07	0.57
G	21.4 ± 0.4	0.79 ± 0.19	3.03
I	22.3 ± 0.2	0.88 ± 0.05	0.59
J	21.2 ± 0.2	1.03 ± 0.08	0.79
K	20.8 ± 0.1	0.84 ± 0.06	0.49
N	22.2 ± 0.3	1.09 ± 0.09	2.11
Weighted Averages for Listed Points			
E, G, I, J, K, N	21.27 ± 0.08	0.92 ± 0.03	-
G, J, K	21.0 ± 0.1	0.90 ± 0.04	-

Table 7.2: The values of the constants in the sampling and linear terms of the intrinsic resolution for electrons. All data are for five cell clusters. Points G, J, and K are the points along the horizontal line studied in reference [1].
All χ^2 values quoted in this thesis are the values of the reduced χ^2.

the data from all impact points when calculating these averages. Point I falls on a crack in the readout electronics, which makes it more susceptible to leakage (as the energy deposited in this crack will not be sampled.) Similarly, Point N is the most susceptible to leakage, given its position within the detector. For this reason, a second weighted average involving only points along the $y = 0$ line (G, J, and K, three of the four points studied in reference [1]) has also been calculated. The data from these impact points produces the values of $A = (21.0 \pm 0.1)\,\%\sqrt{GeV}$ and $B = (0.90 \pm 0.04)\,\%$.

In both cases, the results for A are slightly less than those found in reference [1] (which found $A = (21.4 \pm 0.2)\,\%\sqrt{GeV}$,) although the results for all six impact points agree with the results published in reference [1] within one standard deviation. The results of the three impact points do not quite agree within error, but they do agree within 1.8 standard deviations, so the differences are not unreasonable. Also, remember that the uncertainties used in this analysis reflect statistical uncertainties only, and that an analysis that also includes systematic uncertainties would likely show better numerical agreement between the two analyses. The theoretical prediction from Monte Carlo simulations (see [1]) is $A = (21.7 \pm 0.1)\,\%\sqrt{GeV}$, which is in agreement with the results published in that paper.

The results for B are not as consistent. Reference [1] found that $B = 0.3 \pm 0.2\%$,

Tabulated Results of the
Electromagnetic Conversion Factor

Impact Point	α GeV/μA
E	3.01
G	3.04
I	3.10
J	3.04
K	3.06
N	3.10

Average for Listed Impact Points

E, G, I, J, K, N	3.06
G, J, K	3.05

Table 7.3: The values of the electromagnetic conversion factor for each of the six impact points. All data are for electron beam types and five cell clusters. Uncertainties are omitted as the statistical uncertainties are small compared to systematic uncertainties.

which differs from the result of this analysis by 2.9 standard deviations. The disagreement is possibly due to calibration error. Fortunately, both analyses agree that the effects of leakage are small for electron testbeams. The theoretical prediction from Monte Carlo simulations (see [1]) is $B = 0.00 \pm 0.20\%$, which agrees with the experimental results published in [1].

7.5 Electromagnetic Conversion Factor α

The electromagnetic conversion factor α (introduced in section 6.2) was also calculated for the different impact points, and these results are tabulated in table 7.3 for 5 cell clusters. The overall conversion factor for all six impact points (which is just a weighted average of the individual conversion factors) is $\alpha = 3.06\,\mathrm{GeV}/\mu\mathrm{A}$, and $\alpha = 3.05\,\mathrm{GeV}/\mu\mathrm{A}$ for points G, J, and K only.

The results published in reference [1] are $\alpha = 2.93 \pm 0.03\,\mathrm{GeV}/\mu\mathrm{A}$. While this does not agree with the results presented here, it is difficult to assess the significance of the difference without the systematic uncertainties. It should be noted that the ratio of measured quantities $\frac{\sigma}{E}$ will have little or no dependance on systematic uncertainties, as they will tend to cancel, while α_{em} depends on the absolute scale of E, so systematic uncertainties could well be an important factor. It should also be noted that the significant differences found in the B term above may be a related

problem to the differences in the value of α_{em}.

7.6 Linearity of Electron Results

The final stage in analyzing the electron results is the examination of the linearity. From section 6.2.1, the linearity is the ratio $\frac{\alpha_{em}}{\alpha_{em,i}}$, where $\alpha_{em,i}$ is the electromagnetic conversion factor for some impact point i, while α_{em} is the weighted average electromagnetic conversion factor over all points. In general, the points on the linearity plot will not agree with each other within error, since the geometry of each impact point is slightly different, so they are merely checked to ensure that the percentage difference is small. A 1% margin is generally used as a "rule of thumb" for such a study. In the case of electrons, all linearity factors fall within 2% of the best fit, as is shown in figure 7.14 on page 73. The results for points G, J, and K are all within 1%.

This may serve to illuminate the discrepancies between the results for B, and α. The data analyzed in reference [1] was for the June testbeam data, which was collected from different equipment of the same design as the August equipment. This means it required its own set of calibration constants. If the determination or software implementation of these constants is slightly off, then the differences would appear in the B term, as well as in the mean of the Gaussian.

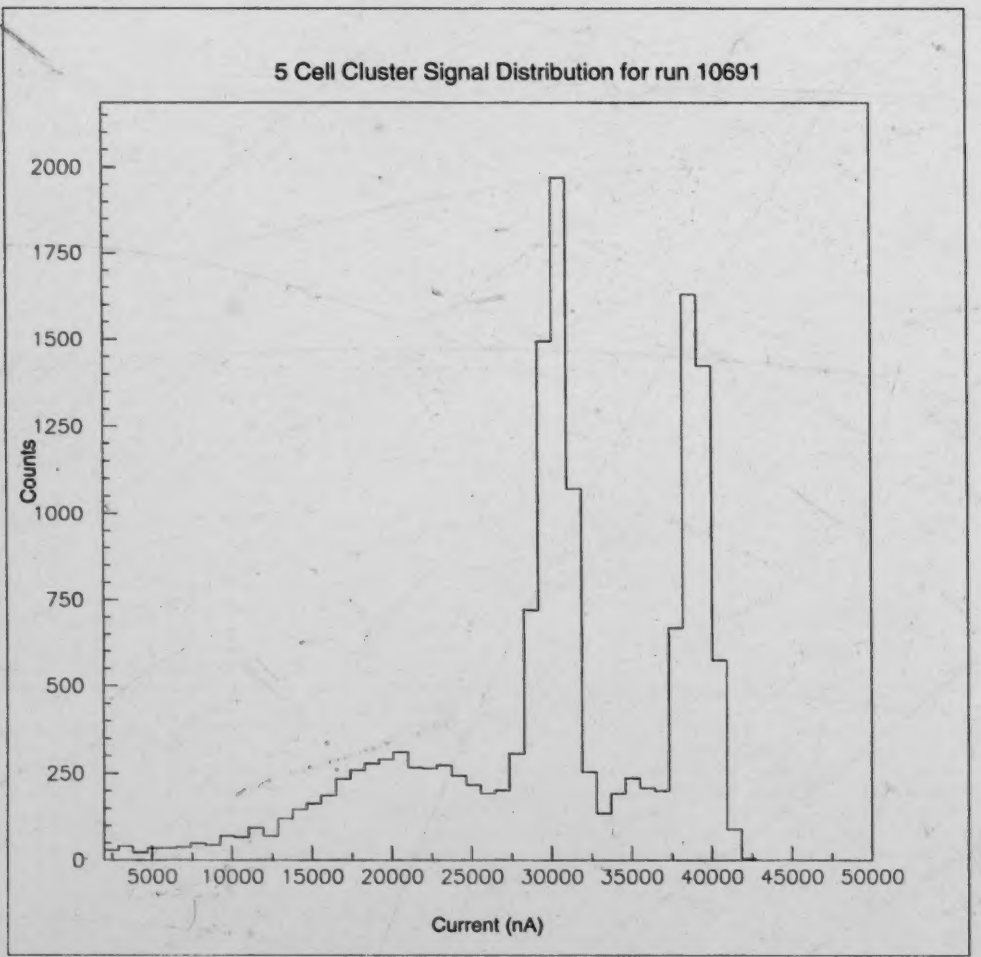

Figure 7.5: An example of a run with a non-Gaussian structure, possibly as a result of a calibration error. The data for all such runs were collected on a single day between two beam accesses by the calibration experts. This run is the sample at impact point I with a beam momentum of 119.1 GeV/c.

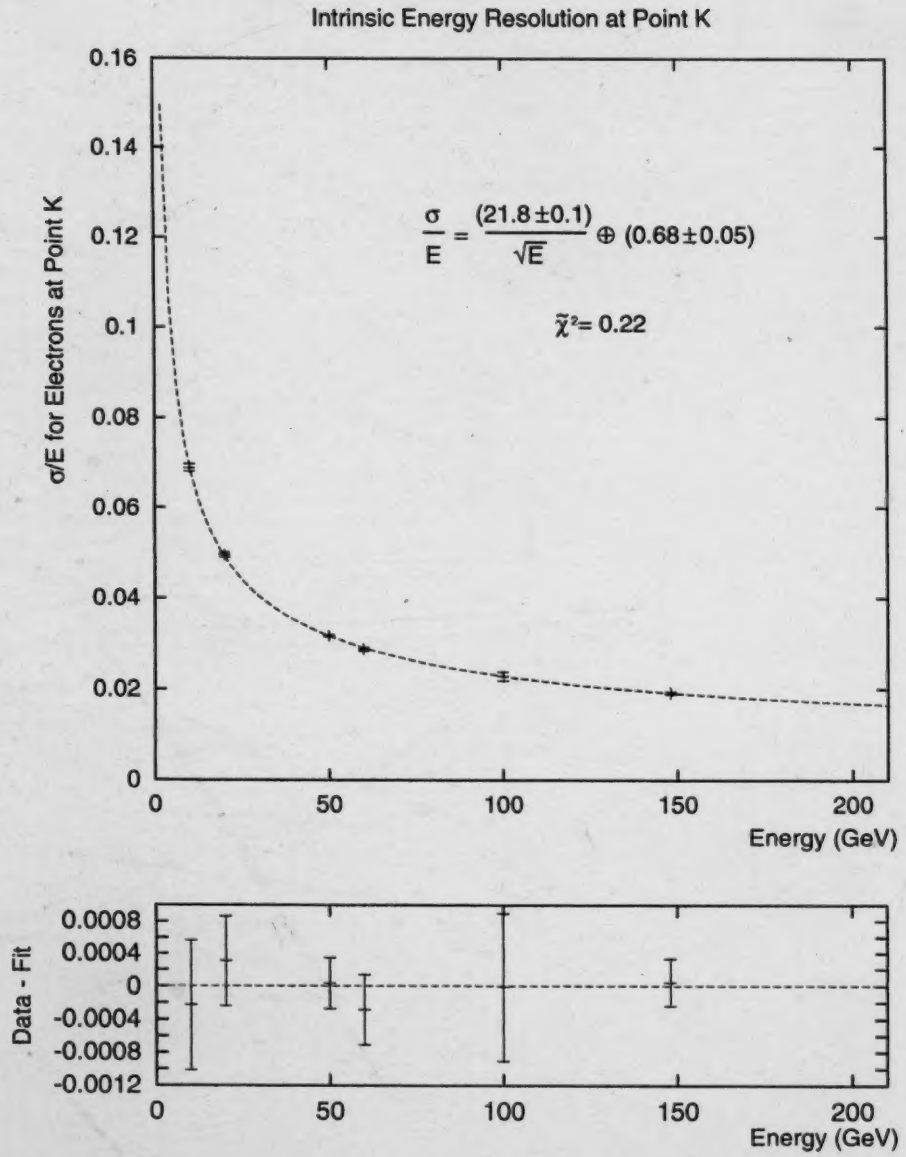

Figure 7.6: The top plot is the intrinsic energy resolution of electrons at point K. The lower plot is the difference between the data and the fitted resolution, provided because the uncertainties are so small on the top plot. This is for a four cell cluster.

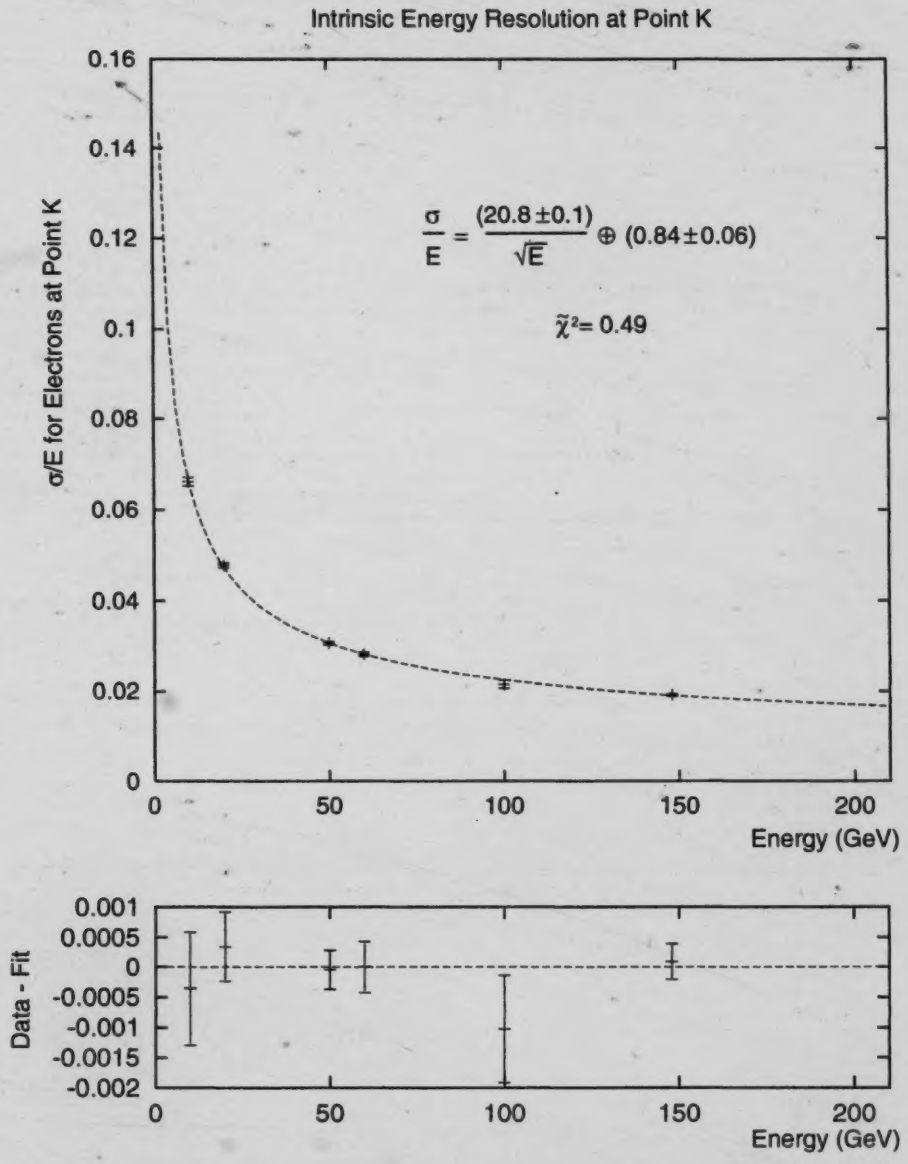

Figure 7.7: The top plot is the intrinsic energy resolution of electrons at point K. The lower plot is the difference between the data and the fitted resolution, provided because the uncertainties are so small on the top plot. This is for a five cell cluster.

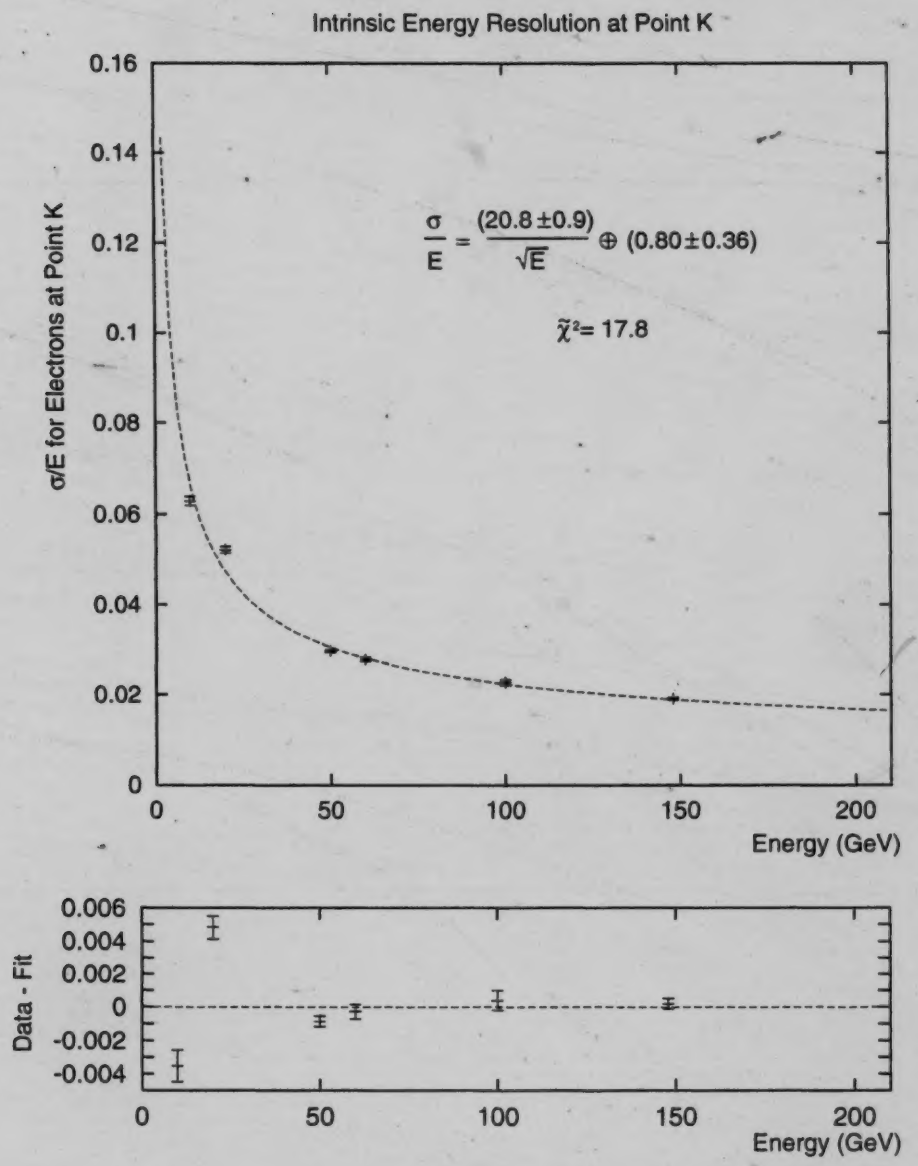

Figure 7.8: The top plot is the intrinsic energy resolution of electrons at point K. The lower plot is the difference between the data and the fitted resolution, provided because the uncertainties are so small on the top plot. This is for a six cell cluster.

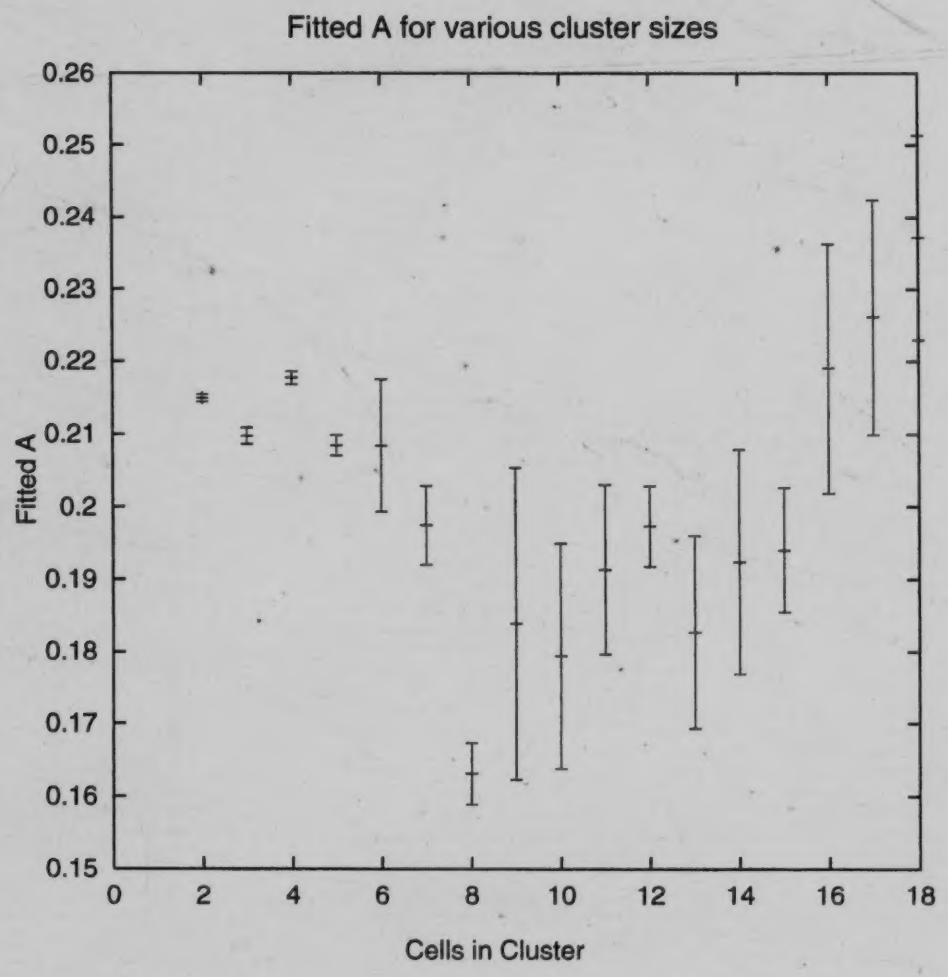

Figure 7.9: A plot of the fitted intrinsic resolution parameter A as a function of cluster size. This parameter is indicative of statistical fluctuations of the shower within the detector.

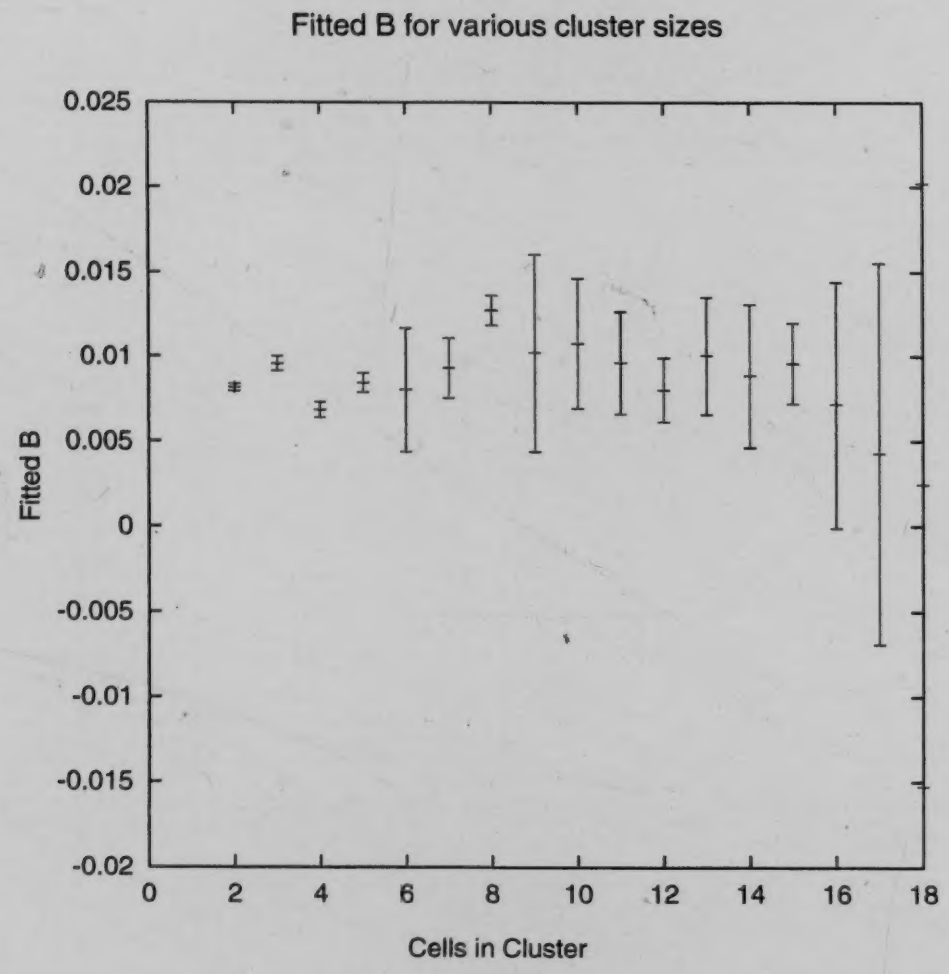

Figure 7.10: A plot of the fitted intrinsic resolution parameter B as a function of cluster size. This parameter is indicative of leakage and calibration errors.

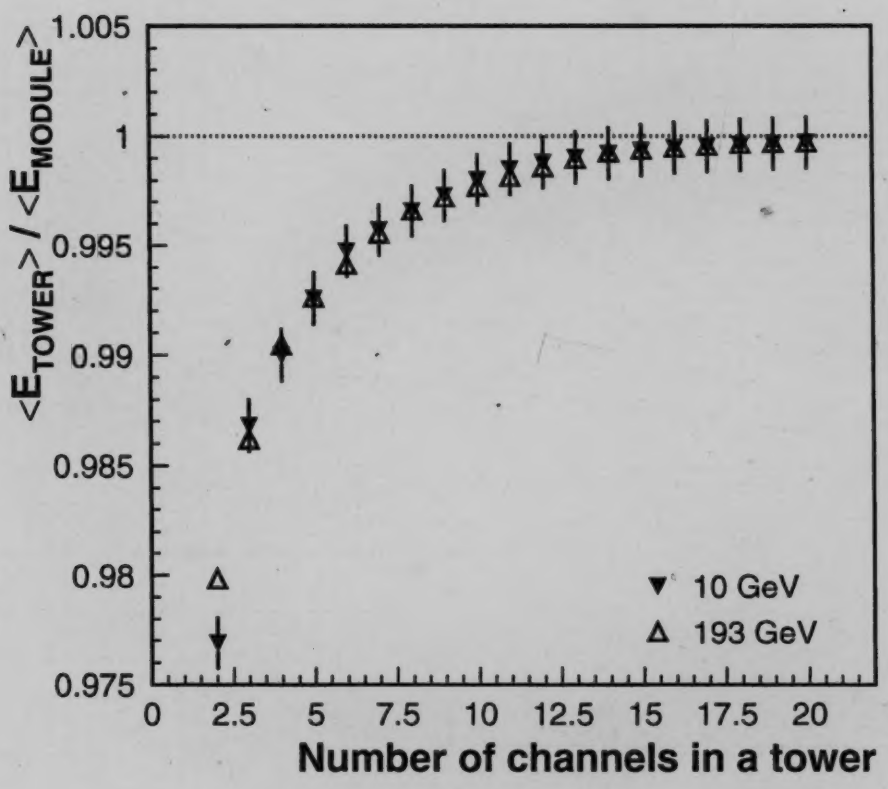

Figure 7.11: Figure 15 from reference [1], depicting the portion of an electromagnetic shower's total energy that would be collected by a given number of cells.

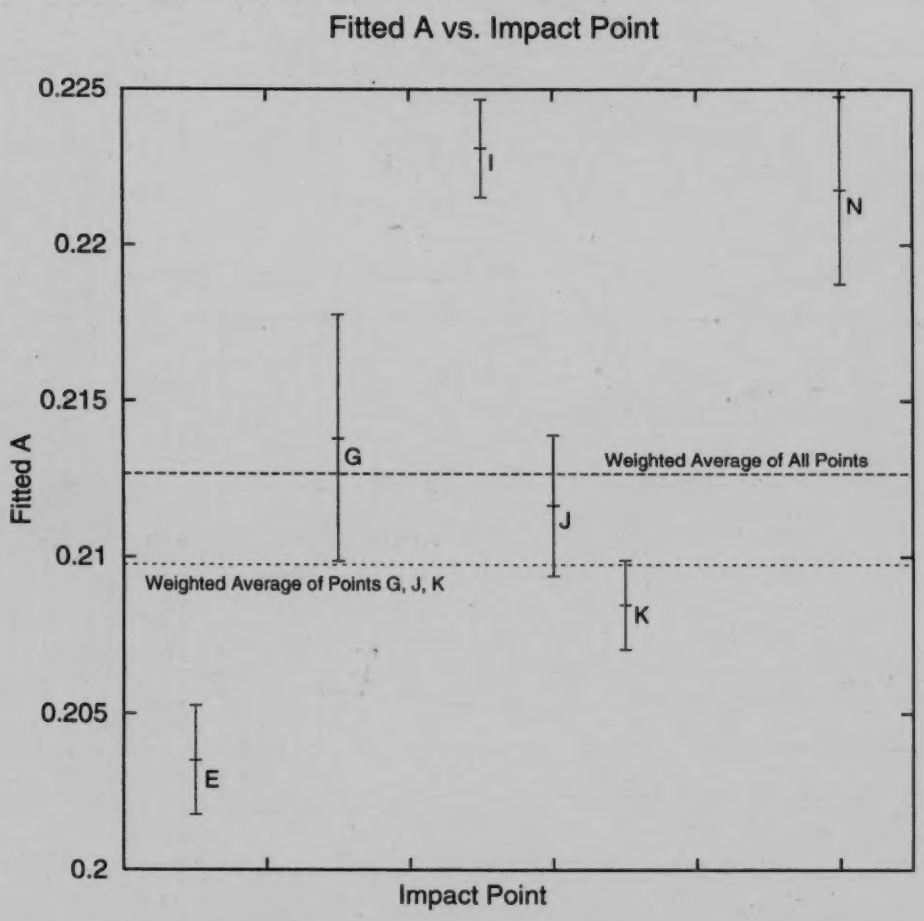

Figure 7.12: A plot depicting the individual values of the intrinsic resolution parameter A for each impact point using a five cell cluster. The horizontal lines mark the weighted averages of the results for the indicated impact points.

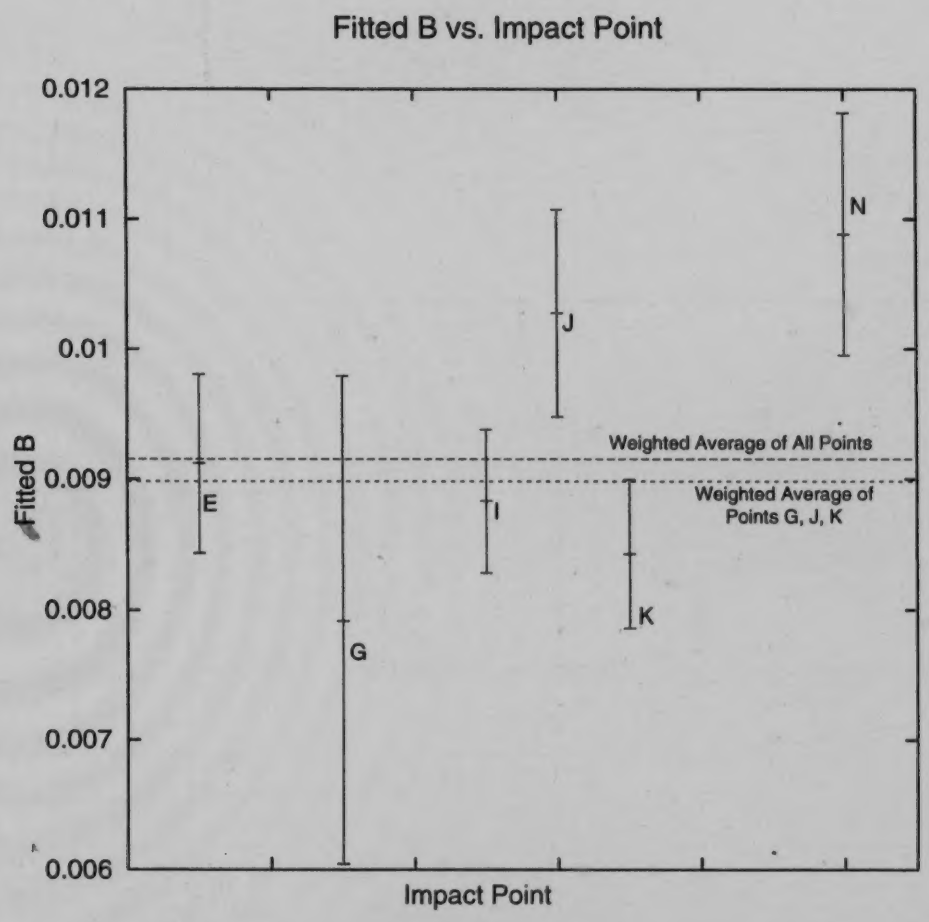

Figure 7.13: A plot depicting the individual values of the intrinsic resolution parameter B for each impact point using a five cell cluster. The horizontal lines mark the weighted averages of the results for the indicated impact points.

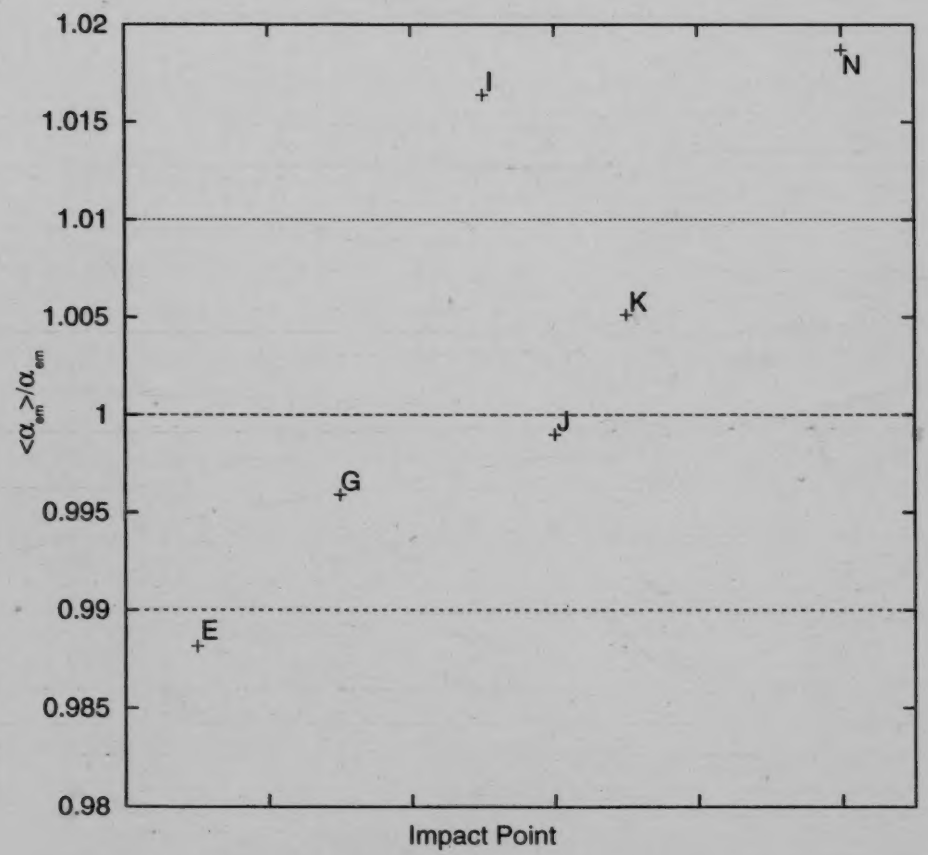

Figure 7.14: The linearity of the electromagnetic conversion factor α_{em} for electron data at all impact points using five cell clusters. The center horizontal line indicates the point at which the electromagnetic conversion factor would equal the average conversion factor (over points G, J, and K.) The other two horizontal lines mark $\pm 1\%$ of this value.

Chapter 8

The Pion Testbeam Results

The primary purpose of the HEC is to sample the energy deposited in showers initiated by hadronic particles. As such, detailed knowledge of the performance of the detector to pion stimulus is very important.

This chapter contains a summary of the expected extent of hadronic showers as predicted by theory, as well as the results of pion data as taken in the August 2000 testbeam period. The quantities examined specifically are the number of cells required to contain a pion shower (which should be larger than that for electrons,) the sampling term A and the linear term B in the intrinsic energy resolution, the hadronic conversion factor, and the fraction $\frac{e}{h}$. These data will be used to make a recommendation for the number of cells that should be included in the clusters to span a pion shower.

8.1 The Expectations

As described in chapter 2, the shape and size of a shower initiated by pions is much wider and deeper than a shower initiated by electrons. The same methodology that was applied to electrons was applied to pions when determining the cluster size, although the tested cluster sizes are considerably larger for pions than for electrons.

Electron showers are thin, and often shallow. Pion showers, on the other hand, tend to spread much wider in the deeper layers, resulting in different shapes and different cluster arrangements. Again, the cells selected for the cluster were manually checked to ensure that they are logical in terms of arrangement and location. The larger spread of the pion showers also requires more cells to contain the shower, so we expect to use more cells in the pion clusters than we did for the electron showers. The widest and deepest showers for pions should be those from the 200 GeV/c momentum

beam particles, with a depth of approximately 120 cm for 90% containment and a width of approximately 58 cm for 99% containment, as calculated in chapter 2. The electron showers were studied with as many as 18 cells per cluster, while the pion showers were studied with as many as 60 cells per cluster.

8.2 Selection of the Data Subset

The data used in this study were chosen in the same manner as the data for the electron studies. Once again, the impact points being studied are E, G, I, J, K, and N. [1] These points provide sample coverage in the horizontal and vertical directions. They are the same points that were used for the electron analysis, so that conditions for the data from both data sets are as similar as possible.

The data quality for the runs was, in general, not as good as that of the electron runs. This was most frequently due to the presence of large amounts of electron contamination in the pion beam, particularly in the later runs and the runs at the 30.0 GeV/c beam momentum. For many of these data runs, the automated fitting routines would fail to find a suitable Gaussian in the data. The fitting routines were confused by the presence of two peaks where they were programmed to look for one Gaussian. Runs with these problems have been fitted to a more restricted range that did not include the contamination. The only serious cases were those of the 30 GeV/c momentum pions, which often resulted in a fit range that did not include the peak of the pion Gaussian. (See figure 8.1 on the following page.) As a result the uncertainties on runs at that momentum are considerably higher than the neighboring runs. A compilation of the data used can be found in table 8.1 on page 78. Note that a run was listed as being used if it was used with any cluster size. For example, if a run produced sensible data when fit to 15 cell clusters, but some problem with the signal from a single cell caused problems for clusters with 16 or more cells, then the run was listed in the table, but the data was only used for cluster sizes up to 15 cells. There were some occasions (such as the 30 GeV/c momentum pion run missing from figure 8.2 on page 77) in which the data from that run could not be fitted to a Gaussian with a χ^2 less than the cut-off value of 2.0. The data from those runs at that particular cluster size were not used for the analysis.

Other runs that failed the fitting procedure had only a single peak, but this

[1] Refer to figure 7.1 on page 55 for the locations of these impact points.

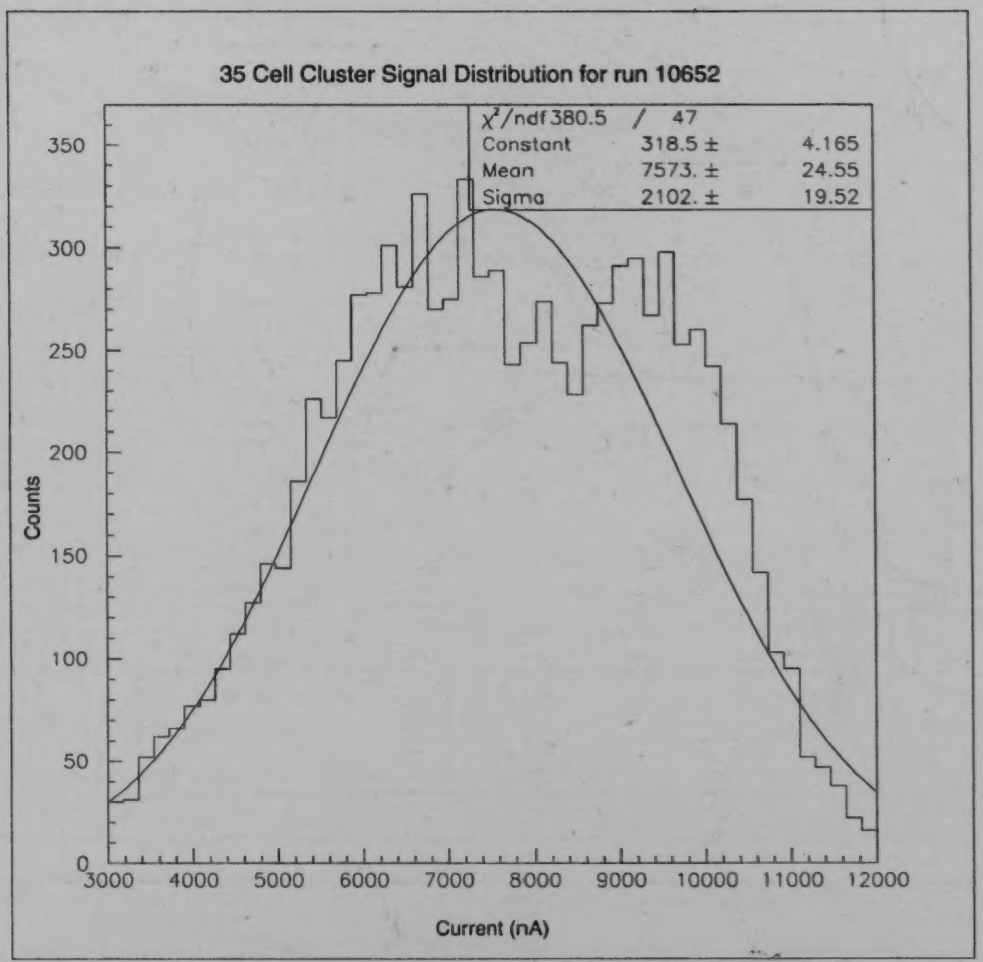

Figure 8.1: A pion run with beam momentum of 30.0 GeV/c. The peak on the left is a result of pions, while the peak on the right is electron contamination. The fitted curve shows the nature of a typical failure to automatically fit a Gaussian to data with this level of contamination.

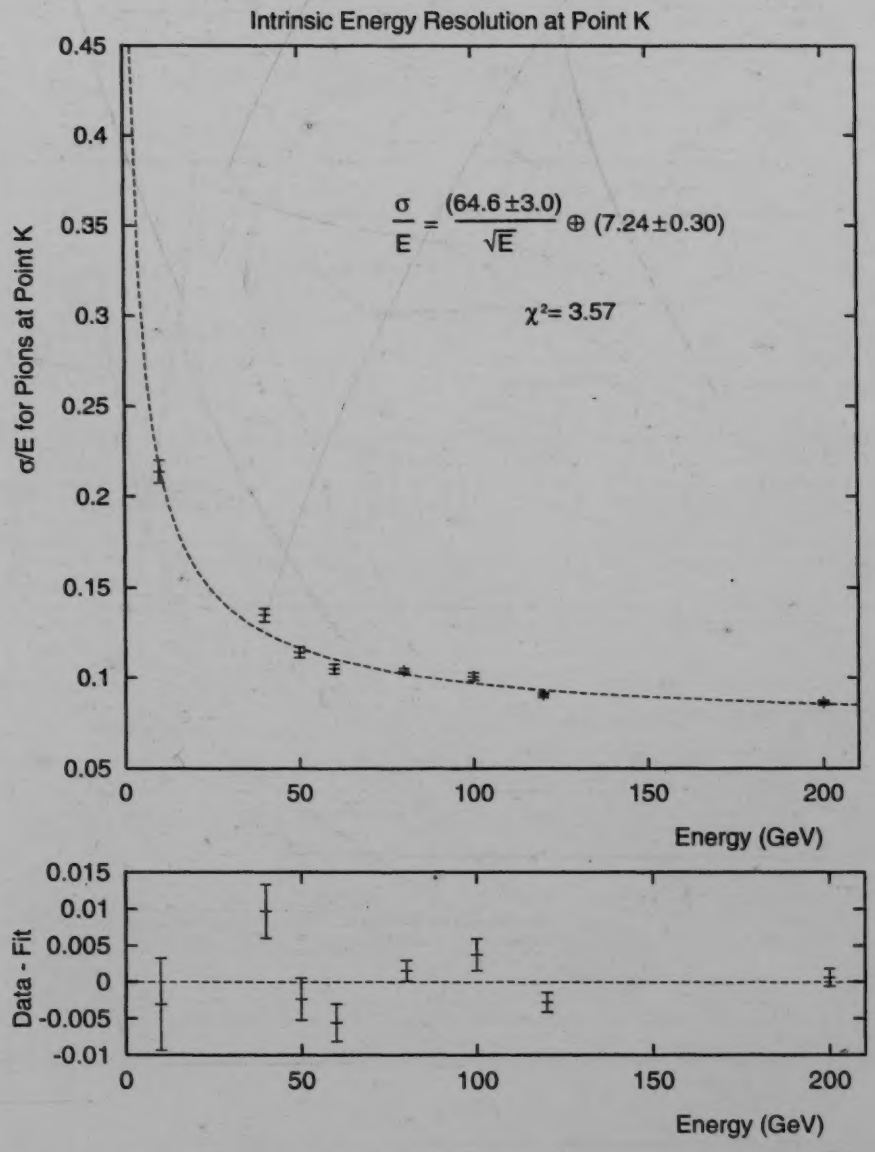

Figure 8.2: The intrinsic energy resolution for pions at impact point K (top plot). There are fifty five cells in this cluster. The bottom plot shows the difference between the data and the fit, to better expose how closely the points follow the fit.

	Impact Point					
Energy (GeV)	E	G	I	J	K	N
10.0	10573	10563	10570	10574	10577	10571
20.0	-	10620	10610	-	-	-
40.0	-	10491	-	-	10504	10498
50.0	10512	10525	10518	10511	10505	-
60.0	10477	10488	-	-	10474	10479
80.0	10467	-	10464	-	10470	10465
100.0	-	10449	-	10437	10434	10440
120.0	10012	-	9982	10035	10024	10050
200.0	10009	10060	9981	10038	10021	-

Table 8.1: The run numbers corresponding to the data used in the pion analysis at each impact point and beam energy. Runs that were eliminated due to hardware troubles, and runs for which data were unavailable, are marked with a '-'. Due to limitations in the strength of the bending magnet, it was not possible to direct pions with momenta of 200.0 GeV/c toward point N. There is more than one occasion in which a run is included in the table because some data was used from it, but it wasn't possible to fit a Gaussian function to the data with certain cluster sizes with a reasonable χ^2 value. (The cutoff for χ^2 used was 2.0.)

peak was not Gaussian in shape. This was almost always the case in a run that corresponded to a trip in the high voltage system. As a result, some cells with real data were inoperative, while others demonstrated unusually large noise. Most of these runs were not included in the final results.

Only one run had a non-Gaussian shape that did not correspond to a trip in the high voltage system of the detector. This run (number 10052) was the 180 GeV/c momentum run for pions at point N. This run had an asymmetric distribution that one finds when the number of cells included in the cluster does not contain a sufficiently large portion of the shower. Since there was no abnormally long low-energy tail, which would indicate that the energy from the run was deposited in a cell not included in the cluster, it is assumed that this missing energy has completely leaked out of the detector. Given the location of point N, (at the bottom edge of the detector) it is not unreasonable to assume that the shower is not well contained within the HEC at this energy.

8.3 Comparison of Pion and Electron Analysis Methods

Now that the analysis of the electron data is complete, it is appropriate to describe which analysis techniques are the same for both electron and pion particle types,

and which are different.

8.3.1 Similarities

The methodology employed in the study of pions is the same as the methodology used for the electron studies. The raw data is still run through the calibration procedures to translate the signal deposited in the HEC modules into a current. The results of that calibration are then fitted to Gaussian forms, and the results of those fits are used in the determination of the energy resolution of the detector, the intrinsic energy resolution of the detector, and the hadronic conversion factor α.

8.3.2 Differences

The primary difference in the analyses of electrons and pions is the anticipated shape and size of a cluster. While the electron clusters studied ranged in size from 1 to 18 cells, the pion clusters studied ranged in size from 3 to 60 cells. This choice was made to reflect the different shower sizes predicted (see chapter 2) by theory.

To make this discussion more tangible, compare figure 7.3 on page 58 to figure 8.3 on the following page. Both show Gaussian distributions for beam particles incident on point G with a beam momentum of 100.0 GeV/c. Figure 7.3 is for an incident electron beam, however, while figure 8.3 is for a pion beam. Notice that the mean of the pion distribution is (as predicted qualitatively in chapter 2) only (approximately) 75% of the mean for the electron distribution, and that the width of the pion distribution is almost 450% of the width of the electron distribution. These differences are as predicted due to the differing natures of the showers, as described more completely in chapter 2.

A further difference is that the study of the linearity of the electron results is inappropriate for the pion studies, as the pion results are not expected to be linear. As discussed in chapter 2, pions experience both hadronic and electromagnetic interactions. The degree to which each interaction is experienced depends on the momentum of the pion as it enters the detector, which means that pions at different energies will have different conversion factors. The pion results should, however, be consistent with a known energy-dependent function that can be used to measure the parameter $\frac{e}{h}$.

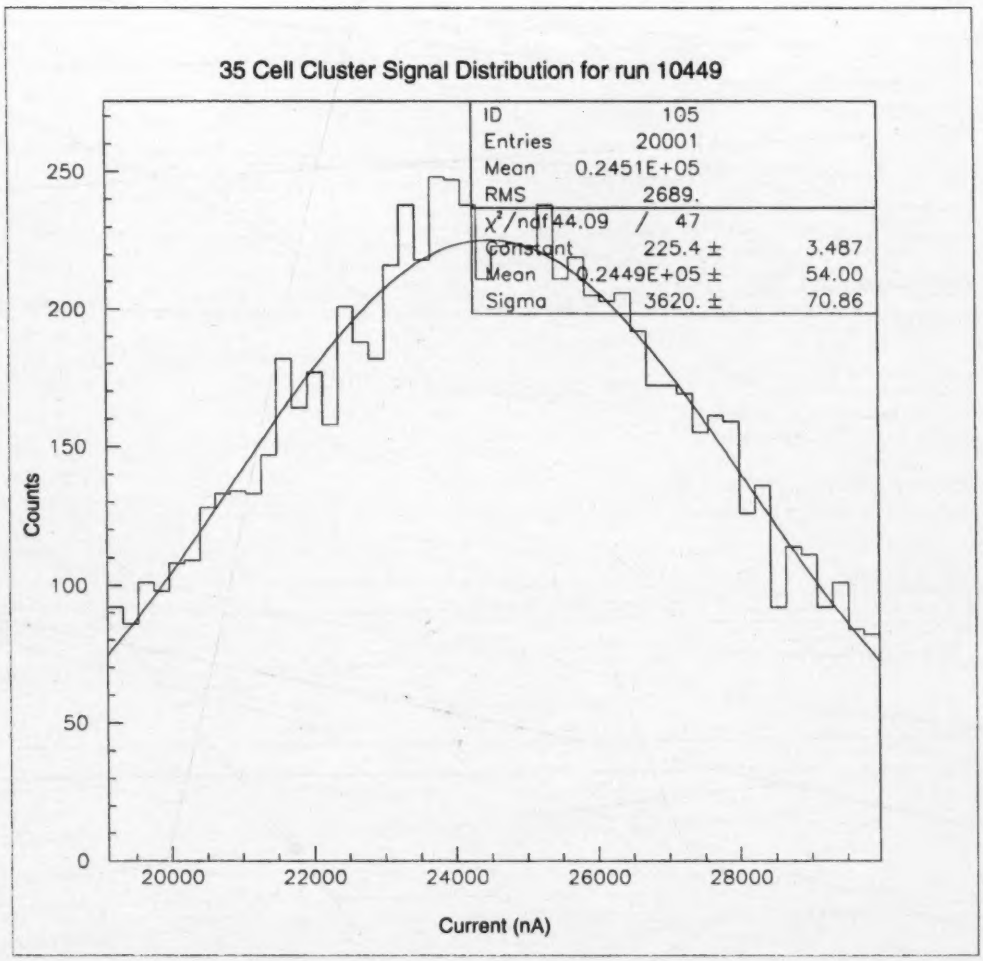

Figure 8.3: A sample Gaussian fit. This is a Gaussian fit to the data collected with pions of momentum 100.0 GeV/c impacting at point G. Gaussians like these were examined for abnormalities before being committed to the final data set.

8.4 Intrinsic Energy Resolution and Determination of Cluster Size

To determine cluster size, energy distributions were fit to Gaussians for 3 to 60 cell clusters. The resulting mean and width were fit to the energy resolution as a function of energy. At this point, the contributions of the noise term were subtracted from the data, and the intrinsic energy resolution was fitted to the result.

The pion data is fit to the same intrinsic energy resolution equation as the electrons,

$$\frac{\sigma}{E'} = \frac{A}{\sqrt{E_0}} \oplus B \tag{8.1}$$

first introduced in Eq. 6.2 on page 49. Again, $\frac{A}{\sqrt{E_0}}$ is the sampling term, which quantifies the statistical fluctuations in the number of particles in the shower, B is the linear term, which measures quantities like leakage and calibration errors, σ is the width of the signal Gaussians that are fit for each run, E' is the mean of those Gaussians, and E'_0 is the beam energy (in GeV). A sample plot of the intrinsic resolution fit for pions at impact point K for a 55 cell cluster can be seen in figure 8.2 on page 77.

Several of these intrinsic resolution plots were created, and the evolution of the parameters was plotted as a function of cluster size. As can be seen in figure 8.4 on page 84, the sampling term for the pion data gradually decreases with increasing cluster size, eventually leveling out around the 50 cell cluster. In contrast, the linear term rapidly drops until a 20 cell cluster is reached, at which point it is flat (see figure 8.5 on page 85.) It has been shown in simulation (see figure 17 of reference [1], reproduced here as figure 8.6 on page 86) that a cluster composed of approximately 50-60 cells should be sufficient to contain over 98% of the shower for 200 GeV pions. Using larger clusters would contribute to the noise term, and provide little gain in terms of the experimental resolution of the detector. Therefore, a cluster composed of approximately 55 cells is recommended. (The specific values of the sampling and linear terms for pions at all impact points can be found in table 8.2 on page 83 and figures 8.7 on page 87 and 8.8 on page 88.)

The first thing one should notice when examining table 8.2 on page 83 is that the results are often not consistent across impact points. In some cases, this is to be expected. Point I is on a division in the electronics, which implies that it has a large dead area that runs through the core if any hadronic (or electromagnetic) showers

targeted there. This effect should only be significant when the parent particle's incident trajectory is oriented along the center of this gap, and becomes more significant as the incident particle's energy decreases and a larger fraction of the total energy is lost, as we can see in the data for $E < 50\,\text{GeV}$ in figure 8.9 on page 89. We can also see the effects on the χ^2 in table 8.2 on the next page. Point N lies nearest to the bottom of the detector, and is more susceptible to leakage than the other points. It also lacks high energy data points, which makes the B term in the fit more difficult to extract with accuracy.[2] The third noticable out of place point is impact point K, with its low value of A and its high values of B and χ^2. The high value of χ^2 for point K strongly implies that the function fitting for point K may have failed. Figures 8.7 on page 87 and 8.8 on page 88 also indicate that there is an issue with the fit in the neighbourhood of the 55 cell cluster. As such, the A factor in the sampling term is likely closer to $70\,\%\sqrt{\text{GeV}}$. One contributing factor would be that these uncertainties are purely statistical, and do not reflect systematic effects. They also do not reflect the fact that the parameter C is treated as an exact value during subtraction, such that the uncertainties on the individual data points (and, by extension, the curves fitted to them) are underestimated. It is clear, however, that there is a significant problem in the analysis of this impact point. One possible problem may be that the assumption that the term C is constant at an impact point over all runs. It may, in fact, vary over time, in which case it must be determined on a run-by-run basis, and the runs would then be corrected individually rather than globally before the intrinsic energy resolution is determined. (In fact, it is this method of determining C that is used in more recent analyses of more recent data.) The weighted averages of A and B at points G, J, and K will still be used for comparison with previous results, but strong agreement cannot be expected until the consistency at point K can be improved. It should also be noted that the value of the χ^2 for each impact point has increased after the subtraction of the noise term, which lends support to the idea that this term should be calculated and subtracted on a run-by-run basis.

The value of the sampling term averaged over points G, J, and K (see table 8.2 on the following page)[3] does not agree with that found in reference [1]

[2]The limitation in available energy levels is a result of limitations in the bending magnet strength. High energy incident beams cannot be steered to the impact points that are too far from the $y = 0$ line. This limitation will, of course, not be present in the data collection of ATLAS.

[3]All values used for comparisons to theory or to the results published in reference [1] are the values determined for points G, J, and K, since they are the ones in a comparable physics arrange-

Tabulated Results of the
Pion Intrinsic Energy Resolution

Impact Point	A $\%\sqrt{GeV}$	B %	χ^2
E	87 ± 3	5.0 ± 0.5	3.37
G	86 ± 2	6.2 ± 0.3	1.93
I	97 ± 5	5.1 ± 0.9	14.38
J	87 ± 2	4.5 ± 0.3	1.48
K	65 ± 3	7.2 ± 0.3	3.57
N	110 ± 3	5.1 ± 1.7	1.74
Weighted Average for Listed Points			
E, G, I, J, K, N	88.0 ± 1.2	5.88 ± 0.16	-
G, J, K	81.8 ± 1.4	6.11 ± 0.18	-

Table 8.2: The fitted parameters of the intrinsic energy resolution for 55 cell clusters with a pion beam. This can be seen graphically in figures 8.7 on page 87 and 8.8 on page 88.

($70.5 \pm 1.5\%\sqrt{\text{GeV}}$), differing by approximately 5.5 standard deviations. The theoretical prediction from Monte Carlo simulations (see [1]) is $A = 65.6 \pm 0.7\%\sqrt{\text{GeV}}$. Similarly, the linear term here disagrees with that of reference [1] ($5.7 \pm 0.2\%$,) but only by approximately 1.5 standard deviations. The theoretical prediction from Monte Carlo simulations (see [1]) is $B = 4.9 \pm 0.1\%$. This discrepancy strongly implies that the C term should not be considered constant across all points, and that meaningful analysis may require the non-intrinsic energy resolution.

In the interests of determining how much of an impact the non-linearity of the C term may cause, the energy resolution was studied without the noise term subtracted. When examining table 8.3 on page 90, which contains the result of the energy resolution fits before the noise term $\frac{C}{E_0}$ has been subtracted, one might notice that the values of A and B are not completely consistent across impact points. Points K and N do not agree with the others within one standard deviation for parameter A. Only Point K is inconsistent with all other points to one standard deviation on parameter B. There is little agreement on parameter C, but that parameter is the one that is most sensitive to the individual electronics of each impact point, so this is not necessarily a problem. However, this may also be an indication that the assumption made that the value of C is independent of the individual run may not be a valid assumption.

ment.

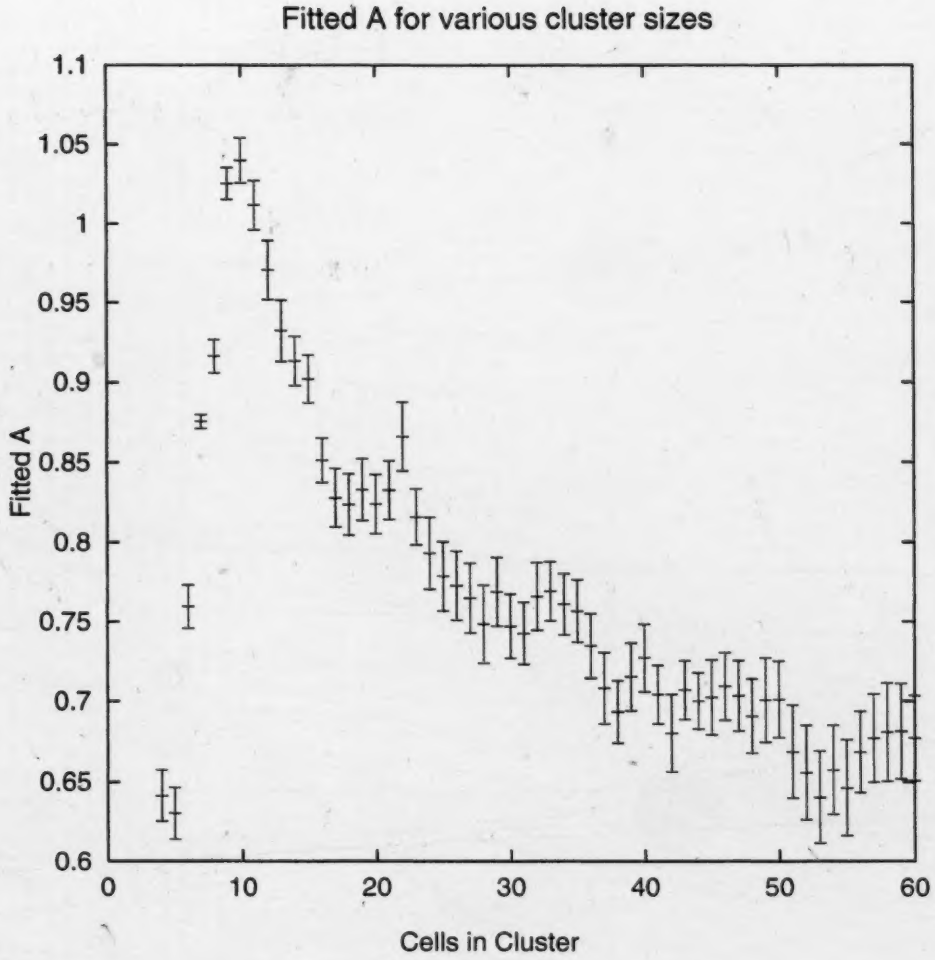

Figure 8.4: A plot of the fitted intrinsic resolution parameter A as a function of the number of cells per cluster. Note the plateau in cluster sizes above approximately 50 cells per cluster. This data is for impact point K.

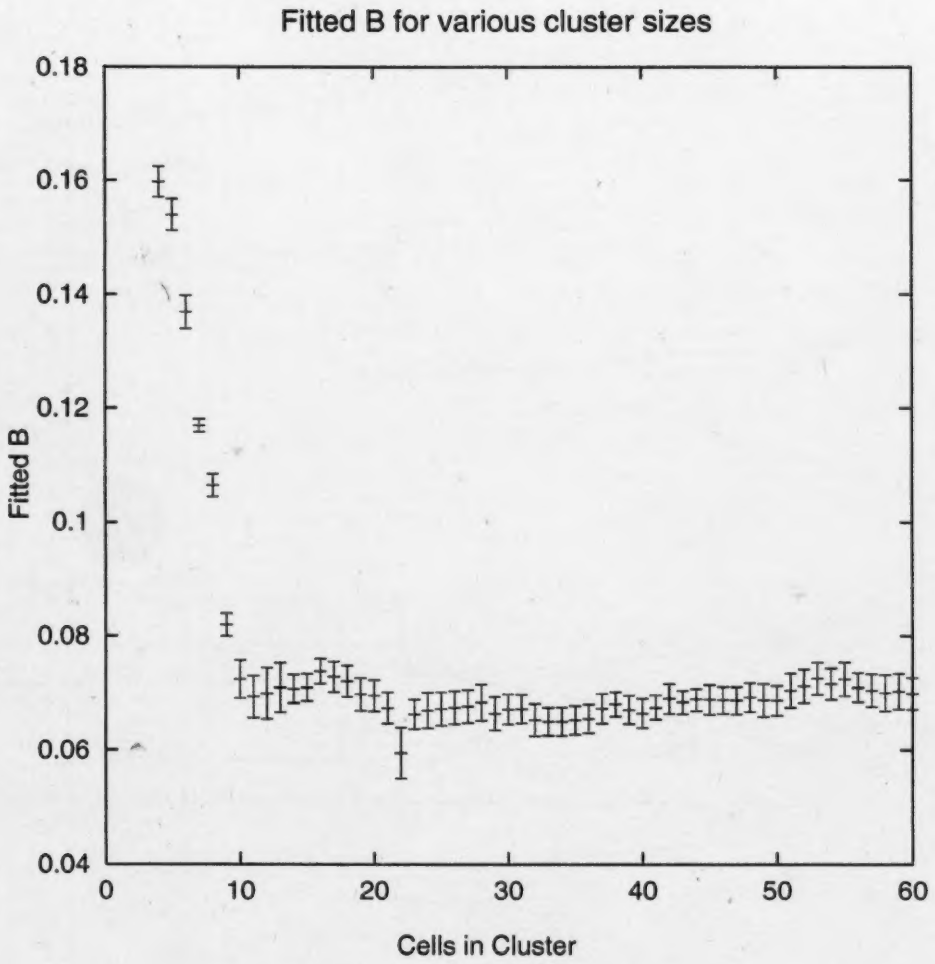

Figure 8.5: A plot of the fitted intrinsic resolution parameter B as a function of the number of cells per cluster. Note the plateau in cluster sizes above approximately 20 cells per cluster. This data is for impact point K.

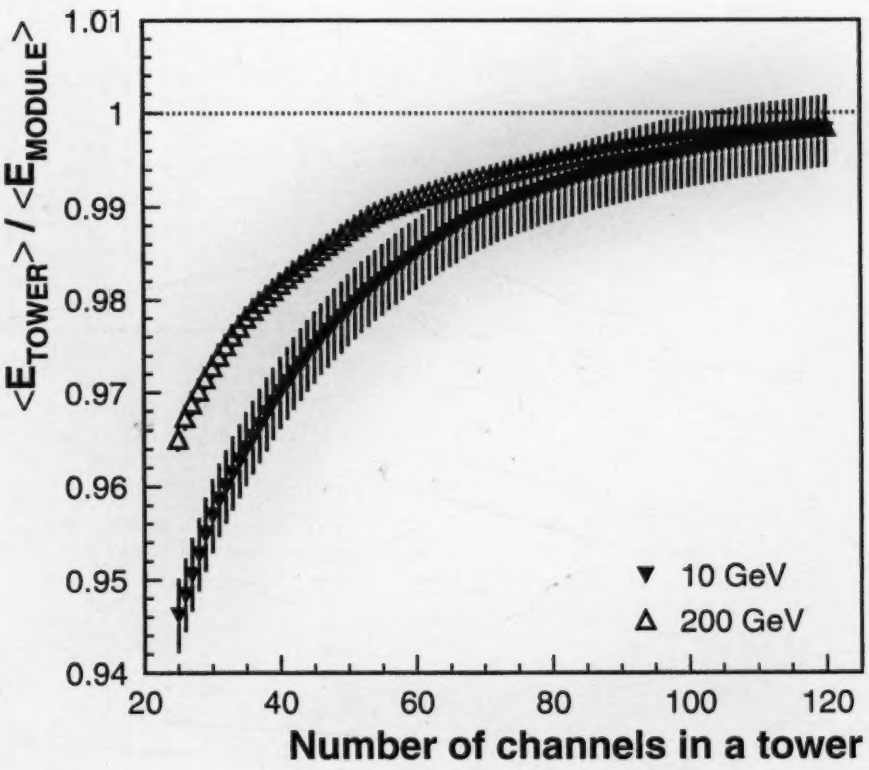

Figure 8.6: The fraction of the shower energy predicted to be contained in a cluster as a function of the number of cells in the cluster. This figure was originally published in reference [1].

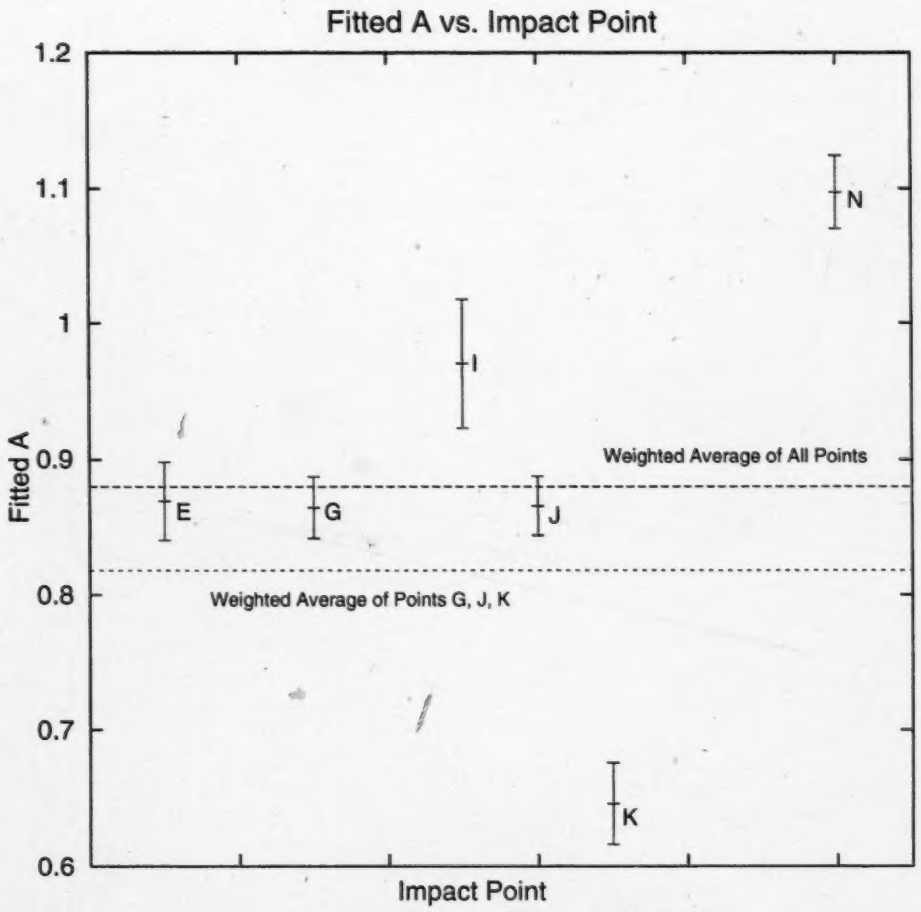

Figure 8.7: The sampling terms for 55 cell clusters at the different impact points. The horizontal lines are the weighted averages of the indicated points.

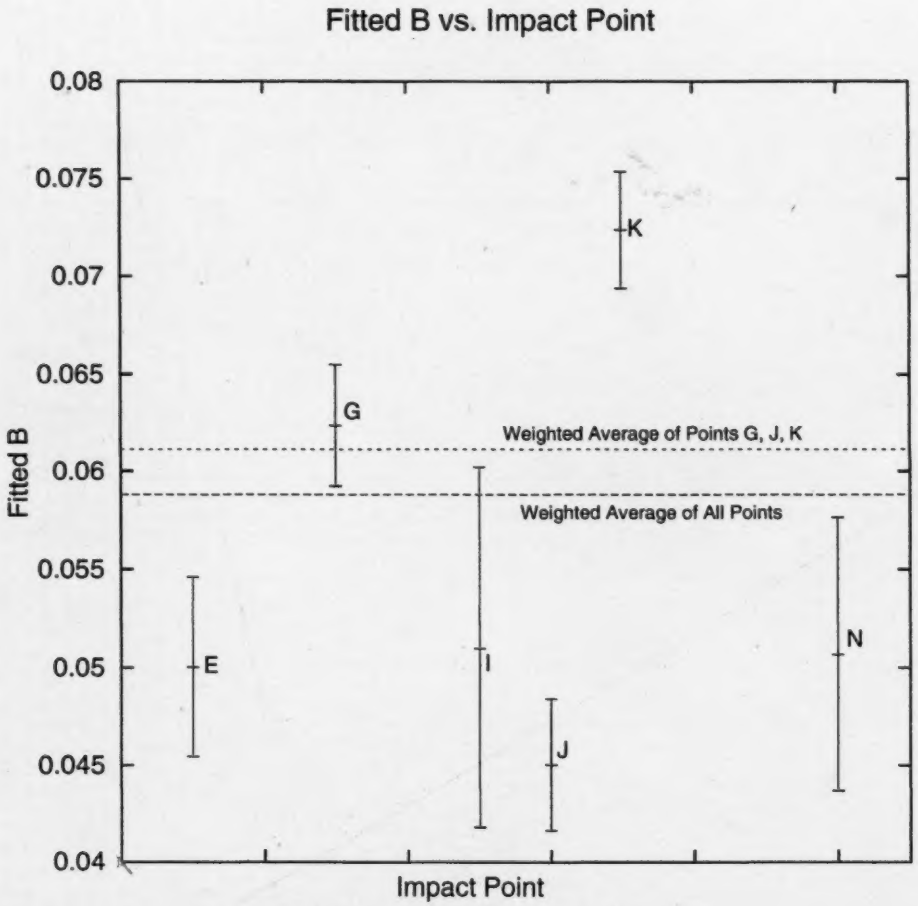

Figure 8.8: The linear terms for 55 cell clusters at the different impact points. The horizontal lines are the weighted averages of the indicated points.

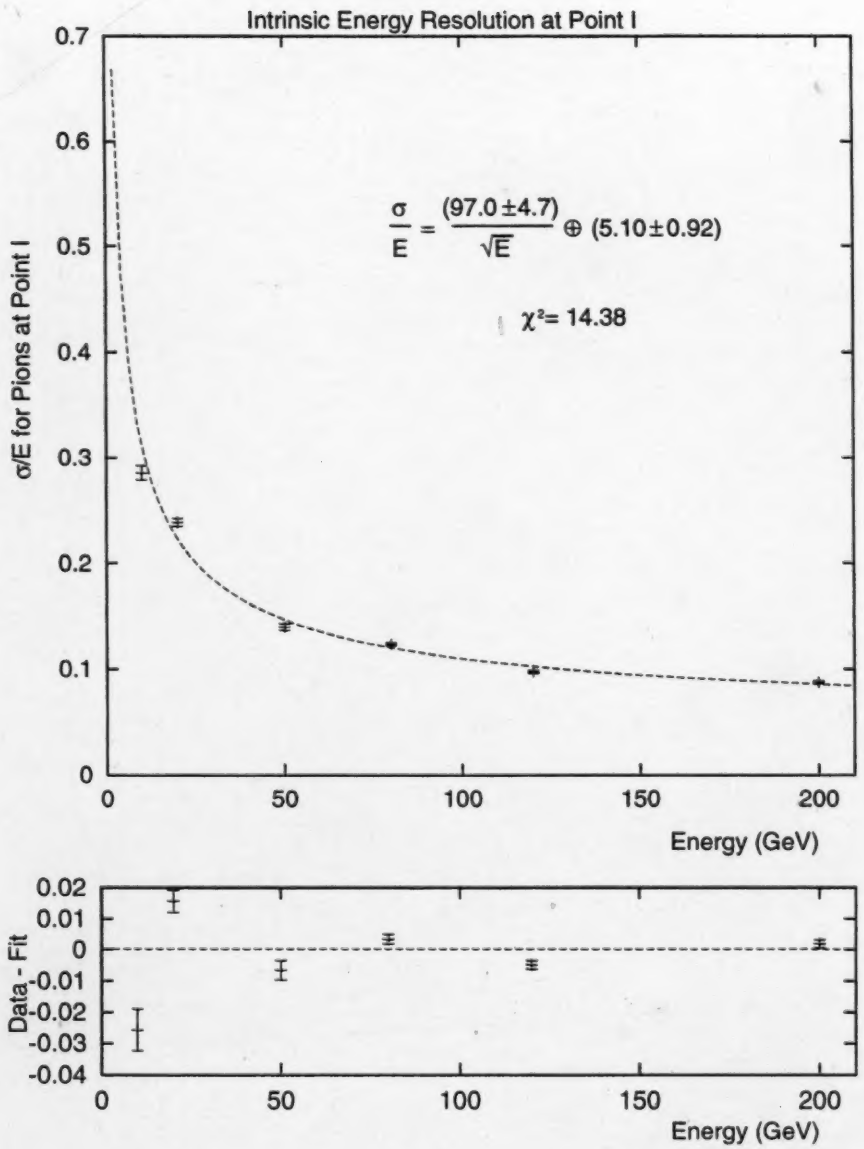

Figure 8.9: The intrinsic energy resolution for pions at impact point I. There are fifty five cells in each cluster. Point I is the point at the crack in the electronics.

Tabulated Results of the
Pion Energy Resolution

Impact Point	A $\%\sqrt{GeV}$	B %	C GeV	χ^2
E	87 ± 6	5.0 ± 0.6	6.6 ± 0.2	2.72
G	86 ± 5	6.2 ± 0.4	6.0 ± 0.1	1.57
I	97 ± 10	5.1 ± 1.4	5.9 ± 0.3	9.50
J	87 ± 5	4.5 ± 0.6	6.6 ± 0.1	1.49
K	65 ± 6	7.2 ± 0.4	6.4 ± 0.1	2.36
N	110 ± 7	5.1 ± 1.5	6.0 ± 0.2	1.73
Weighted Average for Listed Points				
E, G, I, J, K, N	86.5 ± 2.5	6.05 ± 0.23	6.32 ± 0.05	-
G, J, K	81.0 ± 3.0	6.30 ± 0.26	6.33 ± 0.06	-

Table 8.3: The fitted parameters of the energy resolution for 55 cell clusters with a pion beam.

When comparing with reference [1], we notice better agreement than we had with the intrinsic energy resolution. The fitted parameter A (fitted over points G, J, and K) now only differs from the previous result by 2.8 standard deviations, which is a significant improvement over the previous 5.5. The linear term disagrees by 1.8 standard deviations, only slightly larger than the previous result. The inconstancy of the C term cannot explain all of the inconsistencies, but it is certainly a contributing factor.

The cluster sizes found here are consistent with those predicted in chapter 2. The depth of the shower predicted for 90% containment of the largest showers is 120 cm, and 240 cm for 95% containment; the clusters here span the full 143.75 cm depth of copper in the HEC, containing over 90% of the shower. The width to contain 99% of the lateral spread of the shower was predicted to be 58.5 cm. Since the front face of the cells is approximately 15 cm × 15 cm, the inclusion of up to four cells laterally in all directions from the incident beam target is as expected.

8.5 Hadronic Conversion Factor α and the Fraction $\frac{e}{h}$

The conversion factor α for the pion data is expected to differ from that for electrons, as a result of the energy dependence of the pion shower structure.[4] Like

[4]The use of the word hadronic in "hadronic conversion factor" is not completely accurate here. Pion showers contain both hadronic and electromagnetic interactions, so a purely hadronic conversion factor cannot be measured.

the conversion factor for the electromagnetic interactions, the hadronic conversion factor should be independent of beam energy. Unfortunately, the pion interactions are not completely hadronic interactions. As the energy of the pions increases, the pion conversion factor decreases in a non-linear fashion, as the hadronic interactions become more prevalent. Some portion of the shower will escape through the back of the detector as well, which can have a significant impact on the conversion factor. As such, there will be two versions of all plots in this section; the "uncorrected" versions use the data only, while the "corrected" versions attempt to adjust the results according to the energy leakage losses predicted from Monte Carlo simulations, as seen in figure 8.10 on the following page, originally published as figure 16 of reference [1]. (See figures 8.11 on page 93 and 8.12 on page 94 for these results, as well as those from reference [1] shown in figure 8.13 on page 95. As you can see, the results here give a slightly higher value of $\frac{e}{\pi}$ than the results from reference [1].) However, the ratio of the electromagnetic and pion conversion factors is a function that can be described and parameterized in terms of the ratio of the (single, constant) electromagnetic conversion factor and the hadronic conversion factor, generally described in the fraction $\frac{e}{h}$ first seen in equation 6.7 on page 52:

$$\frac{e}{\pi} = \frac{e/h}{1 - \left(1 - \frac{e}{h}\right) f(E)} \tag{8.2}$$

where

$$f(E) = 0.11 \ln\left(\frac{E}{E_0'}\right) \tag{8.3}$$

E_0' is the parameter $E_0' \approx 1\,\text{GeV}$, and E is the deposited energy (in GeV) measured in that run. The value of E is also corrected to compensate for leakage.[19]

An alternative parameterization has [18]

$$f(E) = 1 - \left(\frac{E}{E_0'}\right)^{-0.15} \tag{8.4}$$

where once again $E_0' \approx 1\,\text{GeV}$.

The conversion factors determined previously for each run were used to convert the energies into units of GeV. Once that was completed, the data were fitted to equation 8.2. This fit was performed with data both before and after correction for leakage, as well as with sets of six impact points and three $y = 0$ impact points. (See table 8.4 on page 96 for the details.) A value of $\frac{e}{h} = 1.649 \pm 0.023$ was found when the function was fitted to all six impact points examined here. The results are visible in figure 8.15 on page 98, and it becomes clear that the value of $\frac{e}{h}$ depends greatly

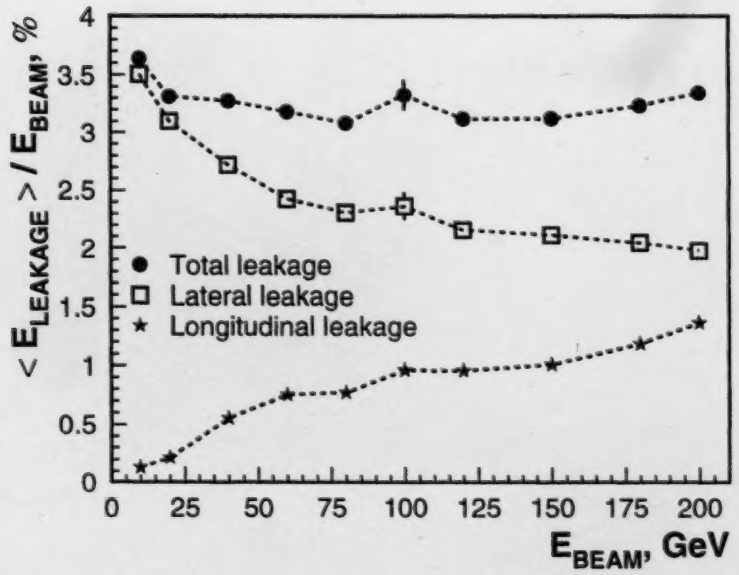

Figure 8.10: The Monte Carlo simulations of energy leakage for pion showers in the HEC for $y = 0$. These numbers are dependent on the cluster size and the impact point. This plot was taken directly from reference [1].

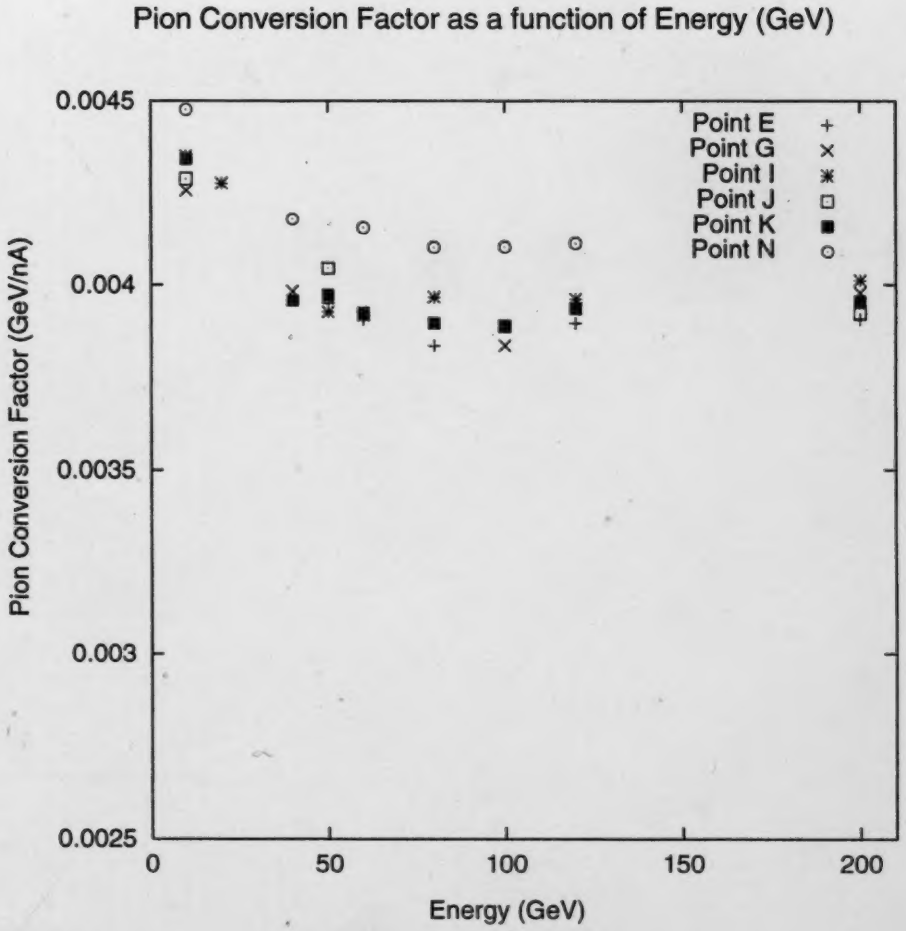

Figure 8.11: The pion conversion factor for all impact points as a function of energy, uncorrected for energy leakage through the back of the HEC. The effects of lateral leakage can be seen most clearly in the set of data from point N.

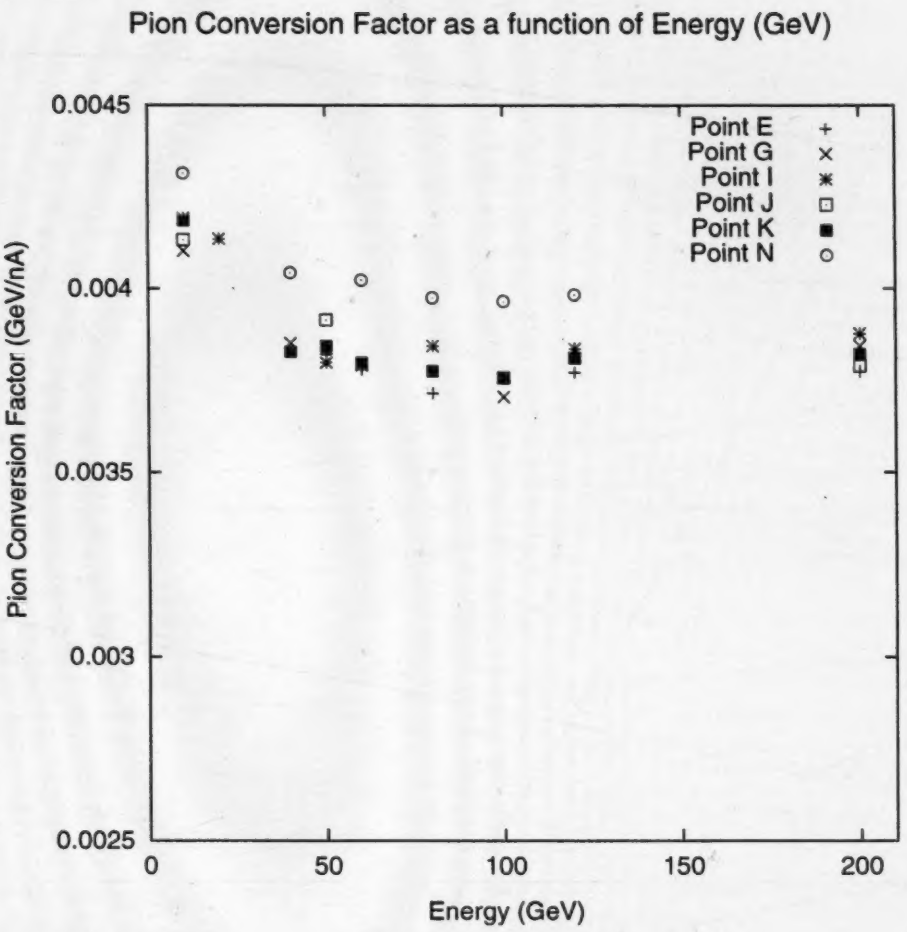

Figure 8.12: The pion conversion factor for all impact points as a function of energy, corrected for energy leakage through the back of the HEC. The effects of lateral leakage can be seen most clearly in the set of data from point N.

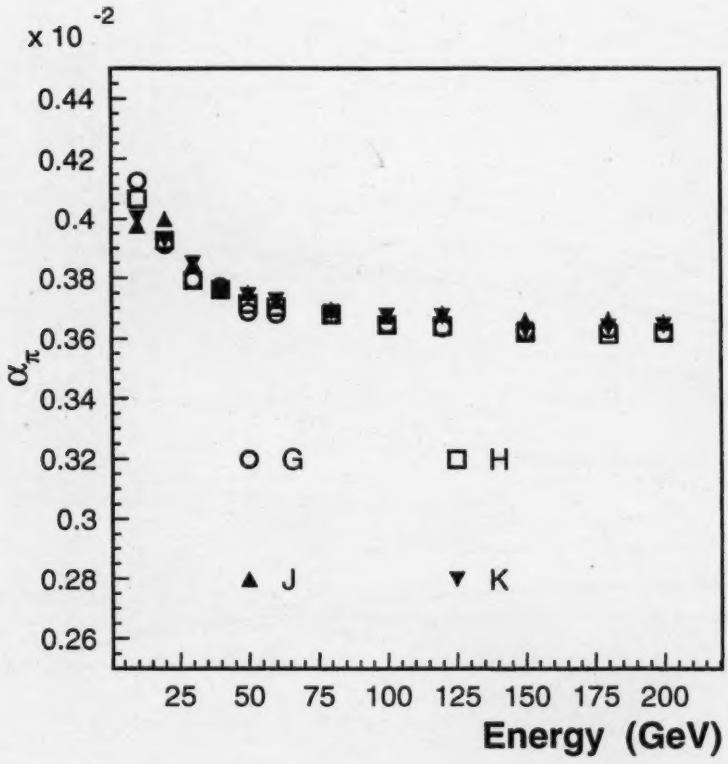

Figure 8.13: The pion conversion factor as determined in reference [1]. This is for four of the points along the horizontal $y = 0$ line of the HEC detector.

Figure Number	Corrected or Uncorrected	Number of Points	Parametrization $f(x) =$
8.14	Uncorrected	6	$0.11 \ln\left(\frac{E}{E_0'}\right)$
8.15	Corrected	6	$0.11 \ln\left(\frac{E}{E_0'}\right)$
8.16	Uncorrected	3	$0.11 \ln\left(\frac{E}{E_0'}\right)$
8.17	Corrected	3	$0.11 \ln\left(\frac{E}{E_0'}\right)$
8.18	Uncorrected	6	$1 - \left(\frac{E}{E_0'}\right)^{-0.15}$
8.19	Corrected	6	$1 - \left(\frac{E}{E_0'}\right)^{-0.15}$
8.20	Uncorrected	3	$1 - \left(\frac{E}{E_0'}\right)^{-0.15}$
8.21	Corrected	3	$1 - \left(\frac{E}{E_0'}\right)^{-0.15}$

Table 8.4: A table summarizing the features of the plots in figures 8.14 on the next page through 8.21 on page 104.

on lateral leakage. The leakage corrections obtained from reference [1] used in this thesis, strictly speaking, only apply to impact points on the horizontal $y = 0$ line. To facilitate comparisons, a second fit was performed, but this time it was restricted to the three impact points common to both this analysis, and to the one in reference [1], which can be seen in figure 8.17 on page 100. A value of $\frac{e}{h} = 1.592 \pm 0.022$ was found for this fit. Using the alternative parameterization from equation 8.4 on page 91, we find $\frac{e}{h} = 1.673 \pm 0.023$ for the six point fit, and $\frac{e}{h} = 1.613 \pm 0.016$ for the three point fit. (See figures 8.19 on page 102 and 8.21 on page 104 respectively.) Both of these values are larger than the value of $\frac{e}{h} = 1.49 \pm 0.01 \pm 0.10$ found in reference [1] as seen in figure 8.22 on page 105, originally published as figure 35 in reference [1]. The systematic uncertainty on this figure is a factor of 10 times greater than the statistical uncertainty, which again supports the idea that the purely statistical uncertainties used in this analysis underestimate the actual uncertainties. Comparing these results with those from reference [1], accounting for the systematic errors in the results from reference [1], gives rise to virtually no discrepancy, differing by about one standard deviation.

It is believed that the differences between these results and those in reference [1] are a result of a systematic error in this analysis. Any such systematic error would be of a larger magnitude in the analysis of the conversion factor than in the energy resolution, as the energy resolution is a ratio of two measured quantities, while the

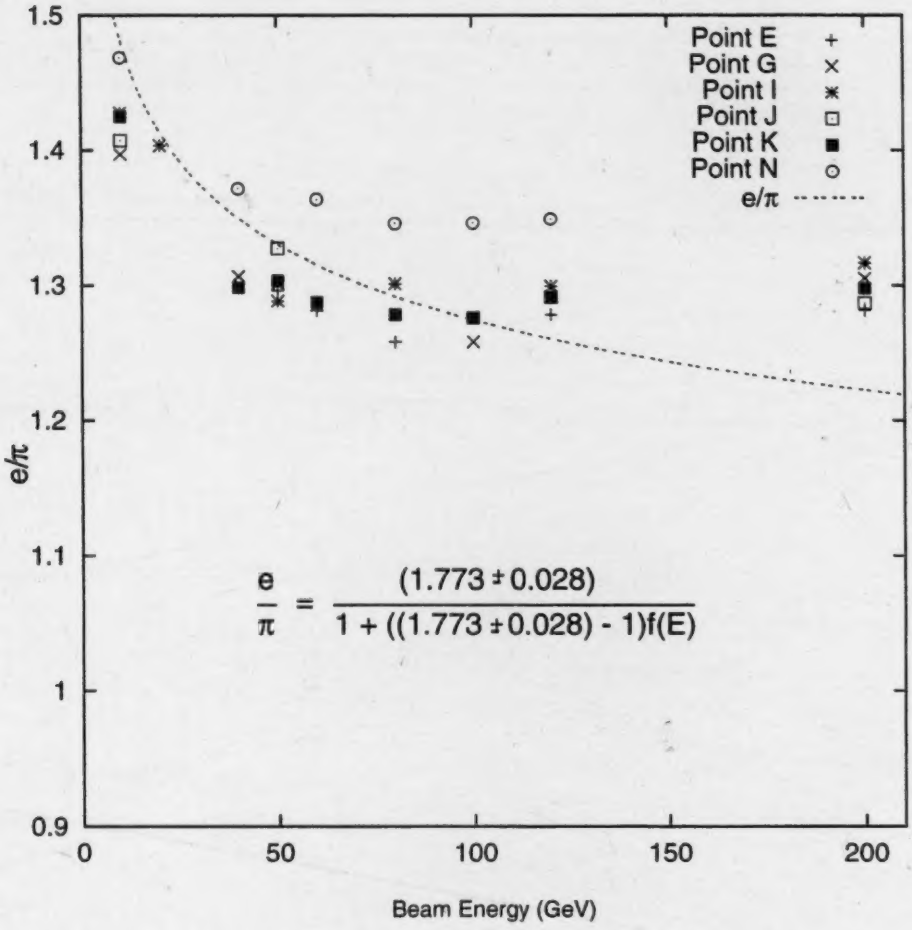

Figure 8.14: The parameterization of the function in equation 8.2 on page 91 with $f(E) = 0.11 \ln\left(\frac{E}{E_0'}\right)$. These data have not been corrected for leakage. The data set here contains all data points examined in this analysis.

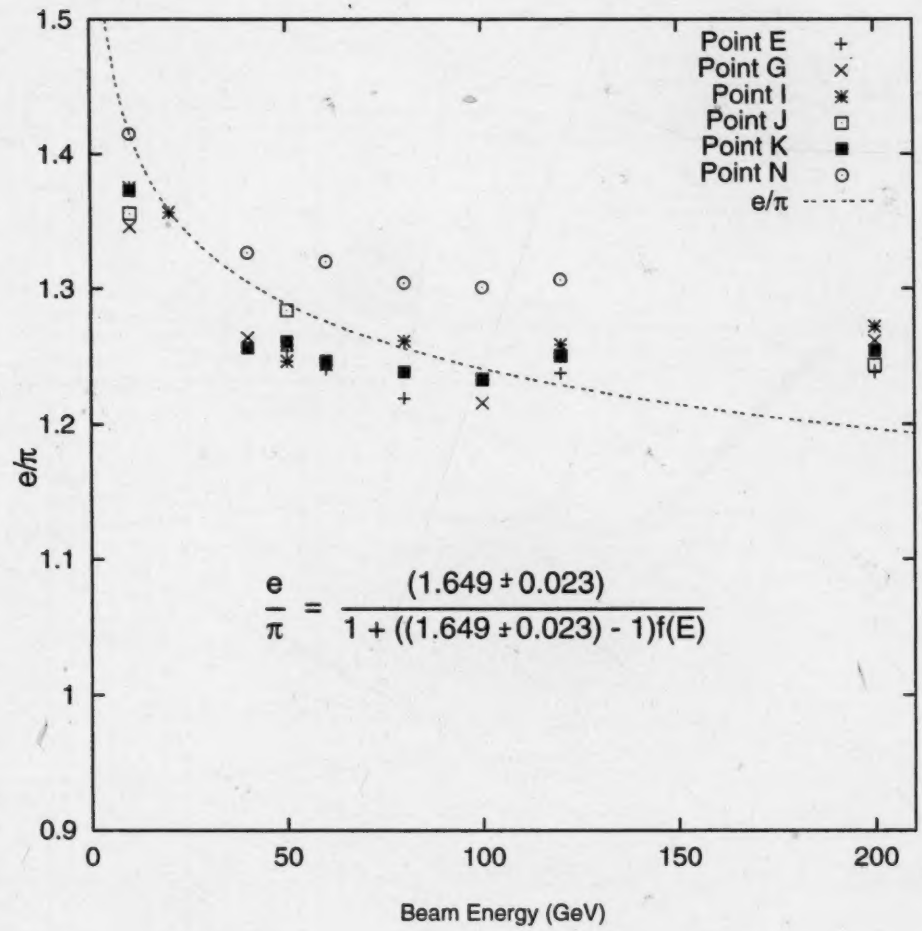

Figure 8.15: The parameterization of the function in equation 8.2 on page 91 with $f(E) = 0.11 \ln\left(\frac{E}{E_0}\right)$. These data have been corrected for leakage. The data set here contains all data points examined in this analysis.

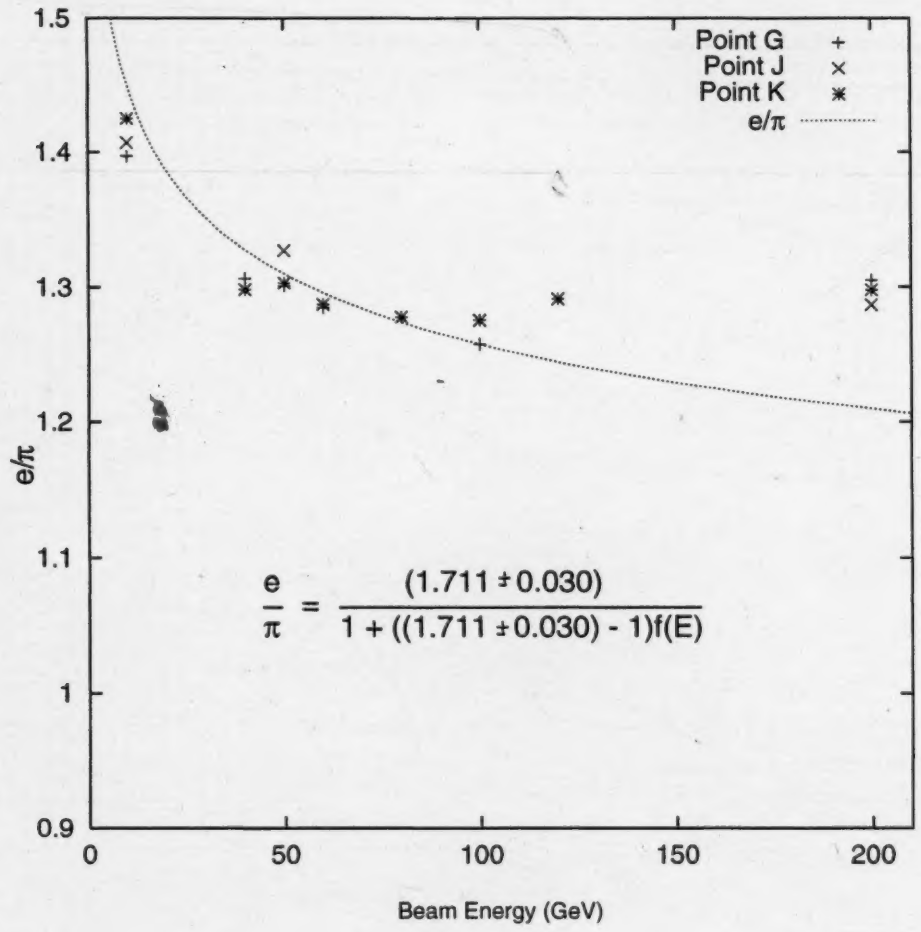

Figure 8.16: The parameterization of the function in equation 8.2 on page 91 with $f(E) = 0.11 \ln\left(\frac{E}{E_0}\right)$. These data have not been corrected for leakage. The data set here is restricted to the data points along the horizontal line examined in reference [1].

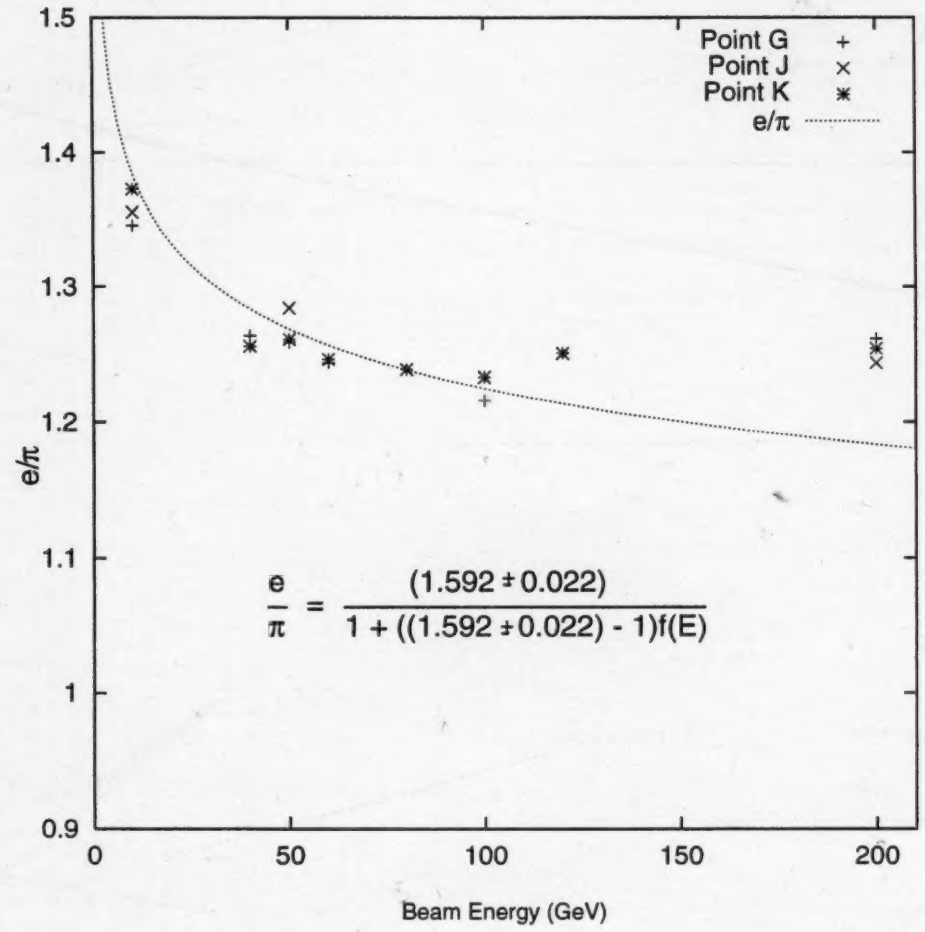

Figure 8.17: The parameterization of the function in equation 8.2 on page 91 with $f(E) = 0.11 \ln\left(\frac{E}{E_0}\right)$. These data have been corrected for leakage. The data set here is restricted to the data points along the horizontal line examined in reference [1].

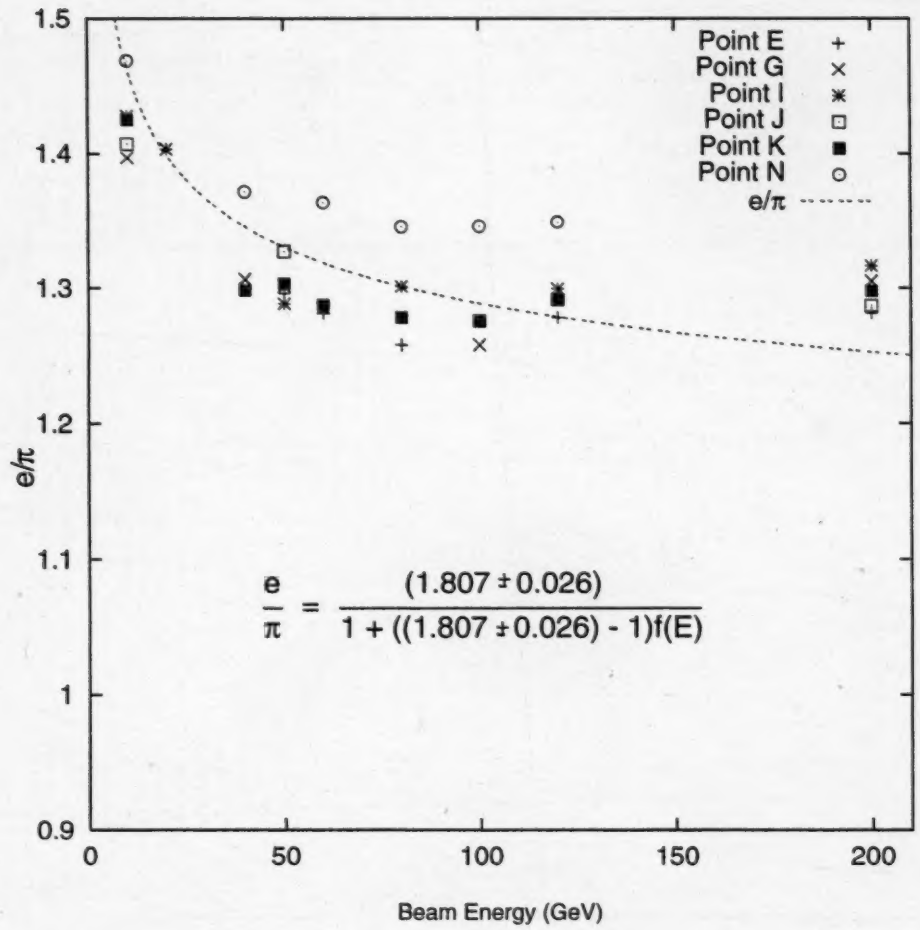

Figure 8.18: The parameterization of the function in equation 8.2 on page 91 with $f(E) = 1 - \left(\frac{E}{E_0'}\right)^{-0.15}$. These data have not been corrected for leakage. The data set here contains all data points examined in this analysis.

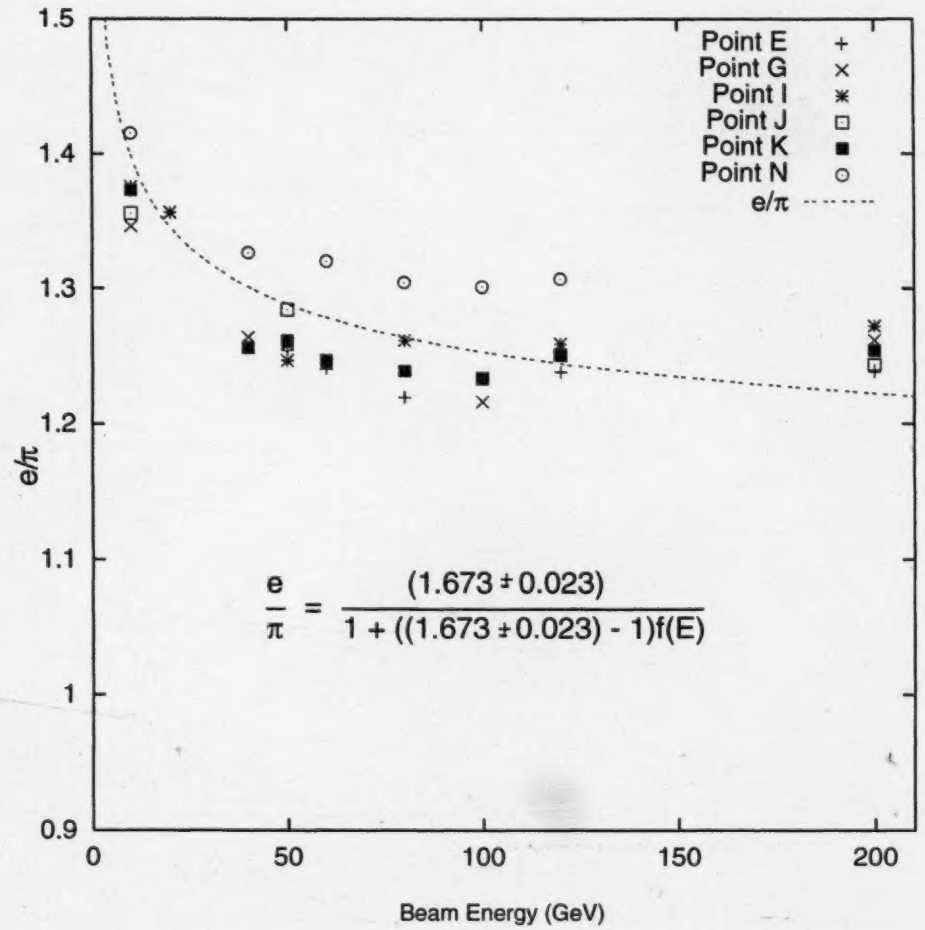

Figure 8.19: The parameterization of the function in equation 8.2 on page 91 with $f(E) = 1 - \left(\frac{E}{E_0}\right)^{-0.15}$. These data have been corrected for leakage. The data set here contains all data points examined in this analysis.

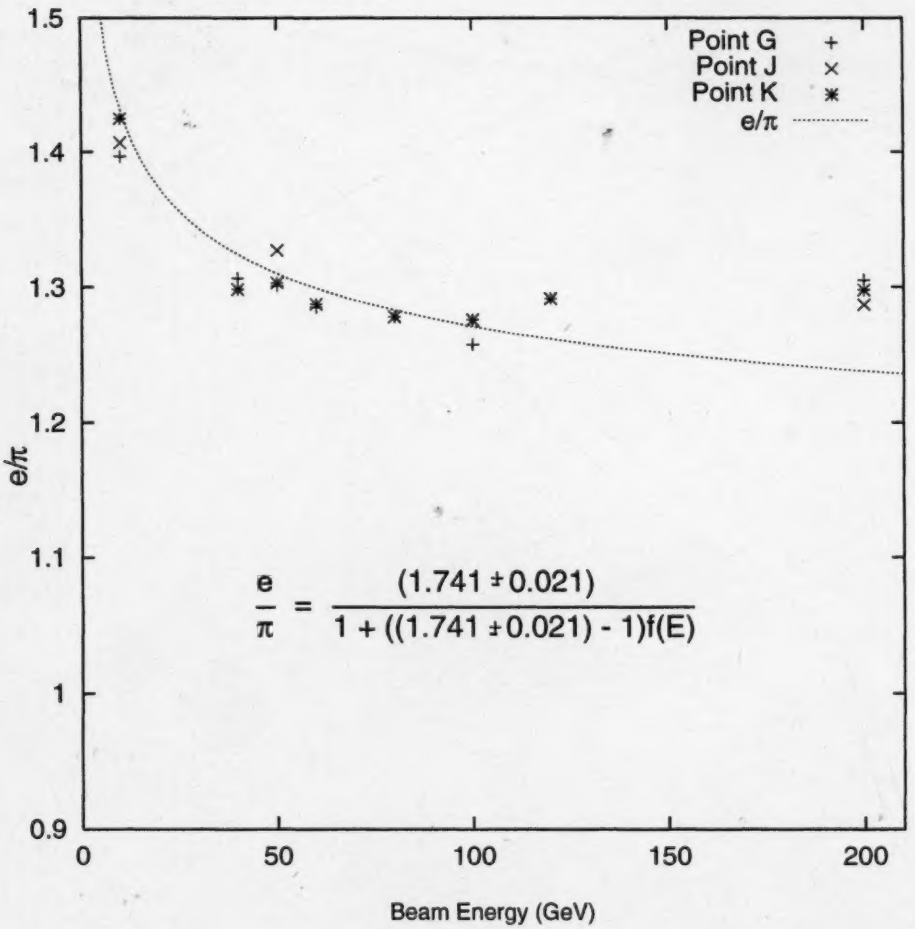

Figure 8.20: The parameterization of the function in equation 8.2 on page 91 with $f(E) = 1 - \left(\frac{E}{E_0'}\right)^{-0.15}$. These data have not been corrected for leakage. The data set here is restricted to the data points along the horizontal line examined in reference [1].

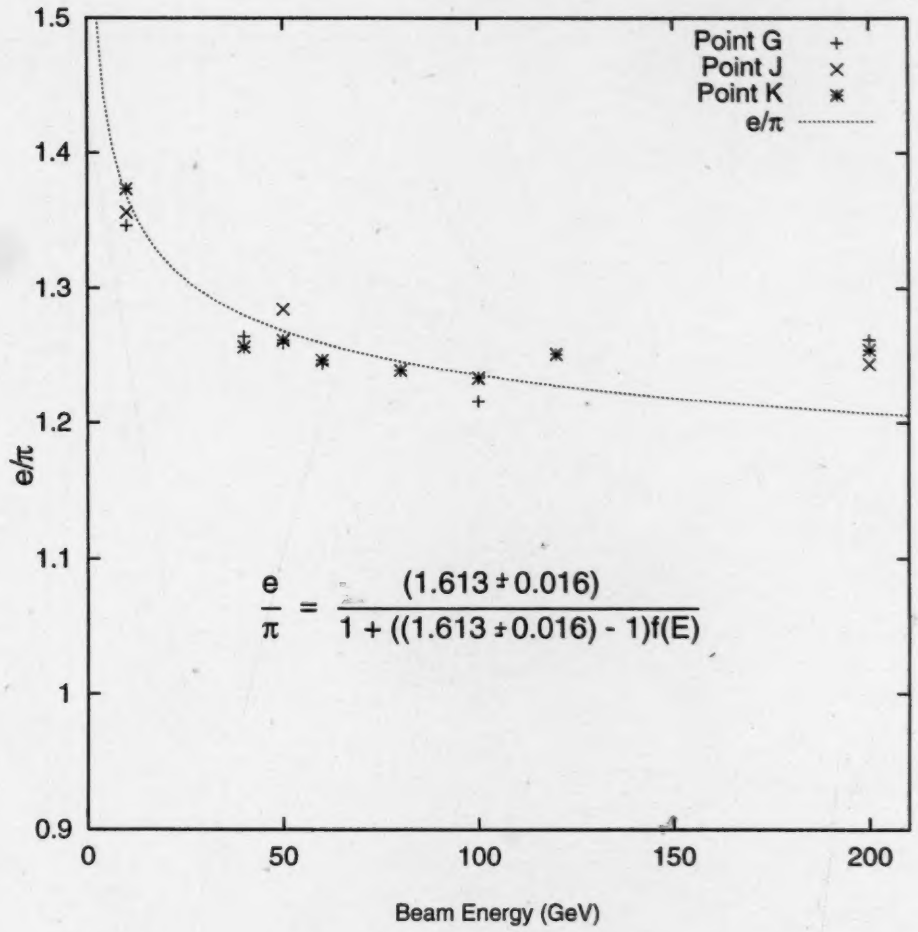

Figure 8.21: The parameterization of the function in equation 8.2 on page 91 with $f(E) = 1 - \left(\frac{E}{E_0}\right)^{-0.15}$. These data have been corrected for leakage. The data set here is restricted to the data points along the horizontal line examined in reference [1].

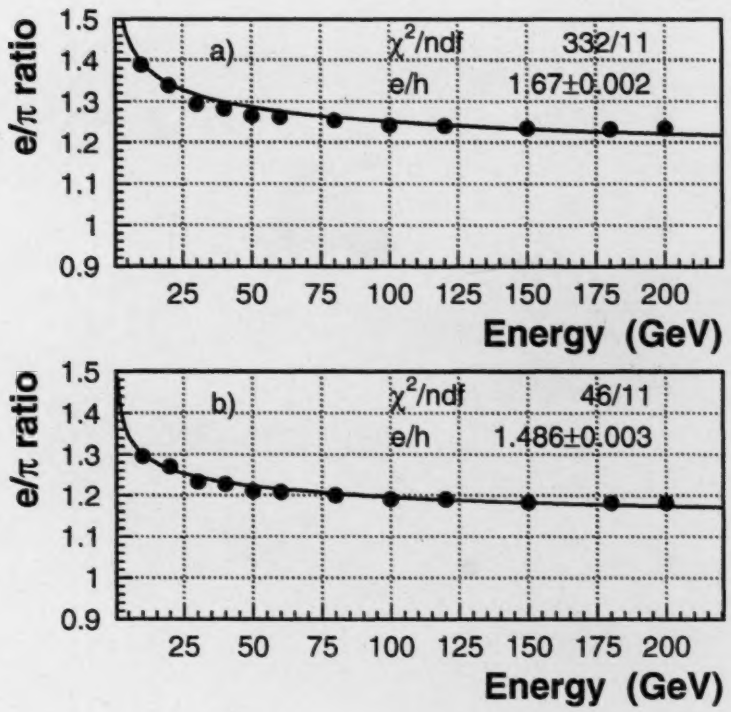

Figure 8.22: The $\frac{e}{\pi}$ parameterization of the function in equation 8.2 on page 91. The top plot is uncorrected for leakage, while the lower plot is corrected. Both plots are taken directly from reference [1].

conversion factor is linearly dependant on measured quantities. The error which would give rise to such a discrepancy would be in the calibration constants used in the digital filtering procedure. However, comparing the corrected and uncorrected data for any given set of conditions demonstrates a qualitative agreement with the results of reference [1]. In both cases, there is a significant decrease in the value of the conversion factors after the correction for leakage.

Chapter 9

Conclusion

The electron and pion beam data from the August 2000 HEC testbeam have been analyzed, and show that (this typical portion of) the hadronic endcap calorimeter will be able to perform as expected when ATLAS is completed in the next few years.

The overall intrinsic energy resolution for electrons was found to be

$$\frac{\sigma}{E'} = \frac{\left(21.27 \pm 0.08\,\%\sqrt{\mathrm{GeV}}\right)}{\sqrt{E_0}} \oplus (0.92 \pm 0.03\,\%) \tag{9.1}$$

for all six impact points being examined, with an electromagnetic conversion factor of $\alpha_{em} = 3.06\,\mathrm{GeV}/\mu\mathrm{A}$. The equivalent intrinsic energy resolution for the three points along the $y = 0$ line is

$$\frac{\sigma}{E'} = \frac{\left(21.0 \pm 0.1\,\%\sqrt{\mathrm{GeV}}\right)}{\sqrt{E_0}} \oplus (0.90 \pm 0.04\,\%) \tag{9.2}$$

with a corresponding electromagnetic conversion factor of $\alpha_{em} = 3.05\,\mathrm{GeV}/\mu\mathrm{A}$. Uncertainties were omitted from the conversion factor results, as the most significant effects will be due to systematic factors that were not taken into account in this analysis. All electron results are quoted for clusters composed of the five cells with the highest energy deposited. The previous testbeam results for electrons (see [1]) found that

$$\frac{\sigma}{E'} = \frac{\left(21.4 \pm 0.2\,\%\sqrt{\mathrm{GeV}}\right)}{\sqrt{E_0}} \oplus (0.3 \pm 0.2\,\%) \tag{9.3}$$

which is in agreement with these results within two standard deviations. The theoretical prediction from the Monte Carlo simulation (see [1]) is

$$\frac{\sigma}{E'} = \frac{\left(21.7 \pm 0.1\,\%\sqrt{\mathrm{GeV}}\right)}{\sqrt{E_0}} \oplus (0.0 \pm 0.2\,\%) \tag{9.4}$$

The overall intrinsic energy resolution for pions was found to be

$$\frac{\sigma}{E'} = \frac{\left(88.0 \pm 1.2\,\%\sqrt{\text{GeV}}\right)}{\sqrt{E_0}} \oplus (5.88 \pm 0.16\,\%) \tag{9.5}$$

for all six impact points being examined, with $\frac{e}{h} = 1.649 \pm 0.023$ and $\frac{e}{h} = 1.673 \pm 0.023$ for the parameterizations with $f(E) = 0.11 \ln\left(\frac{E}{E_0'}\right)$ and $f(E) = 1 - \left(\frac{E}{E_0'}\right)^{-0.15}$ respectively. The equivalent intrinsic energy resolution for the three points along the $y = 0$ line is

$$\frac{\sigma}{E'} = \frac{\left(81.8 \pm 1.4\,\%\sqrt{\text{GeV}}\right)}{\sqrt{E_0}} \oplus (6.11 \pm 0.18\,\%) \tag{9.6}$$

with $\frac{e}{h} = 1.592 \pm 0.022$ and $\frac{e}{h} = 1.613 \pm 0.016$ for the parameterizations with $f(E) = 0.11 \ln\left(\frac{E}{E_0'}\right)$ and $f(E) = 1 - \left(\frac{E}{E_0'}\right)^{-0.15}$ respectively. All pion results are quoted for clusters composed of the fifty-five cells with the highest energy deposited. It should be noted that the uncertainties in the above expressions are purely statistical. There is good reason to believe that the results are sensitive to systematic effects not accounted for here, as the results from point to point are inconsistent, often with high values of the χ^2 measure of confidence in a fit.

It is perhaps more sensible to discuss the non-intrinsic energy resolution when discussing these results, as the assumption that C is a constant for all runs at a given impact point may not be valid. In this case, the energy resolution for all six impact points would be given by

$$\frac{\sigma}{E'} = \frac{\left(86.5 \pm 2.5\,\%\sqrt{\text{GeV}}\right)}{\sqrt{E_0}} \oplus (6.05 \pm 0.23\,\%) \oplus \frac{(6.32 \pm 0.05\,\text{GeV})}{E_0} \tag{9.7}$$

while the result for the three $y = 0$ points is

$$\frac{\sigma}{E'} = \frac{\left(81.0 \pm 3.0\,\%\sqrt{\text{GeV}}\right)}{\sqrt{E_0}} \oplus (6.30 \pm 0.26\,\%) \oplus \frac{(6.33 \pm 0.06\,\text{GeV})}{E_0} \tag{9.8}$$

The previous testbeam results for pions (see [1]) found that

$$\frac{\sigma}{E'} = \frac{\left(70.5 \pm 1.5\,\%\sqrt{\text{GeV}}\right)}{\sqrt{E_0}} \oplus (5.7 \pm 0.2\,\%) \tag{9.9}$$

which is not in agreement with the results of this analysis within two standard deviations, but it does agree within three standard deviations. It is in closer agreement to the non-intrinsic resolution than the intrinsic resolution, however. The theoretical prediction from the Monte Carlo simulation (see [1]) is

$$\frac{\sigma}{E'} = \frac{\left(65.6 \pm 0.7\,\%\sqrt{\text{GeV}}\right)}{\sqrt{E_0}} \oplus (4.9 \pm 0.1\,\%) \tag{9.10}$$

The pion results are not consistent with past testbeams or with the design specifications of the HEC. However, it is believed that those inconsistencies are a result of systematic effects which have not been taken into account. If we assume that all of these inconsistencies are a result of a single cause, then that cause would have to be a problem with the calibration constants used in the digital filtering procedure. If this is, indeed, the cause of these difficulties, then the correction of the problems for the ATLAS experiment will be a relatively simple task.

The fraction $\frac{e}{h}$ was found to be $\frac{e}{h} = 1.592 \pm 0.022$ with the parameterization $f(E) = 0.11 \ln\left(\frac{E}{E_0'}\right)$ and $\frac{e}{h} = 1.613 \pm 0.016$ with the parameterization $f(E) = 1 - \left(\frac{E}{E_0'}\right)^{-0.15}$. Both results are approximately 8% higher than the results published in reference [1] ($\frac{e}{h} = 1.486 \pm 0.003$).

This analysis, which was performed with several new programs in a new software package that is independent of past analyses, examines the performance measuring hadronic and electromagnetic showers of the six HEC modules used at the August 2000 testbeam. Future analyses should take note of systematic errors, particularly those resulting from calibration errors and time dependence of the noise subtraction of data. The author is confident that this portion of ATLAS will be able to perform up to design specifications when ATLAS is complete, without compromising the physics goals of the experiment.

Appendix A

Miscellaneous Derivations

This chapter is home to the calculations and derivations that were computed specifically for this thesis, and not quoted from an external reference.

A.1 Deriving Equation 2.4 on page 10

We begin by making the simplifying substitutions $\sigma_0 = \alpha Z^2 r_e^2$ and $\mu = \frac{E_+}{k}$ into equation 2.3 on page 8, leaving us with

$$\frac{d\sigma}{d\mu} = 4\sigma_0 \left[\left(\frac{4}{3}\mu^2 - \frac{4}{3}\mu + 1 \right) \ln\left(\frac{183}{Z^{\frac{1}{3}}} \right) - \frac{1}{9}\mu(1-\mu) \right] \tag{A.1}$$

Integrating this over all μ, we have

$$\begin{aligned}
\sigma &= 4\sigma_0 \int_0^1 \left[\left(\frac{4}{3}\mu^2 - \frac{4}{3}\mu + 1 \right) \ln\left(\frac{183}{Z_2^{\frac{1}{3}}} \right) - \frac{\mu}{9} + \frac{\mu^2}{9} \right] d\mu \\
\sigma &= 4\sigma_0 \left[\left(\frac{4}{9}\mu^3 - \frac{2}{3}\mu^2 + \mu \right) \ln\left(\frac{183}{Z_2^{\frac{1}{3}}} \right) - \frac{\mu^2}{18} + \frac{\mu^3}{27} \right]_0^1 \\
\sigma &= 4\sigma_0 \left[\left(\frac{4}{9} - \frac{2}{3} + 1 \right) \ln\left(\frac{183}{Z_2^{\frac{1}{3}}} \right) - \frac{1}{18} + \frac{1}{27} \right]
\end{aligned}$$

which leaves us with equation 2.4 on page 10:

$$\sigma = 4\alpha Z_2^2 r_e^2 \left(\frac{7}{9} \ln\left(\frac{183}{Z_2^{\frac{1}{3}}} \right) - \frac{1}{54} \right) \tag{A.2}$$

Appendix B

My Contributions

My experiences in the M.Sc. program included some valuable education and experiences that do not appear in this analysis in a tangible form. This appendix will detail all of the specifics involved in this particular degree program, sorted chronologically.

B.1 The Summer of '99

The summer after the completion of my B.Sc. was spent working with the 1998 test beam data and the `hec_adc` software package, so that I might be more familiar with the tools that I'd be working with as well as the sorts of results to expect. It was during this time that I became familiar with all of the existing CERN software tools. I also participated in a quality control check for the marriage frames made to assemble the modules for use in the testbeam during this period.

B.2 The Course Work

From September 1999 to April 2000, I worked on the course credits required for my thesis. Three of the courses (non-relativistic quantum mechanics, relativistic quantum mechanics, and particle physics) were fairly standard courses for this type of program. The fourth course, designed by Dr. Nate Rodning, was rather unique. In it, six students took part in the design, implementation and analysis of an experiment. We started by deciding what we would measure (a muon scattering cross section) and how we would do so. We then calculated the theoretical predictions, and designed the apparatus. Once we were ready to collect the data, we went to TRIUMF for several days, and performed the actual experiment. Once we obtained the data, we returned to the University of Alberta for the analysis. The experience garnered from this course was invaluable. It was also my first exposure to the LaTeX

document formatting system, which we used to prepare our homework assignments, as well as this thesis.

B.3 The Summer of 2000

Following the course work required for my thesis, I spent six months at CERN. There were several benefits of this time, including:

Data Collection I worked shifts in the beam hut during the collection of the data used in this thesis and in reference [1].

Colleague Interaction I met several collaborators involved in the HEC project specifically and ATLAS in general. These formal and informal discussions provided valuable advice and feedback that was implemented in this analysis.

Programming Experience Most of the software written specifically for this analysis was written during this period. The environment was well suited to this, as I was able to discuss programming strategies with several individuals who had previously written equivalent software for this project.

Presentation Experience I was able to present preliminary results from both the June and August 2000 testbeams at "LArg weeks" during this period. A "LArg week" is a collaboration meeting that is roughly five days long, designed to allow members of the liquid argon collaboration to present the most recent information available in all aspects of the experiment.

B.4 The Remaining Time

The time spent working on this thesis since my return from CERN has been spent primarily on the tangible results you see before you. It was during this period that the analysis was completed, and this thesis was written.

References

[1] Dowler et al. Performance of the ATLAS hadronic end-cap calorimeter in beam tests. Technical report, ATLAS, May 2001.

[2] Richard Fernow. *Introduction to experimental particle physics.* Cambridge University Press, 1986.

[3] K. Hagiwara et al. Review of Particle Physics. *Physical Review D*, 66:010001+, 2002.

[4] ATLAS collaboration. ATLAS Detector and Physics Performance Technical Design Report. Technical report, ATLAS, May 1999.

[5] R. K. Ellis at al. *QCD and Collider Physics.* Cambridge University Press, 1996.

[6] M. Kobayashi and K. Maskawa. *Progr. Theor. Phys.* 49, 282, 1972.

[7] P. W. Higgs. *Phys. Lett.* 12, 132, 1964.

[8] P. W. Higgs. *Phys. Rev.* 145, 1156, 1966.

[9] C. Quigg. *Gauge Theories of the Strong, Weak, and Electromagnetic Interactions.* Addison Wesley, 1997.

[10] G. G. Ross. Beyond the standard model. In *16th LLWI.* World Scientific, 2002.

[11] CERN. The Large Hadron Collider Home Page. World Wide Web Site. http://lhc-new-homepage.web.cern.ch/lhc-new-homepage/.

[12] ATLAS LARG Unit. Liquid Argon Calorimeter Technical Design Report. Technical report, ATLAS, December 1996.

[13] ATLAS Muon Collaboration. ATLAS Muon Spectrometer Technical Design Report. Technical report, June 1997. CERN / LHCC 97-22.

[14] Konrad Elsener. Short Introduction to the use of the H6 Beam. Technical report, CERN, April 1998.

[15] MPI Group. Proposal for the Standard HEC Test Beam Programme. Technical report, MPI Group, January 04, 2001.

[16] M. Lefebvre and D. O'Neil. Endcap Hadronic Calorimeter Testbeam Software Framework, A Proposal: The hec adc package. Technical Report HEC Note 35, ATLAS, University of Victoria, Victoria, Canada, May 1997.

[17] M. Lefebvre and D. O'Neil. Endcap Hadronic Calorimeter Offline Testbeam Software, The hec adc Package Version 3.6. Technical Report HEC Note 69, ATLAS, University of Victoria, Victoria, British Columbia, Canada, March 1999.

[18] R. Wigmans. Nucl. Instr. and Meth. A239, 273, 1988.

[19] D. Groom. What really goes on in a hadronic calorimeter. In *VII International Conference on Calorimetry in High Energy Physics*, Tuscon, Arizona, November 1997.